

# $W$ production in $ep$ collisions

Nicholas Malden

November 2000



THE UNIVERSITY  
*of* MANCHESTER

High Energy Group  
Department of Physics and Astronomy

A thesis submitted to The University of Manchester for the degree of  
Doctor of Philosophy in the Faculty of Science and Engineering

# Contents

<b>1</b>	<b>Introduction</b>	<b>10</b>
<b>2</b>	<b>The H1 experiment</b>	<b>12</b>
2.1	HERA . . . . .	12
2.2	An Overview of the H1 Detector . . . . .	13
2.3	Tracking . . . . .	15
2.3.1	Central Jet Chambers . . . . .	17
2.3.2	Central $z$ Chambers . . . . .	18
2.3.3	Forward Tracking Detector . . . . .	18
2.3.4	Backward Drift Chamber . . . . .	19
2.3.5	Multiwire Proportional Chambers . . . . .	19
2.4	Calorimetry . . . . .	20
2.4.1	The Liquid Argon Calorimeter . . . . .	21
2.4.2	The SpaCal . . . . .	23
2.4.3	The Tail Catcher . . . . .	24
2.4.4	The Plug Calorimeter . . . . .	24

<i>CONTENTS</i>	3
2.5 The Muon Systems . . . . .	25
2.5.1 The Instrumented Iron . . . . .	25
2.5.2 The Forward Muon Detector . . . . .	25
2.6 Time-of-Flight Detectors . . . . .	27
2.7 The Luminosity System . . . . .	28
2.8 Triggering and Data Acquisition . . . . .	29
2.9 Trigger Efficiencies . . . . .	31
2.9.1 The “Pseudo-CC” Sample . . . . .	32
2.9.2 Determining the Trigger Efficiencies . . . . .	32
<b>3 Theory</b>	<b>35</b>
3.1 Electron Proton Scattering . . . . .	35
3.2 Kinematics . . . . .	36
3.3 Deep Inelastic Scattering . . . . .	38
3.4 Hadronisation and Jets . . . . .	43
3.5 Photoproduction . . . . .	44
3.6 W production . . . . .	45
3.7 Beyond the Standard Model . . . . .	48
<b>4 Monte Carlo Simulation</b>	<b>52</b>
4.1 The Stages of Event Simulation . . . . .	53
4.2 EPVEC . . . . .	54

<i>CONTENTS</i>	4
4.2.1 Cross Section Calculation . . . . .	54
4.2.2 Event Characteristics . . . . .	57
4.3 Background Processes . . . . .	57
<b>5 Event Selection : Part I</b>	<b>60</b>
5.1 The “Isolated Lepton” Analysis . . . . .	60
5.2 The Presented Data . . . . .	63
5.3 The Selection Variables . . . . .	63
5.4 Lepton Identification . . . . .	66
5.4.1 Electron Candidates . . . . .	66
5.4.2 Muon Candidates . . . . .	66
5.5 Hadronic Reconstruction . . . . .	69
5.6 Rejection of non- $ep$ Processes . . . . .	71
5.7 The Cuts . . . . .	71
5.7.1 Selecting the Electron Channel : $ep \rightarrow eWX \rightarrow ee\nu X$ . . . . .	74
5.7.2 Selecting the Muon Channel : $ep \rightarrow eWX \rightarrow e\mu\nu X$ . . . . .	85
<b>6 Background Studies</b>	<b>92</b>
6.1 Analysis of the Distributions in the Electron Channel . . . . .	92
6.1.1 $\zeta^2$ . . . . .	93
6.1.2 $P_T^{calo}$ . . . . .	94
6.1.3 $\frac{V_{ap}}{V_p}$ . . . . .	97

6.1.4	$\delta_{miss}$	99
6.1.5	$\Delta\phi_{e-X}$	100
6.1.6	$D_{track}$	101
6.1.7	$P_T^X$	102
6.2	Analysis of the Distributions in the Muon Channel	104
6.2.1	$P_T^\mu$	105
6.2.2	$\frac{V_{ap}}{V_p}$	106
6.2.3	$\Delta\phi_{\mu-X}$	108
6.2.4	$D_{track}$	109
6.2.5	$P_T^X$	110
6.3	A NC Study Sample	111
6.4	A CC Study Sample	113
6.5	A $\mu^+\mu^-$ Study Sample	115
<b>7</b>	<b>Event Selection : Part II</b>	<b>117</b>
7.1	The Final Selection of the Electron Channel	117
7.1.1	The Cuts	117
7.1.2	Distributions of the Final Electron Selection	118
7.2	The Final Selection of the Muon Channel	122
7.2.1	The Cuts	122
7.2.2	Distributions of the Final Muon Selection	123
7.3	Selection Efficiencies	126

<b>8</b>	<b>Final Results and Discussion</b>	<b>128</b>
8.1	Results in the Positron-Proton Data . . . . .	128
8.1.1	Tables . . . . .	128
8.1.2	Event Kinematics . . . . .	132
8.2	Results in the Electron-Proton Data . . . . .	136
8.2.1	Tables . . . . .	136
8.3	Discussion . . . . .	138
<b>9</b>	<b>Summary</b>	<b>143</b>
	<b>Bibliography</b>	<b>144</b>
<b>A</b>	<b>Event Displays</b>	<b>155</b>
<b>B</b>	<b>Comparison with ZEUS</b>	<b>163</b>
<b>C</b>	<b>A Note about Collaboration</b>	<b>165</b>

## Abstract

A search for  $W$  boson production in the process  $ep \rightarrow eWX$ , with subsequent  $W$  decay into electrons or muons, has been performed at the electron-proton collider HERA using an integrated luminosity of  $13.6 \text{ pb}^{-1}$  in  $e^-p$  scattering and  $81.6 \text{ pb}^{-1}$  in  $e^+p$  scattering. The analysis has been tuned to maximise the acceptance of  $W$  boson production, and reject other Standard Model processes. In  $e^-p$  interactions no events are observed, consistent with the expectation of the Standard Model in this low luminosity sample. In the  $e^+p$  data 14 events are seen compared to an expectation of  $8.2 \pm 2.0$  dominated by  $W$  production ( $6.4 \pm 1.9$ ). The excess above the expectation is mainly due to events with transverse momentum of the hadronic system greater than 25 GeV where 9 events are found compared to  $2.3 \pm 0.6$  expected.

## Zusammenfassung

Eine Suche nach Produktion von  $W$  Bosonen im Prozeß  $ep \rightarrow eWX$  mit anschließendem Zerfall des  $W$  Bosons in ein Elektron oder Myon und ein Neutrino wurde durchgeführt. Sie basiert auf der Analyse von Daten des H1 Experimentes am HERA Elektron-Proton Beschleuniger, die einer integrierten Luminosität von  $13.6 \text{ pb}^{-1}$  in  $e^-p$  Streuung und von  $81.6 \text{ pb}^{-1}$  in  $e^+p$  Streuung entsprechen. Die Analyse ist optimiert worden, die Effizienz für Ereignisse mit  $W$  Boson Produktion zu maximieren und Untergrund durch andere Prozesse des Standardmodells zu unterdrücken. In den  $e^-p$  Daten werden keine Ereignisse beobachtet, übereinstimmend mit der Erwartung des Standardmodells in diesem kleinen Datensatz. In den  $e^+p$  Daten werden 14 Ereignisse beobachtet, die mit einer Erwartung von  $8.2 \pm 2.0$  zu vergleichen sind, die durch  $W$  Produktion beherrscht ist ( $6.4 \pm 1.9$ ). Der Überschuß an Ereignissen über der Erwartung des Standardmodells ist am deutlichsten für Transversalimpulse des hadronischen Systems grösser als 25 GeV. In diesem kinematischen Bereich wurden 9 Ereignisse beobachtet, während nur  $2.3 \pm 0.6$  vorhergesagt werden.

No portion of the work referred to in this thesis has been submitted in support of an application for another degree or qualification of this or any other university or other institute of learning.

Copyright in text of this thesis rests with the author. Copies (by any process) either in full, or of extracts, may be made only in accordance with instructions given by the Author and lodged in the John Rylands University Library of Manchester. Details may be obtained from the librarian. This page must form part of any such copies made. Further copies (by any process) of copies made in accordance with such instructions may not be made without the permission (in writing) of the author.

The ownership of any intellectual property rights which may be described in this thesis is vested in the University of Manchester, subject to any prior agreement to the contrary, and may not be made available for use by third parties without the written permission of the University, which will prescribe the terms and conditions of any such agreement.

Further information on the conditions under which disclosures and exploitation may take place is available from the Head of the Department of Physics and Astronomy.

This work was supported financially by the Particle Physics and Astronomy Research Council (PPARC) between October 1997 and September 2000.



*For my parents*

# Chapter 1

## Introduction

The high energy scattering of a lepton off the proton has provided much information about the proton's sub-structure. The subject of Deep Inelastic Scattering (DIS) was born at the fixed target experiments, and more recently has been taken further by collider experiments. HERA is the only electron-proton collider in the world, and provides access to a unique region of exploration in high energy physics. HERA has allowed the detailed study of the proton's constituents, in particular when they carry only tiny fractions of the proton's total momentum.

Yet HERA's exploration potential is not only limited to these "low- $x$ " (low momentum fraction) regimes. At the other end of the spectrum, HERA provides the opportunity to observe the production of very massive particles, formed when the electron interacts with a constituent of the proton carrying a large proportion of the proton's total momentum.

One such process is  $W$  production. Having a mass of around  $80 \text{ GeV}^1$ , a large proportion of the HERA centre-of-mass energy ( $\sim 320 \text{ GeV}$ ) is required for the formation of a real  $W$ . Consequently  $W$  production in  $ep$  collisions is a rare process – in the entire operational history of HERA, a period of some 8 years, barely two

---

<sup>1</sup>Natural units are used throughout this thesis, i.e.  $\hbar = c = 1$ .

dozen such events have been observed by the two  $ep$  collision experiments combined.

Nevertheless, the study of this process is of great importance for not only does it allow a weakly tested region of the Standard Model to be examined, it also provides a window to potential physics *beyond the Standard Model* (BSM). This is because even heavier particles may decay via a real  $W$ , enhancing the rate predicted by the Standard Model. Also, the decay signature of a  $W$ , by which its production is identified, is the same as that of several particles postulated to exist by BSM theories.

# Chapter 2

## The H1 experiment

### 2.1 HERA

HERA (Hadron-Elektron-Ring-Anlage) lies in the west of Hamburg, and consists of two nearly concentric evacuated beam pipes 6.3km in circumference. In one beam pipe protons are accelerated to 920 GeV<sup>1</sup> and in the other positrons<sup>2</sup> are accelerated to 27.6 GeV. The beam pipes intersect at two points on the ring, around which the two  $ep$  collision experiments, H1 and ZEUS, are constructed.

Both proton and positron beams are accelerated by superconducting cavities in pulses or “bunches”. Bunches from each beam are steered into collision every 96 ns, however not all bunches are collided. Non-colliding bunches are known as pilot bunches, and allow the experiments to measure the rate of interactions between the beams and residual gas in the beam pipes, and between the beams and the beam pipe wall.

---

<sup>1</sup>from 1994 to 1997, the proton beam energy was 820 GeV.

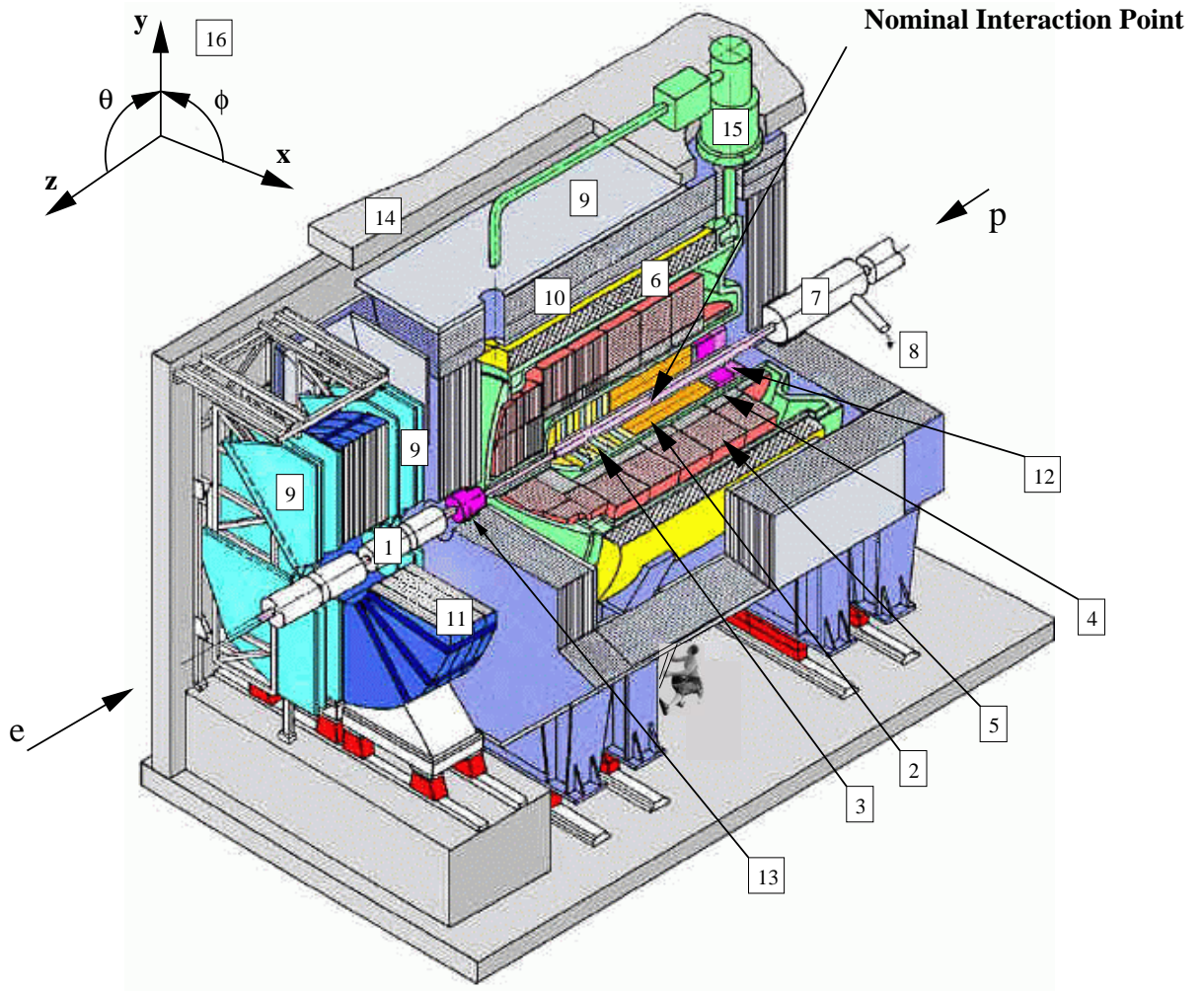
<sup>2</sup>between 1994 and 2000 HERA has mainly accelerated positrons. For 1998 and the first half of 1999, electrons were used. For the rest of this thesis, the term *electron* will be employed, referring generically to both electrons and positrons. Distinction will be made explicit where required.

## 2.2 An Overview of the H1 Detector

The H1 detector [1] (illustrated in figure 2.1) is situated around the northern intersection of the two HERA beams, where magnets located within the detector itself bring the protons and positron beams into head-on collision. The detector measures approximately  $12\text{m} \times 10\text{ m} \times 15\text{ m}$  and weighs  $\approx 2800$  tonnes. It is designed to measure the direction, energy and charge of particles resulting from the  $ep$  collision at its very centre. An angular coverage of almost  $4\pi$  steradians is achieved, the main obstruction being the beam pipe itself. Cabling, cooling supplies and structural supports also impinge on the spatial coverage of the detector. Also shown is the H1 coordinate system, which defines the incoming proton direction to be  $+z$ . Cartesian and spherical coordinate sets are then defined with respect to this axis. For the spherical coordinate system,  $+z$  defines  $\theta = 0^\circ$ .

To record the consequences of an  $ep$  collision in as much detail as possible, the H1 detector relies principally on two particle detection methods – tracking and calorimetry. Tracking chambers immediately surrounding the interaction point measure the path of charged particles traversing them. These chambers are situated in a strong magnetic field of 1.15 T, allowing particle charge and momentum to be ascertained from the curvature of the path taken. This field is provided by the superconducting solenoid that encases the core of the detector (see label 6 in figure 2.1). Calorimeters surrounding the tracking chambers absorb almost all of the energy of incident particles. Fine segmentation of the calorimeters allows good spatial resolution of the incident particles, providing information not only on total energy and position, but also on the nature of the incident particle from the shape of the energy deposition.

Combining the information from these two detection methods allows measurements to be made over a wide range of particle momenta. Low momentum particles may not even reach the calorimeters, but their small radii of curvature allow their momenta to be accurately measured by the tracking chambers alone. High



- |                                   |                           |
|-----------------------------------|---------------------------|
| 1 Beam pipe and beam magnets      | 9 Muon chambers           |
| 2 Central track detectors         | 10 Instrumented iron yoke |
| 3 Forward track detectors         | 11 Forward muon toroid    |
| 4 Electromagnetic LAr calorimeter | 12 SPACAL and Backward DC |
| 5 Hadronic LAr calorimeter        | 13 PLUG calorimeter       |
| 6 Superconducting coil (1.15 T)   | 14 Concrete shielding     |
| 7 Compensating magnet             | 15 Liquid argon cryostat  |
| 8 Helium supply for 7             | 16 H1 coordinate system   |

Figure 2.1: A schematic diagram of the H1 detector.

momentum particles pass through the tracking chambers with very little curvature (“stiff tracks”) and hence the track information will have large errors, but the energy of such particles will be well measured in the calorimeters.

The detector is very asymmetric. Due to the asymmetry in the beam energies, the majority of the particles produced in an  $ep$  collision are thrown “forward” (the  $+z$  direction). Note that this asymmetry can be almost entirely attributed to the difference in the beam energies, not the difference between the  $e$  and  $p$  masses, since the beams are so highly relativistic.

H1 achieves as full an angular coverage as possible. This is of particular importance to this thesis, since neutrinos, one of the possible decay products of a  $W$ , are not directly detectable. Their presence in an event can only be inferred by a total transverse momentum imbalance in the detector.

## 2.3 Tracking

The tracking system of H1 provides track triggering and reconstruction. It is divided into two main regions, the central (CTD) and forward (FTD) tracking devices, each optimised for tracking and triggering in its angular region. The system is illustrated in figure 2.2. Track reconstruction is predominantly reliant on drift chambers. Rapid triggering depends on the fast response of multiwire proportional chambers.

Track reconstruction in the central region is based on two concentric drift chambers, CJC1 and CJC2 (Central Jet Chambers). The central inner (CIZ) and central outer (COZ)  $z$ -chambers are thinner drift chambers, designed to complement the measurements of the CJCs with a more accurate  $z$  measurement. All triggering in the tracking system uses multiwire proportional chambers (MWPCs), because of their rapid response time. The central inner proportional (CIP) and central outer proportional (COP) chambers are adjacent to the CIZ and COZ respectively.

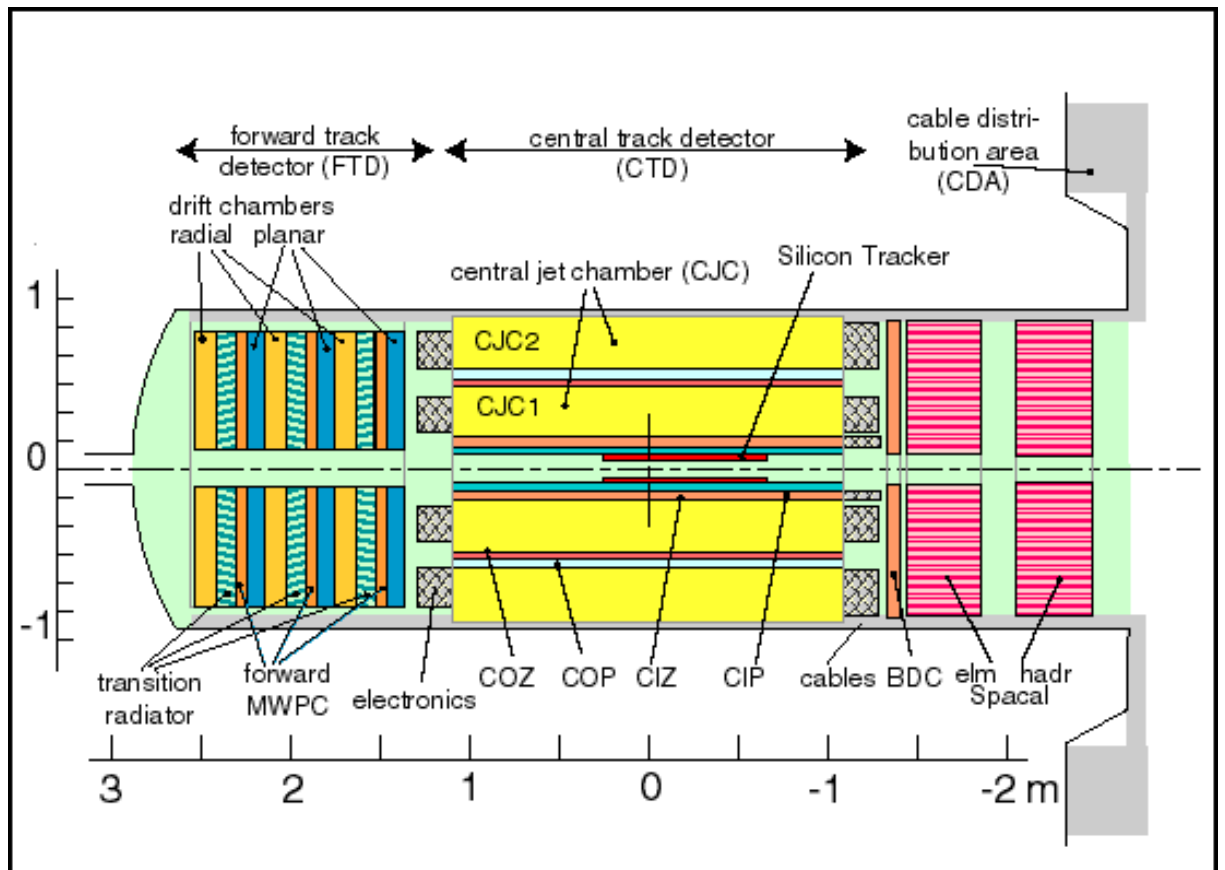


Figure 2.2: An  $r - z$  view of the tracking chambers, which immediately surround the beam pipe.



In the forward region ( $\theta < 30^\circ$ ) track reconstruction relies on the FTD, constructed from three supermodules. Each supermodule consists of three orientations of planar wire drift chambers, a multiwire proportional chamber (FWPC), a passive transition radiator and a radial wire drift chamber. In the backward region the Backward Drift Chamber (BDC) provides track reconstruction.

### 2.3.1 Central Jet Chambers

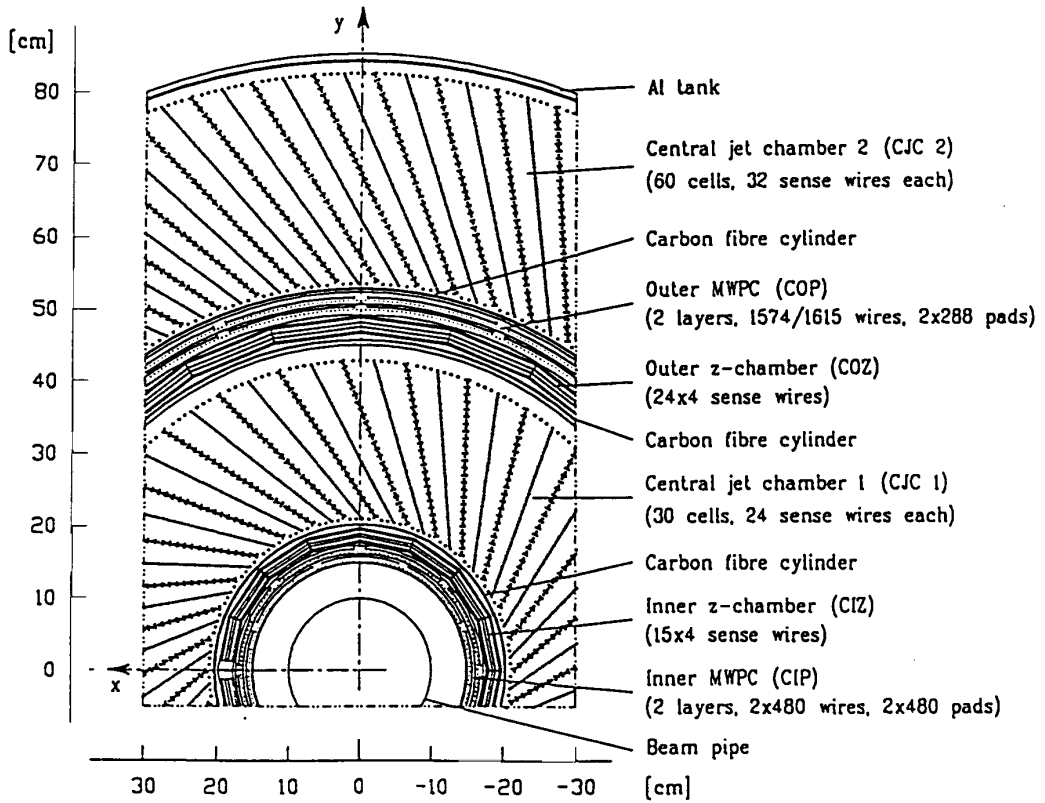


Figure 2.3: An  $r - z$  view of the tracking chambers.

CJC1 and CJC2 have planes of sense anode wires running parallel to the beam axis. Cells in each chamber extend azimuthally from the sense wire plane to each cathode wire plane, and radially over the full radial span of the chamber. Cells are

tilted by approximately  $30^\circ$  (see figure 2.3) so that stiff tracks pass through more than one cell, aiding the track position resolution, and eliminating reconstruction ambiguities by linking track segments from different cells. The cathode wires of each cell are set to a voltage proportional to the distance from the sense wire plane in order to create a uniform drift field and hence a constant drift velocity over almost the entire cell. At nominal HV the drift velocity is  $50 \text{ mm}/\mu\text{s}$  giving a resolution in the  $r - \phi$  plane of  $\sigma_{r-\phi} \approx 350 \text{ }\mu\text{m}$ . Since the sense wires are parallel to the  $z$  axis, the resolution in this direction is poor, because the measurement is reliant on charge division techniques. A resolution of  $\approx 1\%$  of the wire length is possible, or  $\sigma_z \approx 5 \text{ cm}$ .

### 2.3.2 Central $z$ Chambers

The CIZ and COZ chambers surround the inner half of the jet chamber, and complement the measurement of charged track momenta in CJC1 and CJC2. These chambers have the reversed orientation of sense wires and drift field to that of the jet chambers, i.e. their sense wires are strung in the  $r - \phi$  plane and their drift field is along the  $z$  direction. This allows an accurate measurement of the  $z$  coordinate from drift time measurements with a typical resolution of  $300 \text{ }\mu\text{m}$ . Conversely these chambers can only poorly constrain the  $r - \phi$  measurement from charge division.

### 2.3.3 Forward Tracking Detector

The layout of the FTD is shown in the left-hand part of figure 2.2. In each super-module, the planar drift chambers are located closest to the central tracker, since its homogeneous spatial precision in  $x$  and  $y$  is most suitable for linking tracks in the centre. The planars are designed to provide accurate  $\theta$  measurements. The FWPC (see section 2.3.5) is mounted directly behind the planars, since it shares the same gas mixture. After the FWPC particles traverse a transition radiator of

400 polypropylene foils, producing transition radiation photons which are detected in the radial chamber of each supermodule. The radials also provide accurate  $r - \phi$  information and a moderate radial measurement (by charge division). To improve track position resolution the second and third radial modules are rotated by  $3.75^\circ$  and  $2.5^\circ$  relative to the first.

### 2.3.4 Backward Drift Chamber

The Backward Drift Chamber (BDC) was constructed and installed as a part of the 1995 upgrade of the H1 Detector<sup>3</sup>. The main goal of this upgrade was to improve the ability to investigate  $ep$  events with the incident positron scattered through small angles (events with low  $Q^2$  and Björken  $x$  – see section 3 for definitions of these quantities). The BDC is shown in the right-hand part of figure 2.2.

The BDC consists of 8 layers in the  $z$  direction. In phi, each layer is divided into 8 sectors. Each sector consists of 32 drift cells. The 8 layers are paired up, and each pair is rotated by  $11.25^\circ$  with respect to the previous layer.

### 2.3.5 Multiwire Proportional Chambers

The rapid trigger decisions required by H1 are heavily dependent on its multiwire proportional chambers. Most importantly they must deliver a timing signal with a time resolution better than the separation of two successive HERA bunch crossings. The region of H1 seen by the interaction point between the polar angles of  $5^\circ$  and  $175^\circ$  is completely covered by multiwire proportional chambers (MWPCs). The MWPCs also provide track elements in the backward direction where the drift chambers fail to provide enough space points.

---

<sup>3</sup>The upgrade in 1995 replaced the BWPC (Backward Proportional Chamber) with the BDC. Since the great majority of the data presented in this thesis was taken with the BDC in place, only the BDC is described here. Description of the BWPC can be found in [1]

The forward proportional chambers (FWPC) are interspaced between the drift chambers of the FTD as described in 2.3.3. The CIP and COP are constructed from low mass materials to keep the track quality of particles traversing them and into the adjacent drift chambers as high as possible. The primary purpose of the FWPC and the CIP/COP is to provide space points for the  $z$ -vertex trigger.

## 2.4 Calorimetry

The H1 calorimeters can be subdivided into four main components: the Liquid Argon Calorimeter (LAr), the Spaghetti Calorimeter (SpaCal), the Tail Catcher (TC) and the Plug Calorimeter (PLUG). All four calorimeters function according to a similar principle. The calorimeter is constructed from two main components – “passive” layers of absorber material and “active” layers of sampling material. High energy particles traversing the absorber undergo multiple interactions with the absorber, producing secondary particles which also interact with the absorber, such that a shower of particles each with progressively lower energy develops. The energy of the shower is measured by the sampling layers.

Electrons or photons (electromagnetic particles) passing through an absorber layer rapidly lose energy through bremsstrahlung and pair production. The interaction of electromagnetic particles with matter is characterised by a radiation length,  $X_0$ , which is the mean distance in which the particle loses all but  $\frac{1}{e}$  of its initial energy. Lead, the most common electromagnetic absorber in H1, has a radiation length of 0.56 cm. If the shower is fully contained within the calorimeter, the energy of the incident particle is proportional to the amount of ionisation collected in the sampling layers.

Hadrons (strongly interacting particles) interact with the nuclei of the atoms of the absorber, both elastically and inelastically. This results in secondary hadrons,

and (as in the electromagnetic case) a shower of secondary particles develops. The characteristic scale over which such a hadronic shower develops, the interaction length  $\lambda_i$ , is typically much larger than  $X_0$  (lead and steel both have  $\lambda_i \approx 17\text{cm}$ ). The shower development stops when the secondary hadrons have sufficiently low energy to be stopped by ionisation or nuclear capture.

Not only is the longitudinal extent of a hadronic shower greater than that of an electromagnetic one, but also the lateral extent (due to Coulomb scattering). These two differences influence the relative location and design of the electromagnetic and hadronic calorimeters, and form the basis of differentiation techniques between particle types.

### 2.4.1 The Liquid Argon Calorimeter

The Liquid Argon Calorimeter (LAr) [2] (figure 2.4) is the main H1 calorimeter. It has full azimuthal coverage, and extends over the polar range  $4^\circ < \theta < 153^\circ$ , making it the main calorimeter used for the detection of the hadronic final state (HFS) and electron identification.

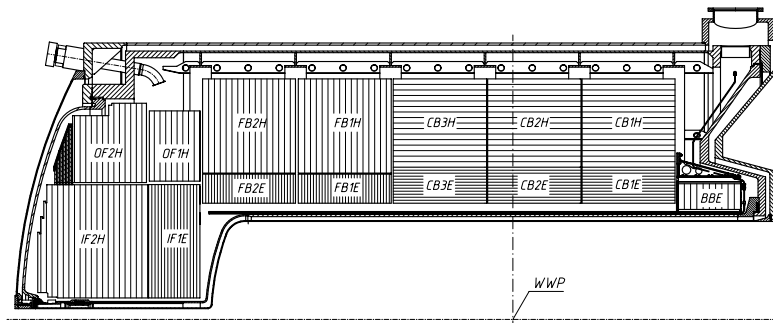


Figure 2.4: An  $r - z$  view of the upper half of the Liquid Argon Calorimeter. WWP (Wechselwirkungspunkt) is the interaction point.

The LAr has an electromagnetic (EMC) and a hadronic (HAC) section, the

former being located closer to the interaction point than the latter. The EMC uses 2.4mm thick plates of lead as an absorber, and the HAC uses 16mm stainless steel plates. Both sections use liquid argon as the sampling medium. Argon atoms are ionised by the shower particles, and the resulting charge is read out from rectangular cathodes, a few centimetres in size. Argon's high density results in an efficient production of the ionisation charge, and being a noble gas, the ionisation products do not undergo further inelastic scatters.

Both EMC and HAC are deepest in the forward region, where the greatest activity occurs in the detector due to the beam asymmetry. Here the EMC is  $\approx 30X_0$  deep and the HAC is  $\approx 7\lambda_i$  deep. The calorimeters become shallower towards the backward region, where they are  $\approx 20X_0$  and  $\approx 5\lambda_i$  deep respectively.

The LAr is highly segmented, and 45000 channels are read out. Readout channels from both the EMC and HAC are combined into 256 towers – groups of calorimeter cells radiating out from the interaction point. The sum response of these towers is used as the basis for the LAr triggers. The fine granularity of the calorimeter allows  $e/\pi$  discrimination at a level of  $10^{-3}$ , by keeping only those calorimeter cells associated with significant deposits of energy, and rejecting isolated activity consistent with noise. The LAr is a non-compensating calorimeter, meaning that its response to hadronic particles is  $\approx 30\%$  less than that for electrons and photons [2]. This difference is corrected for using software reweighting off-line [3].

Test beam studies of the LAr modules show an energy resolution consistent with  $\frac{\sigma_E}{E} \approx \frac{0.12}{\sqrt{E}} \oplus 0.01$  for electrons and  $\frac{\sigma_E}{E} \approx \frac{0.50}{\sqrt{E}} \oplus 0.02$  for charged pions<sup>4</sup>. The overall electromagnetic energy scale is currently known to 1.5%, by comparing the measured track momentum of electrons and positrons with their LAr energy deposition. By studying the transverse momentum balance in Neutral Current DIS events (see section 3.1), the hadronic energy scale is then verified to an accuracy of 4%.

---

<sup>4</sup>Unless otherwise stated, energies are always given in units of GeV.

## 2.4.2 The SpaCal

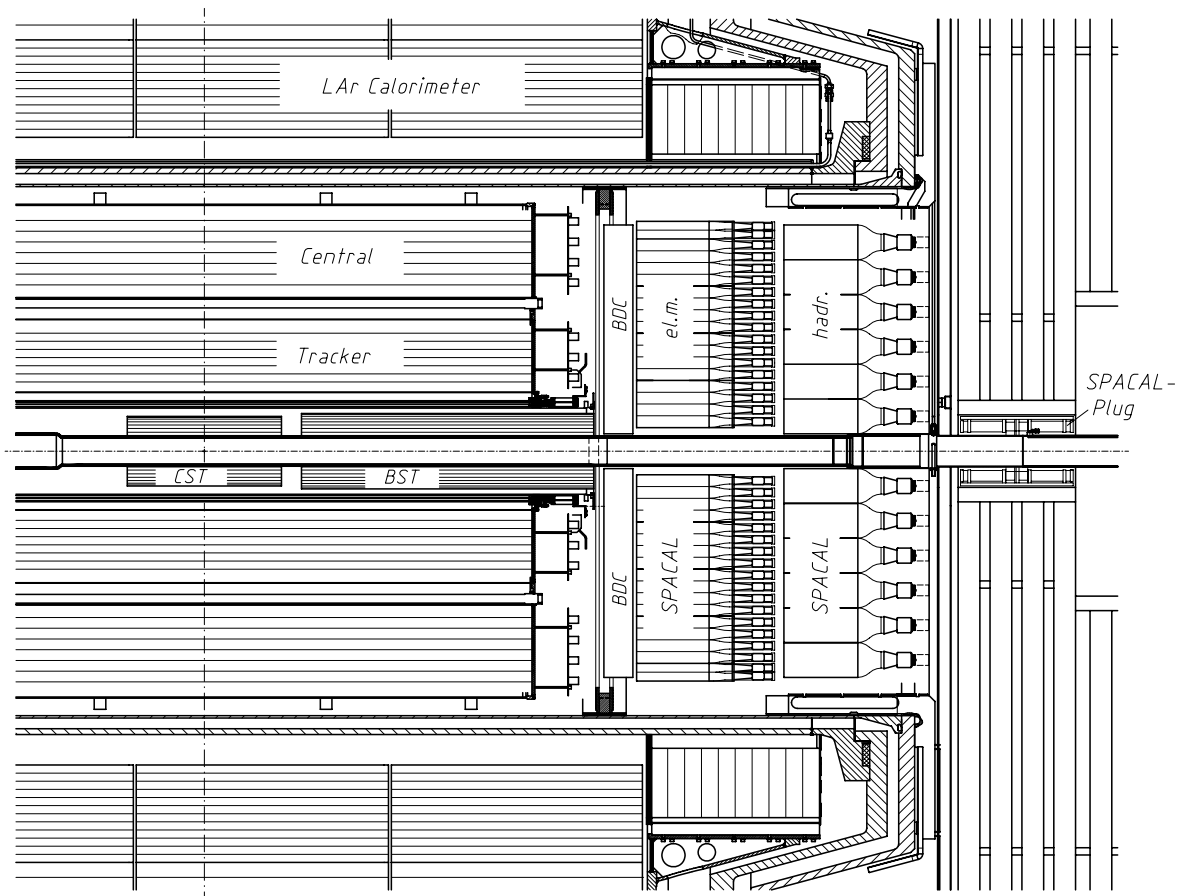


Figure 2.5: A view of the SpaCal. The point where the vertical dotted line crosses the CST is the interaction point (WWP).

The SpaCal<sup>5</sup> calorimeter [4], shown in figure 2.5, is situated in the backward region of the detector covering an (electromagnetic) angular range of  $153 < \theta < 177.5^\circ$ . Like the LAr calorimeter, it is a non-compensating sampling calorimeter, and is divided into electromagnetic and hadronic sections. The active region of the SpaCal consists of scintillating fibres embedded in lead sheets. Incident particles shower in the lead causing the fibres to scintillate. This light is collected at one end of

<sup>5</sup>SpaCal - Spaghetti Calorimeter - a reference to the long, thin nature of the scintillator material used in this calorimeter.

the fibre by a photomultiplier tube. The electromagnetic section contains 1192 cells, each of which consists of 26 grooved lead plates interspersed with 2340 scintillating fibres 0.5 mm in diameter. The cells are 250 mm deep and have a lead:fibre ratio of 2.27:1. This yields a radiation length of 9 mm (27.8 radiation lengths in total). The energy resolution has been measured to be  $\frac{\sigma_E}{E} = \frac{7.1\%}{\sqrt{E}} \oplus 1.0\%$  [5]. The hadronic section is similar to the electromagnetic section although has fewer, larger cells, reflecting the greater lateral extent of hadronic showers: 136 cells with a lead:fibre ratio of 3.4:1. This yields another interaction length, the first being provided by the electromagnetic section of the SpaCal. The energy resolution of the hadronic section has been measured to be  $\frac{\sigma_E}{E} = \frac{56\%}{\sqrt{E}} \oplus 3.0\%$  [6]. The combined response of the electromagnetic and hadronic sections of the calorimeter has been studied using a 4 GeV  $\pi^-$  beam, showing the combined energy scale to be known to  $\approx 5\%$  and the resolution (at this energy) to be  $\frac{\sigma_E}{E} = (29 \pm 2)\%$  [7].

### 2.4.3 The Tail Catcher

The iron return yoke of the main H1 magnet (see figure 2.1) is instrumented with 16 layers of limited streamer tubes and 11 of these are used to detect ionisation caused by hadronic showers leaking out of the LAr [8]. This “tail catcher” provides a coarse measurement of this energy leakage, with a resolution of 100% and a scale uncertainty, determined from cosmic muon data, of approximately 35%.

### 2.4.4 The Plug Calorimeter

The Plug calorimeter [9] is also located in the return yoke of the magnet, situated in the forward region of the detector (see figure 2.1), covering the gap in acceptance between the LAr calorimeter ( $\theta \approx 4^\circ$ ) and the beam pipe ( $\theta \approx 0.3^\circ$ ). It is a silicon instrumented sampling calorimeter, with passive copper layers. Eight planes, each containing 84 detectors, are read out through 336 channels (for simplicity



pairs of detectors are ganged together). The energy resolution is limited by the coarse sampling and the incomplete containment of showers and is estimated to be  $1.50/\sqrt{E}$  [1].

## 2.5 The Muon Systems

### 2.5.1 The Instrumented Iron

The iron return yoke of the magnet is used to detect muons, as well as being used as the Tail Catcher (see section 2.4.3). The central muon trigger [10] searches for track segments using coincidence information from 5 of the 16 layers in each of the six regions (inner and outer, forward and backward endcap, and forward and backward barrel). A signal is required in at least 3 of the 5 layers for all regions except the forward inner endcap, where the particle flux is very high due to the proximity of the outgoing proton beam. In this region 4 layers must fire in coincidence.

### 2.5.2 The Forward Muon Detector

The Forward Muon Detector (FMD) [11] is located outside the main detector (see figure 2.1), covering an angular range of  $3 < \theta < 17^\circ$ . It is illustrated in figure 2.6. This is a highly active angular region of the detector, surrounding the outgoing proton remnant. The location of the FMD outside both the calorimeters and the instrumented iron, makes possible the identification of muon tracks extrapolated from the FTD. Identification of these tracks using the FTD alone would be extremely difficult due to the high multiplicity of tracks in this region.

The FMD consists of six double layers of drift chambers, three either side of a toroidal magnet (figure 2.6a), providing a magnetic field of about 1.5 T. The toroid curves the passage of muons, allowing a momentum ( $p$ ) measurement to be made

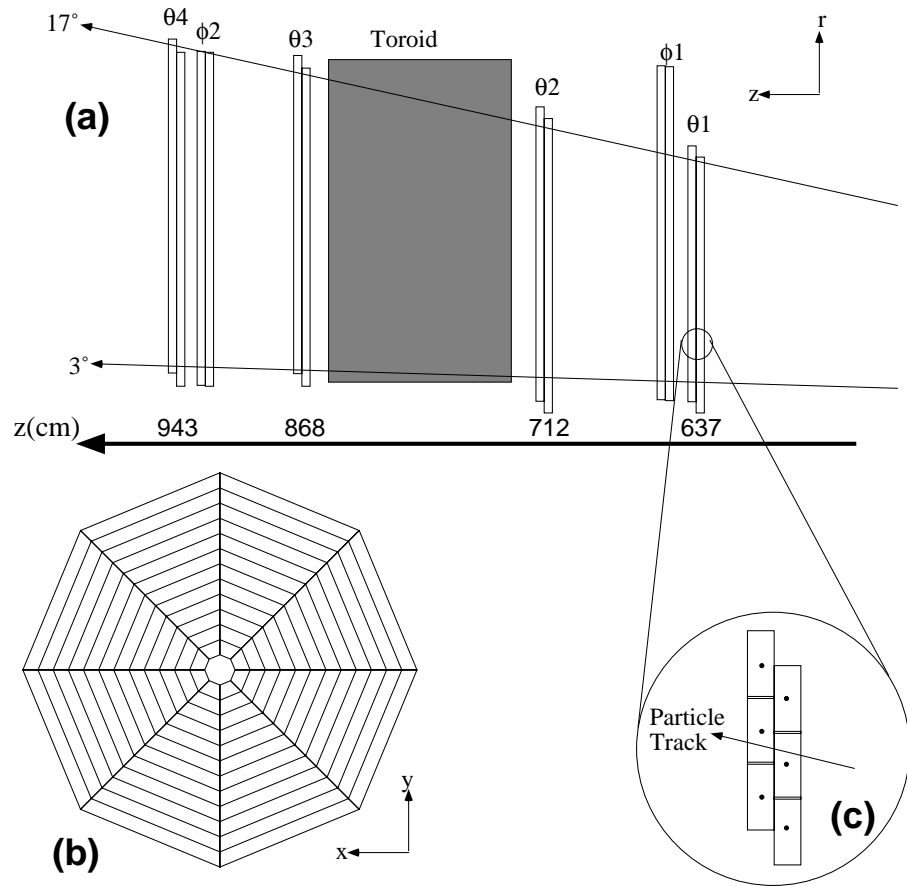


Figure 2.6: The Forward Muon Detector. (a) A side view showing muon paths at the extremes of coverage. (b) A  $\theta$ -layer of the FMD. (c) The off-setting of cells to avoid reconstruction ambiguities.

independently of the CTD and FTD. This measurement is possible over the range  $5 < p < 100$  GeV. The lower limit is set by multiple Coulomb scattering – on average a muon loses 3 GeV in the main detector and 1.5 GeV in the toroid. The upper limit is set by the angle through which a high momentum muon can be deflected by the toroid. Four of the six layers have their sense wires strung tangential to the beam pipe to measure most accurately in  $\theta$  (figure 2.6b) and two layers have their sense wires strung azimuthally, to measure accurately in  $\phi$ . Each drift cell is 20 mm deep and 120 mm wide with a sense wire located in the middle. The spatial resolution of these cells is  $\approx 250$   $\mu\text{m}$  from drift time and  $\approx 4$  cm from charge division techniques. The two layers of each section are offset with respect to each other to eliminate the ambiguity of which side of a sense wire the muon passed. This is illustrated in figure 2.6c.

## 2.6 Time-of-Flight Detectors

The Time-of-Flight (ToF) [12] detectors are vital to the rejection of non  $ep$  interactions within H1, because genuine  $ep$  collision events occur at a much lower rate than these “background” processes. Beam-gas and beam-wall events can be differentiated from  $ep$  collisions by suitably placed scintillation detectors with good timing resolution, since these background events will occur at approximately the same time as the proton bunch passes through the scintillator, whereas events originating from an  $ep$  collision at the interaction point will occur marginally later or earlier, namely  $\approx 2\Delta z$ , where  $\Delta z$  is the distance along the beam pipe between the interaction point and the scintillator. The ToF systems, constructed from plastic scintillator, are located near the beam pipe in the backward endcap of the return yoke (BToF), within the PLUG calorimeter (PToF) and near the FMD (FToF). In addition, the “Veto Wall”, a double set of scintillators positioned behind the return yoke, detects particles from the proton beam-halo. This is a shower of particles, mainly muons,

which accompanies the proton beam, caused by the inelastic collision of protons with residual gas or hardware far upstream from the detector.

## 2.7 The Luminosity System

An accurate knowledge of the luminosity produced by HERA within H1 is essential for the calculation of cross-sections and predicted event rates. The luminosity is measured by observing the rate of a process with an extremely well known cross-section, the Bethe-Heitler process [13],  $ep \rightarrow ep\gamma$ . The luminosity system [14] consists of two main components, the Electron Tagger (ET) and the Photon Detector (PD). These are situated in the backward direction at  $z = -33.4$  m and  $z = -102.9$  m respectively.

Both detectors are Čerenkov calorimeters. The ET is a  $7 \times 7$  array of crystals, and the PD is a  $5 \times 5$  array. An online measurement of the luminosity is made from Bethe-Heitler events, which are registered by the system when hits are observed in the ET and PD in coincidence. The rate of these events, corrected for detector acceptances and background processes, is used to calculate a luminosity measurement which is used by HERA as the beams are steered to optimise the luminosity delivered to the experiment.

The final luminosity, used for physics analyses, is calculated off-line from the rate of scattered photons alone. Corrections are made for the contributions from proton satellite bunches, which can contribute up to 10% of the proton current. Background contributions are also subtracted, the main process being bremsstrahlung from electrons in the electromagnetic fields of the residual gas in the beam pipe.

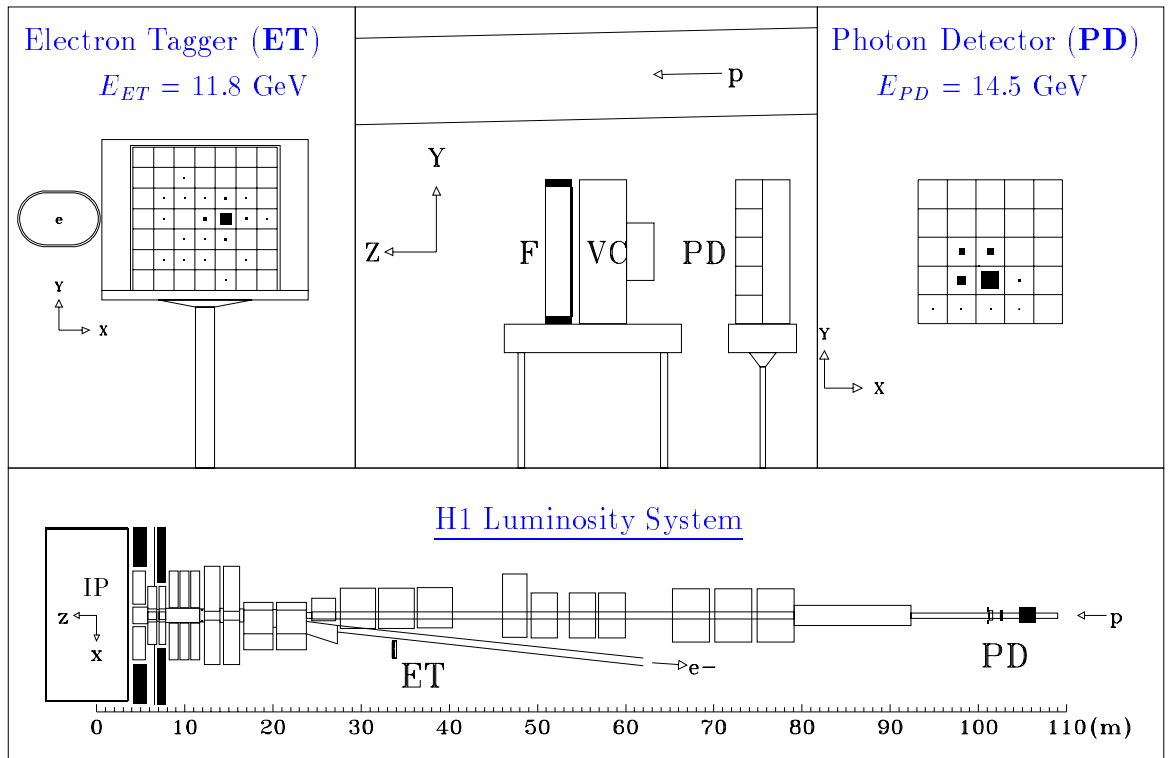


Figure 2.7: The luminosity system.

## 2.8 Triggering and Data Acquisition

Currently, HERA has the fastest bunch crossings of any collider facility in the world with bunch crossings every  $96 \text{ ns}$ <sup>6</sup>. Modern detector technology and electronics cannot process and read out the full detector information from H1 ( $\approx 270\,000$  channels) in this time interval. Instead, a layered triggering system is employed which “decides” whether to keep an event or not, whilst the information being read out from the detector is pipelined (buffered). At each bunch crossing, all subdetector components of H1 send eight *bits* of information (*trigger elements*) to

<sup>6</sup>The LHC being constructed at CERN will have bunch crossings every  $25 \text{ ns}$ .

the central trigger [15]. Reading out this information from all the subdetectors takes approximately 22 further bunch crossings ( $\approx 2.1 \mu\text{s}$ ). The central trigger combines the 200 trigger elements into 128 *subtriggers*. The decision to keep or reject an event is then based on these subtriggers. This is level 1 (L1) of the triggering system. Different physics processes occur with very different rates, so prescales are introduced for selected subtriggers. A prescale of  $x$  for a given subtrigger means that L1 only passes 1 in  $x$  of these events to the next level. This prevents the system's bandwidth being swamped by a few, common subtriggers. When an event is accepted by the central trigger, an "L1Keep" signal is sent out, the pipelining ceases, and the event information is passed to level 2 (L2).

The L2 trigger is divided into two sections – the topological trigger (L2TT) [16] and the neural network (L2NN) [17]. These two systems combine information from different trigger systems, allowing decisions to be based on the correlation between different subdetectors. When an "L2Keep" signal is sent, the entire event information is read into the Central Event Builder (CEB) of level 4 (L4)<sup>7</sup>. Once this reading is complete, the pipelining recommences. This process means that the pipelining is typically stopped for 1-2 ms per event. The running total of these stopped periods is referred to as "deadtime". The experiment, running under optimum conditions, operates with about 7% deadtime, although overall an average of nearer 10% is typical.

L4 is a farm of microprocessors, consisting of around 30 Power PC boards. It processes up to 30 events, asynchronous to the other trigger levels, performing a limited reconstruction of each event. Online software applies further cuts at this level, depending on the subtriggers that fired for the event. The great majority of beam-gas, beam-wall and cosmic induced events are rejected at this stage as well as trigger noise, and L4 writes data events to tape at a rate of about 10 Hz. L4 can process events at an input rate of around 50 Hz, above which deadtime accumulates.

---

<sup>7</sup>Level 3 is yet to be implemented at H1.

The full reconstruction and classification of events is done offline by level 5 (L5). L5 is a dedicated SGI workstation, which reconstructs all individual subdetectors and also links charged track segments and calorimeter clusters to complete the overall description of the event. L5 classifies events into classes – groups of events exhibiting similar physics signatures. The full output of L5 is written to Production Output Tapes (POTs). A compressed version, containing a simplified information set sufficient for most analyses, is written to Data Summary Tapes (DSTs). Events on the DSTs are typically 10 kB, allowing them to be written to disk for rapid access.

## 2.9 Trigger Efficiencies

As described in 2.8, the H1 data acquisition system utilises 128 subtriggers, which recognise key topological features of interesting physics processes, to initiate the data processing and recording procedure. This analysis uses the five subtriggers developed for the H1 Charged Current (CC) analysis [18,19]. These subtriggers are based on two main trigger elements – LAr\_Etmiss (an imbalance of energy deposits measured in the LAr calorimeter) and LAr\_electron (an energy deposit typical of a high energy electron in the LAr calorimeter). Since CC processes (and real W production processes) are comparatively rare, none of these subtriggers is prescaled (see section 2.8).

Whilst these five subtriggers are carefully designed to identify CC processes, they cannot do so perfectly, and it is important to study and quantify their efficiencies, so that corresponding corrections may be made to the Monte Carlo simulations.

### 2.9.1 The “Pseudo-CC” Sample

Due to the relative infrequency of CC events (see section 3.3), studies of the efficiency of these triggers are hampered by the small data sets. To allow these studies to be performed on a larger sample a “pseudo-CC” technique has been developed [20]. A large Neutral Current (NC) data set is converted to a pseudo-CC data set by removing the identified scattered beam electron from all subdetectors. The event itself is then indistinguishable from a real CC event. Each event in the sample is finally re-weighted to the CC cross section, so that distributions in key kinematic quantities are correctly reproduced. This method relies on the assumption that the hadronic final state in NC and CC events is very similar. Previous studies have confirmed this [21].

### 2.9.2 Determining the Trigger Efficiencies

The trigger efficiency for the pseudo-CC sample is then defined as

$$\epsilon = \frac{\text{Sum of all weights of pseudo-CC events firing at least one subtrigger}}{\text{Sum of all weights of entire pseudo-CC data set}} \quad (2.1)$$

These efficiencies are calculated double-differentially – with respect to  $p_T^X$  and  $\gamma$  (the transverse momentum and polar angle of the hadronic final state respectively).

The efficiencies are then fitted by a function of the form

$$f(x) = A - B e^{C \cdot x} \quad (2.2)$$

where  $x = p_T^X$ . (A,B,C) are free parameters determined by the function minimisation package MINUIT [22]. The entire data sample presented in this thesis covers the period 1994 to 2000. The function is fitted separately for four subdivisions of this data set (1994-1996, 1997, 1998 and 1999-2000). This is done because of minor



differences in the trigger definitions between these sets. The trigger efficiencies for the latest period are shown in figure 2.8.

The appropriate function is used to reweight the Monte Carlo simulations, so that the kinematic regions where the efficiency for triggering on real data is less than 100% are accurately modelled.

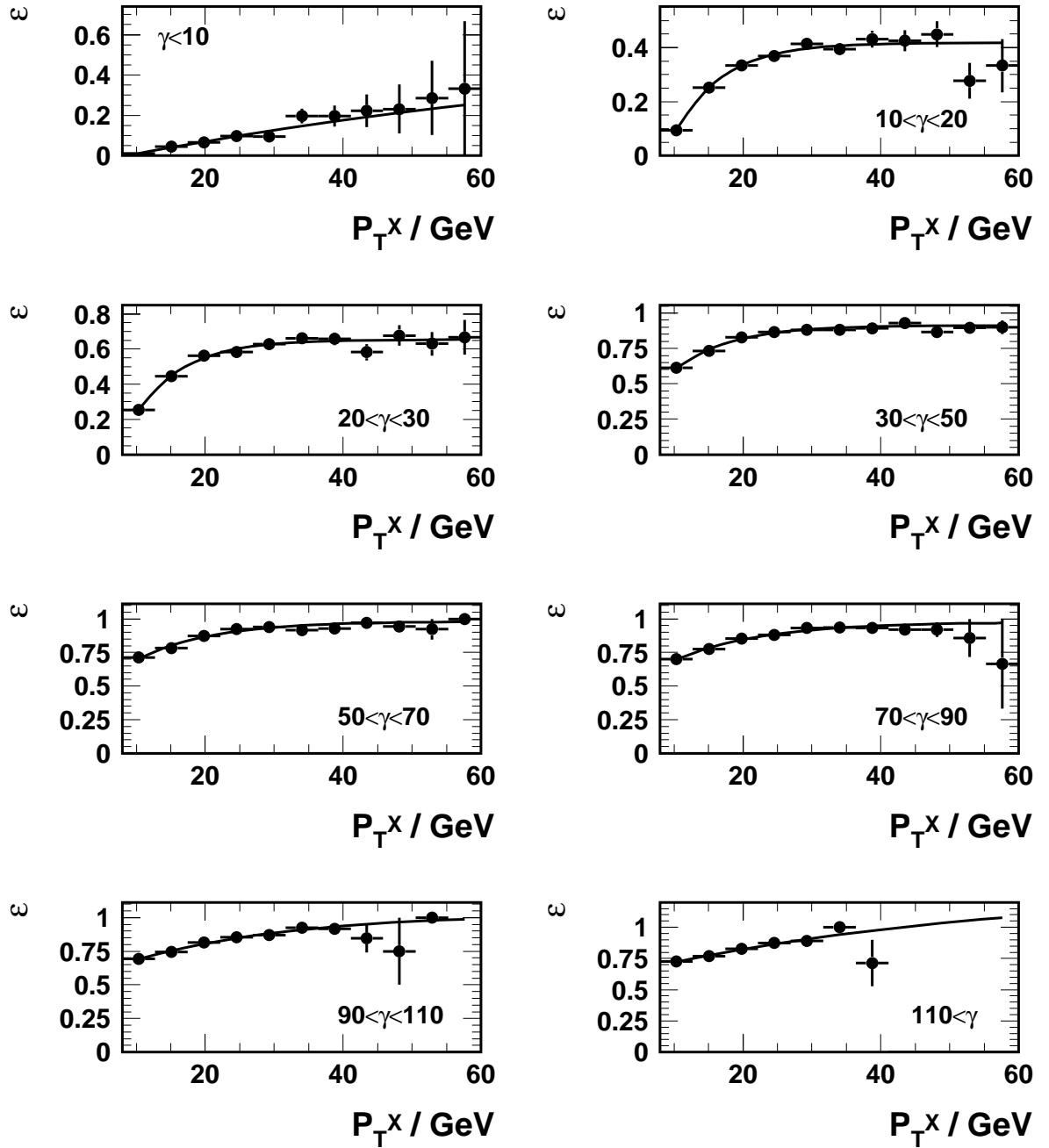


Figure 2.8: The combined trigger efficiency for all subtriggers as a function of  $P_T$  for different ranges of  $\gamma$ , calculated using pseudo-CC events taken in 1999-2000. The fitted function is shown as the solid line.  $\gamma$  is the polar angle of the hadronic final state.

# Chapter 3

## Theory

This chapter outlines the theoretical background necessary to understand the work presented within the context of HERA physics. A detailed presentation of Quantum Electrodynamics (QED) and Quantum Chromodynamics (QCD) is not appropriate here. The mechanisms of  $W$  production are briefly discussed, and are examined in more detail in section 4.2.

### 3.1 Electron Proton Scattering

The “collision” of an electron and proton at HERA commonly involves the exchange of a single boson. This can be a photon ( $\gamma$ ) or  $Z^0$  in the case of neutral current (NC) scattering, or a  $W^\pm$  in charged current (CC) scattering. These two types of interaction are shown in figure 3.1.

The incident electron and proton have four-momenta  $k = (E_e, \mathbf{k})$  and  $p = (E_p, \mathbf{p})$  respectively, while the scattered lepton has four-momentum  $k' = (E_l', \mathbf{k}')$ . The outgoing hadronic final state is generically labelled  $X$ , which may be the original proton if the scatter is elastic, or a more complex object, consisting of the proton remnant

and the struck quark, if the scatter is inelastic. The latter scenario dominates at high energy colliders such as HERA.

## 3.2 Kinematics

A schematic diagram of single boson exchange at lowest order in QED and QCD is shown in figure 3.2.

The squared centre-of-mass energy of the interaction is given by

$$s = (k + p)^2 \tag{3.1}$$

Through the exchange of the gauge boson, four momentum is transferred between the incident particles. This is traditionally represented by  $Q^2$ , the four-momentum transfer squared, which is defined as

$$Q^2 = -q^2 = -(k^\mu - k'^\mu)^2 \tag{3.2}$$

When the exchanged boson is a photon,  $Q^2$  represents its “virtuality”. For  $Q^2 \ll 1 \text{ GeV}^2$  the photon is almost real, or on mass shell. This class of interactions is known as photoproduction.  $Q^2$  also represents the spatial resolving power of the interaction. The greater  $Q^2$  the smaller the structure within the proton that may be measured. The size of the proton is of the order of  $10^{-15} \text{ m}$ , which corresponds to  $Q^2 \approx 1 \text{ GeV}^2$ , so for  $Q^2$  greater than this, the substructure of the proton may be resolved, and this class of interactions is known as deep inelastic scattering (DIS).

$Q^2$  is Lorentz-invariant. Two other Lorentz-invariant quantities are traditionally defined, which may also be employed to describe the kinematics of the interaction:

$$x = \frac{Q^2}{2p \cdot q} \tag{3.3}$$

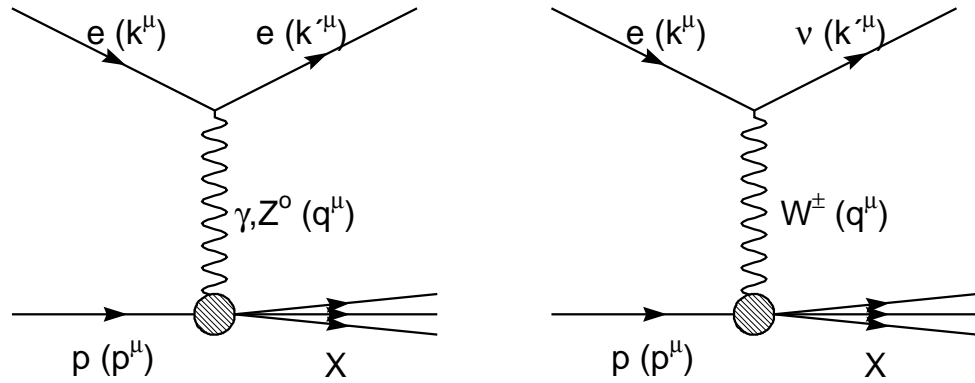


Figure 3.1: Single boson exchange : NC and CC. The quantities in brackets are the four-momenta of the labelled particles.

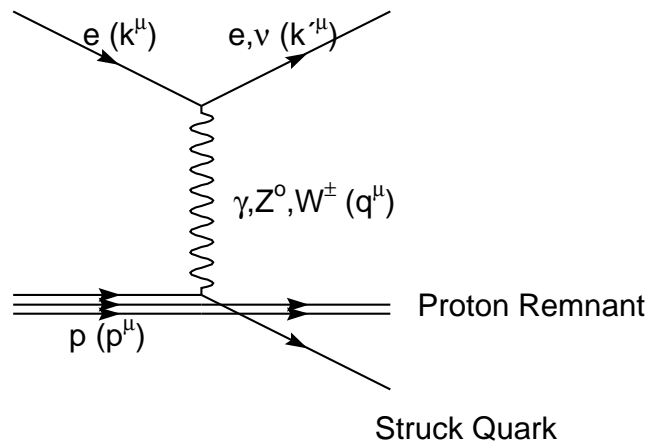


Figure 3.2: Deep inelastic scattering (DIS) at lowest order in QED and QCD.

and

$$y = \frac{p \cdot q}{k \cdot p} \quad (3.4)$$

Both  $x$  and  $y$ , by definition, are constrained to take values between 0 and 1.  $x$  may be interpreted<sup>1</sup> as the fraction of the proton's momentum carried by the struck quark.  $y$  is the fraction of the electron's energy carried by the photon, in the rest frame of the proton, i.e. the frame in which HERA collisions are equivalent to fixed target collisions with an incident electron energy of  $\sim 50$  TeV.

Having defined  $Q^2$ ,  $s$ ,  $x$  and  $y$ , the kinematic system is now *over-constrained*, that is only two<sup>2</sup> of these are independent, since the four are related by

$$Q^2 = sxy \quad (3.5)$$

### 3.3 Deep Inelastic Scattering

The scattering of an electron off a proton via the exchange of a single photon may be described, at lowest order in QED, in terms of two *structure functions*,  $F_1(x, Q^2)$  and  $F_2(x, Q^2)$ , which themselves are dependent on the distribution of electric charge within the proton. These structure functions determine the  $ep$  cross section in the following form,

$$\frac{d^2\sigma_{ep \rightarrow eX}}{dx dQ^2} = \frac{4\pi\alpha_{em}^2}{xQ^4} [xy^2 F_1(x, Q^2) + (1-y)F_2(x, Q^2)] \quad (3.6)$$

where  $\alpha_{em}$  is the electromagnetic fine structure constant. Interactions involving the exchange of a  $Z^0$  (or, in the case of charged current interactions, the exchange of

---

<sup>1</sup>Strictly speaking this is only valid in the *quark parton model*, where the partons are assumed to be massless and to have no transverse momentum.

<sup>2</sup>In principle three are independent, but in practice at HERA  $s$  is fixed

a  $W^\pm$ ) only contribute at high  $Q^2$ , since the large masses of these bosons suppress the cross section by the factor

$$\frac{\sigma(Z^0, W^\pm)}{\sigma(\gamma)} \propto \left| \frac{Q^2}{Q^2 + M_{Z^0, W^\pm}^2} \right|^2 \quad (3.7)$$

with respect to that for photon exchange. This is illustrated in figure 3.3 by the fact that the charged current cross section is greatly suppressed with respect to the neutral current cross section until  $Q^2$  of greater than the vector boson masses squared ( $\mathcal{O} 10^4 \text{ GeV}^2$ ).

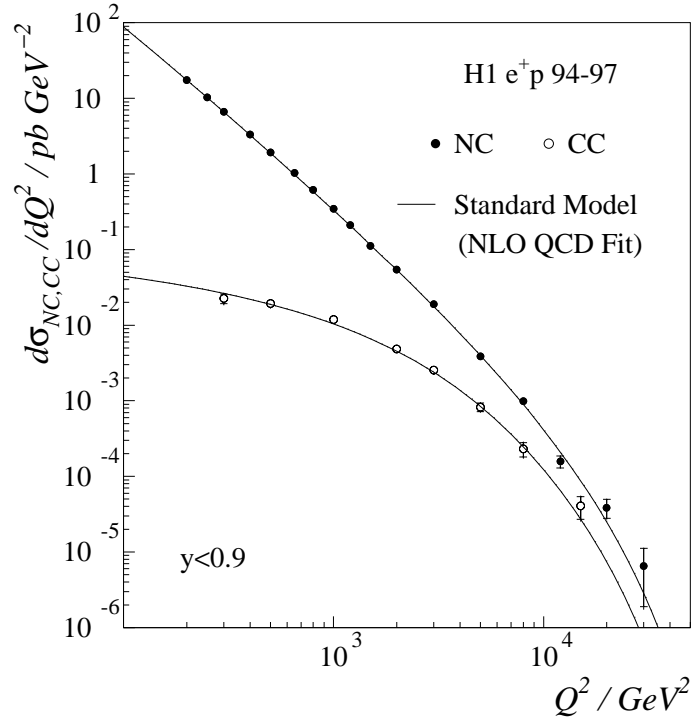


Figure 3.3: The differential neutral and charged current cross sections with respect to  $Q^2$  showing the suppression of the charged current cross section due to the  $W$  mass. Taken from [19].

It can be shown [25] that  $F_1(x, Q^2)$  and  $F_2(x, Q^2)$  are related to the photo-absorption cross sections for longitudinally and transversely polarised photons,  $\sigma_L$  and  $\sigma_T$ , by

$$\sigma_L = \frac{4\pi^2\alpha_{em}^2}{Q^2}(F_2 - 2xF_1) \quad (3.8)$$

$$\sigma_T = \frac{4\pi^2\alpha_{em}^2}{Q^2}2xF_1 \quad (3.9)$$

and hence, defining the photo-absorption ratio

$$R(x, Q^2) = \frac{\sigma_L(x, Q^2)}{\sigma_T(x, Q^2)} \quad (3.10)$$

allows equation 3.6 to be written

$$\frac{d^2\sigma_{ep\rightarrow eX}}{dx dQ^2} = \frac{4\pi\alpha_{em}^2}{xQ^4} \left[ xy^2 F_1(x, Q^2) + \frac{y^2}{2[1 + R(x, Q^2)]} \right] F_2(x, Q^2) \quad (3.11)$$

This formalism may be further simplified within the framework of the Quark Parton Model (QPM) [23], which considers the proton to consist solely of quarks which do not interact with each other (also described as *partons*). Within this model  $F_1(x, Q^2)$  and  $F_2(x, Q^2)$  are related by

$$2xF_1(x, Q^2) = F_2(x, Q^2) \quad (3.12)$$

the Callan Gross relation [24]. It is therefore possible to formulate the differential  $ep$  cross section in terms of a single structure function  $F_2(x, Q^2)$ .  $F_2$  has now been measured by H1 over a wide range of  $x$  and  $Q^2$ , and this measurement is shown in figure 3.4.



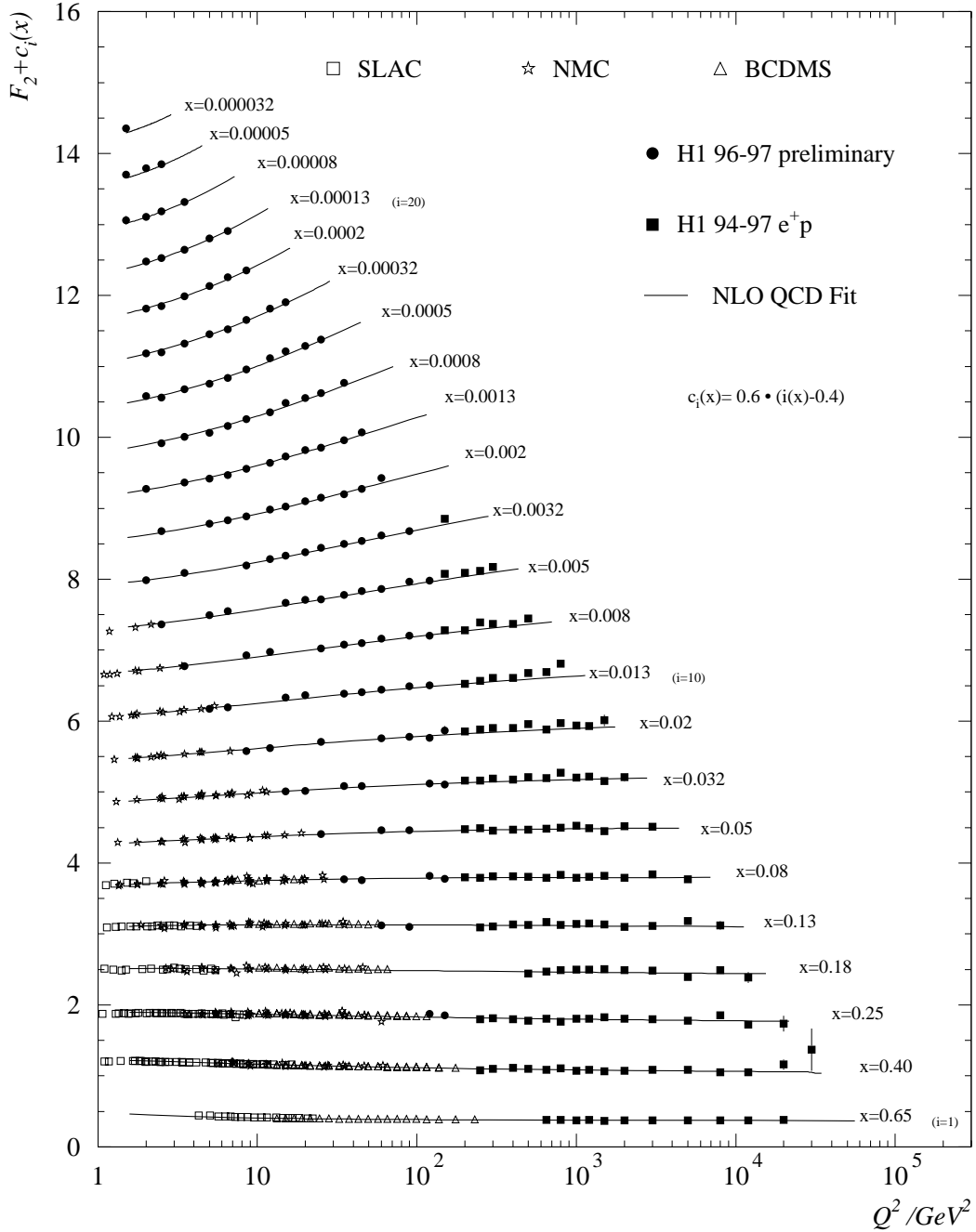


Figure 3.4: The structure function  $F_2(x, Q^2)$  as a function of  $Q^2$ , as measured by H1, and by fixed target experiments, for a range of  $x$  values. The solid squares are data presented in [18]. The solid triangles are H1 data for  $Q^2 > 150 \text{ GeV}^2$  from [26]. The curves are a NLO fit performed by H1 [19].  $c_i(x)$  is an arbitrary vertical displacement added for visual clarity.

It can be seen from figure 3.4 that  $F_2(x, Q^2)$  has little dependence on  $Q^2$  for the lower energy, fixed target data from SLAC [27], NMC [28] and BCDMS [29]. This phenomenon is known as *scaling* or *scale invariance* [30], and is explicable in the QPM, where the partons do not interact with each other. The point-like nature of the interaction leaves no scale in the process, and scale invariance automatically follows. However, the non-interaction of quarks is contrary to experience, since they are never observed individually, but rather always as bound states, either in mesons or baryons. This contradiction may be understood, when the *running* of the strong coupling constant,  $\alpha_s$ , is considered. A recent H1 measurement of  $\alpha_s$  as a function of  $Q^2$  is shown in figure 3.5(a). At low  $Q^2$  the coupling becomes very large and the partons interact strongly. At higher  $Q^2$  the coupling becomes weaker, to the extent that at sufficiently high  $Q^2$  the quarks in the proton may be considered as non-interacting.

The structure function  $F_2$  has a clear dependence on  $x$ , as can be seen in figure 3.5(b). In order to explain this in terms of a parton model it is necessary to include a sea of quark-antiquark pairs and gluons. It is these “sea” quarks that drive the low- $x$  behaviour of the structure function.

To describe and explain these distributions more rigorously than is possible with the naïve quark parton models, it is necessary to invoke the colourful magic of Quantum Chromodynamics (QCD). Only a cursory overview is given here. For a very readable introduction see [32]. For a little more detail see [33]. For a more rigorous approach see [34]. QCD is a non-Abelian gauge theory, describing the interaction of quarks and gluons, both of which carry colour charge. QCD is based on the gauge group  $SU(3)$ , invariant under colour transformations. A crucial feature of QCD is its non-Abelian nature, meaning that gluons can couple to other gluons – it is this feature of QCD that gives it its scale dependent coupling strength.

Calculations in QCD are possible via the expansion of series in orders of  $\alpha_s$ . These perturbative expansions are only feasible where  $\alpha_s$  is small enough. This

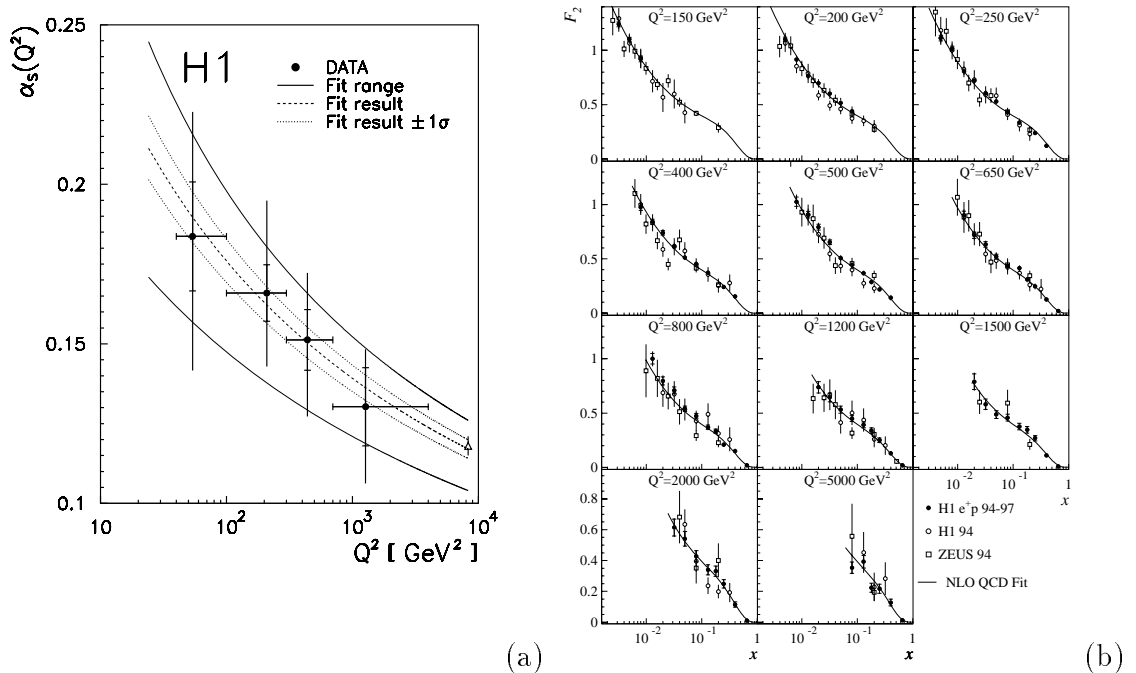


Figure 3.5: (a) A measurement of the strong coupling constant  $\alpha_s$  at different values of  $Q^2$ . Taken from [31]. (b) The structure function  $F_2$  shown as a function of  $x$ , in  $Q^2$  bins ranging from 150 GeV<sup>2</sup> to 5000 GeV<sup>2</sup>. Taken from [19].

occurs where the process contains a hard enough scale (e.g.  $Q^2$ ) to make  $\alpha_s$  small enough for *perturbative QCD* to be valid.

### 3.4 Hadronisation and Jets

The running of the strong coupling constant,  $\alpha_s$ , has two experimental effects of note here. Firstly, the short-distance behaviour of the strong interaction – the weakening of  $\alpha_s$  – allows quarks in the proton to behave as almost free partons (giving, to some extent, the observed scaling of  $F_2$ ). Secondly, the long-distance behaviour of the strong interaction – the strengthening of  $\alpha_s$  – leads to a phenomenon known as “confinement”. Free quarks are not observed, yet the process by which the partons which participate in high energy collisions convert into the hadrons which spray

out into detectors such as H1 is not fully understood. In particular the formation of “jets” has been the subject of considerable, ongoing study [35]. The formation of a jet can be treated in two stages. Firstly, the process by which an exiting participant from the original interaction radiates further quarks and gluons, known as *parton showering*. Secondly, the process by which these many individual partons organise themselves into the final state particles observed in the detector, known as *hadronisation*.

### 3.5 Photoproduction

Photoproduction is strictly defined as interactions where  $Q^2 = 0$ ; however, a common experimental definition of photoproduction is a process in which the scattered beam electron is lost in the outgoing beam pipe. This is because  $Q^2$  is never actually zero, but peaks at very small values, when the electron is scattered at a very low angle. At H1, if the scattered electron is not “tagged” (i.e. detected in any part of the detector, including the electron taggers at 33 m and 44 m downstream) then  $Q^2 < 0.01\text{GeV}^2$ . Photoproduction processes may either be “direct” or “resolved”. In the former case, the photon interacts directly with a quark from the proton (figure 3.6(a)). In the latter case, the photon fluctuates into a hadronic state, part of which then interacts with the proton (figure 3.6(b,c)).

The great majority of the photoproduction cross section at HERA is “soft” i.e. involves low energy interactions. However, high transverse momentum ( $P_T$ ) jets may be produced, allowing pQCD calculations to be made using the high  $P_T$  as the hard scale for the process. Such jets are typically produced in pairs (*di-jet production*) via the resolved processes illustrated in figure 3.6(b,c). These processes are sensitive to the quark and gluon content of the photon [36].

## 3.6 $W$ production

HERA is the first ever  $ep$  collider and it operates at a sufficiently high centre-of-mass energy to produce real  $W$  bosons. The typical leading order Feynman diagram for  $W$  production in  $ep$  collisions is shown in figure 3.7. The diagram is, in essence, very similar to figure 3.2, with the additional radiation of a  $W$  boson from the struck quark. The  $Q^2$  spectrum of the neutral current interaction is dominated by the exchange of low  $Q^2$  photons, and hence  $W$  production via a diagram such as this typically happens at  $Q^2 \sim 0$  GeV. Previous studies by H1 [37] have shown that the scattered electron is expected to be observed in the calorimeters ( $\theta < 178^\circ$ ) in 25% of the events. Further discussion of the production mechanism can be found in section 4.2.

Real  $W$  production at HERA is a comparatively rare event. The bremsstrahlung of an on-shell  $W$  from a quark is suppressed by the large mass of the  $W$ , giving an expected [38] total cross section of around 60 fb per charge state and leptonic decay channel. The total cross section is then  $\mathcal{O}(1$  pb). Furthermore, this thesis is solely concerned with the subsequent electronic and muonic decays of the  $W$ . It should be noted that the branching ratio for  $W \rightarrow e$ ,  $W \rightarrow \mu$ , and  $W \rightarrow \tau$  are approximately 10% each, whereas the branching ratio for  $W \rightarrow q\bar{q}$  is approximately 70%. Despite the relatively lower rates for the electron and muon channels, these two have much the simplest experimental signal, hence their selection here. The subsequent decay of the tau creates difficulties in the identification of this decay channel, and the hadronic ( $q\bar{q}$ ) decay is exceptionally hard to isolate from other QCD processes. Further discussion of these decay channels, and illustration of the present insensitivity to these channels at HERA, can be found in [39].

The expected experimental signature of this process (when the  $W$  decays electronically or muonically) consists of three well defined parts. Firstly there is a hadronic jet formed from the outgoing quark which participated in the sub-process.

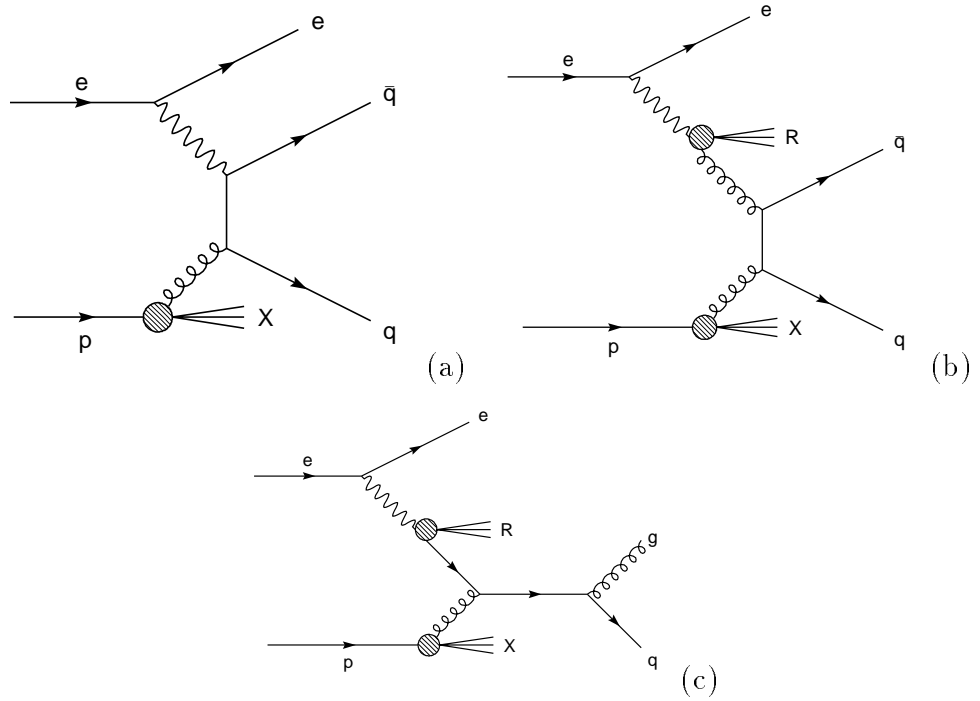


Figure 3.6: Direct (a) and resolved (b,c) photoproduction.

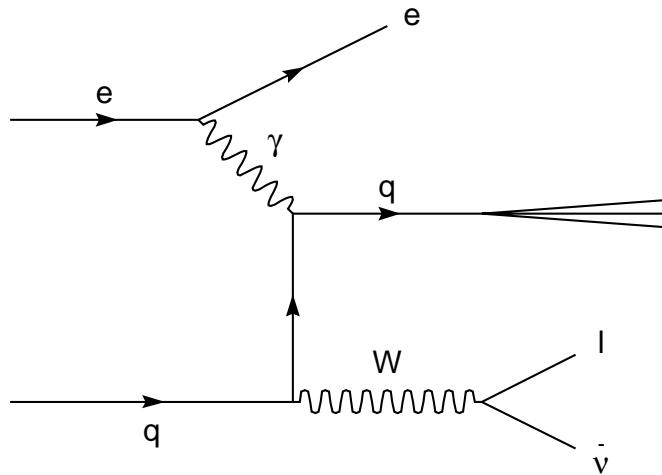


Figure 3.7: A typical leading order diagram of  $W$  production in  $ep$  collisions. Note that the  $W$  is shown decaying leptonically.

Secondly there is an electron or muon with significant transverse momentum from the decay of the  $W$ , which furthermore should be well separated from the jet in the detector, having originated from a different coupling vertex (see figure 3.7). Finally there is a total momentum imbalance in the detector, since a significant quantity of momentum is carried by the neutrino, which is undetectable.

The study of this process is of considerable theoretical interest, and is possible now that HERA has delivered sufficient luminosity for a reasonable data sample to be accumulated. Theoretical interest beyond the Standard Model is the subject of the next section. Within the framework of the Standard Model this process is of interest because it is sensitive to triple boson couplings (TBCs). This occurs when it is the  $W$  that couples to the photon, rather than a quark from the proton<sup>3</sup>. The theory of such *electroweak* interactions, like QCD, is a non-Abelian gauge theory. The self-interactions of the gauge bosons are one of the most direct consequences of the  $SU(2)_L \times U(1)_Y$  gauge symmetry, yet these couplings have only been poorly constrained by earlier lower energy experiments [40]. The search for deviations from the Standard Model predictions for these couplings is parameterised in terms of the phenomenological effective Lagrangian [41]

$$i\mathcal{L}_{eff}^{WWWV} = g_{WWV} \left[ g_1^V (W_{\mu\nu}^\dagger W^\mu - W^{\dagger\mu} W_{\mu\nu}) V^\nu + \kappa_V W_\mu^\dagger W_\nu V^{\mu\nu} + \frac{\lambda_V}{m_W^2} W_{\rho\mu}^\dagger W_\nu^\mu V^{\nu\rho} + ig_5^V \epsilon_{\mu\nu\rho\sigma} ((\partial^\rho W^{\dagger\mu}) W^\nu - W^{\dagger\mu} (\partial^\rho W^\nu)) V^\sigma \right] \quad (3.13)$$

where  $V$  is the photon,  $\gamma$ , in the case under discussion here, since  $Z$  exchange is so greatly suppressed (see equation 3.7). The overall coupling is defined as  $g_{WW\gamma} = e$  and the field strength tensors  $W_{\mu\nu} = \partial_\mu W_\nu - \partial_\nu W_\mu$  and  $V_{\mu\nu} = \partial_\mu V_\nu - \partial_\nu V_\mu$ . At tree level, electromagnetic gauge invariance fixes the couplings for on-shell photons as

$$g_1^\gamma = \kappa_\gamma = 1, \quad \lambda_\gamma = g_5^\gamma = 0. \quad (3.14)$$

---

<sup>3</sup>This diagram is explicitly illustrated in figure 4.1(e).

Hence, deviations from the Standard Model are given by

$$\Delta\kappa_\gamma = \kappa_\gamma - 1$$

and

$$\lambda_\gamma. \tag{3.15}$$

### 3.7 Beyond the Standard Model

Once into the realms of physics beyond the Standard Model,  $W$  production becomes one of the main backgrounds to a range of potential new physics processes, and hence a thorough understanding is vital.  $W$  production becomes a background either because the new physics has the same experimental signature, caused by different decay products, or because the the new physics also involves the production of a real  $W$  and its subsequent decay.

Several extensions [42–45] of the Standard Model predict the top quark to have significant flavour changing neutral current (FCNC) interactions, which could lead to a sizable single top production cross section. The subsequent decay of the top quark into a  $b$  quark and a  $W$  boson could enhance the  $W$  production cross section considerably. Such a process proceeds via diagrams like the one illustrated in figure 3.8. Notice the FCNC vertex ( $\kappa_\gamma^{FCNC}$ ) at the lower reach of the exchanged photon. The most stringent limits on the strength of such a vertex have been set by the CDF collaboration [46] as  $BR(t \rightarrow u\gamma) < 3.2\%$  at 95% confidence level, leading to  $\kappa_\gamma < 0.28$  [47]. This is sufficient to allow several single top events to be produced with the current integrated luminosity at HERA.

The possible production of leptoquarks at HERA has been the subject of both experimental [48, 49] and theoretical [50] interest in recent years. The Standard Model contains no couplings describing the direct interaction of the vertices shown



in figure 3.9.

The decay products of the leptoquark are generically labelled as a lepton and a quark; however, if the lepton is not the same as the incident electron, then lepton number has not been conserved by the process, and as such it is known as *lepton flavour violation* [51]. The latter process is considerably easier to search for, since the signature of lepton flavour conserving leptoquark production (an electron back-to-back with an hadronic jet) is swamped by the standard neutral current process ( $ep \rightarrow eX$ ). Note that such leptoquark scenarios would also allow lepton flavour violation via the  $t$ -channel exchange of a leptoquark, in addition to the  $s$ -channel process illustrated.

Another process, also beyond the Standard Model, that has been searched for at HERA is that of excited fermion production [52, 53]. Three examples are illustrated in figure 3.10, in which a fermion is temporarily excited into a higher energy state by the scattering process.

Two further processes that may contribute a  $W$ -decay-like signal are both consequences of the Minimal Supersymmetric Standard Model (MSSM). These are illustrated in figure 3.11, one  $R_P$  conserving and one  $R_P$  violating.  $R_P$ ,  $R$ -Parity, is defined as  $(-1)^{3B+L+2S}$ , where  $S$  is spin,  $B$  is baryon number and  $L$  is lepton number. Normal particles have  $R_P = 1$  and supersymmetric particles have  $R_P = -1$ , hence singly produced supersymmetric particles violate  $R_P$  conservation and those produced in pairs conserve this quantity.

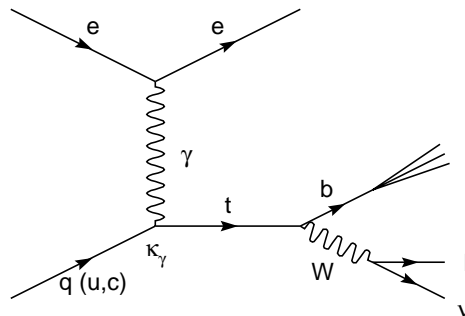


Figure 3.8: Single top production via a flavour changing neutral current (FCNC)  $\gamma_{ut}$  or  $\gamma_{ct}$  vertex.

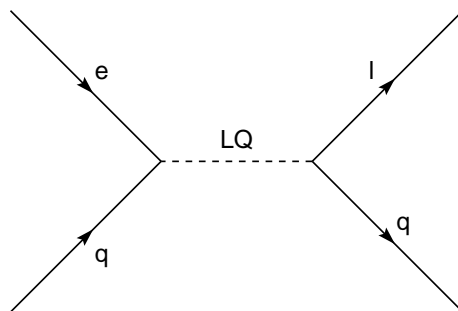


Figure 3.9: Leptoquark production via the fusion of an electron and quark, subsequently decaying to a lepton and a quark. If the decay lepton is not the same as the incident electron, the process is also known as *lepton flavour violation*.

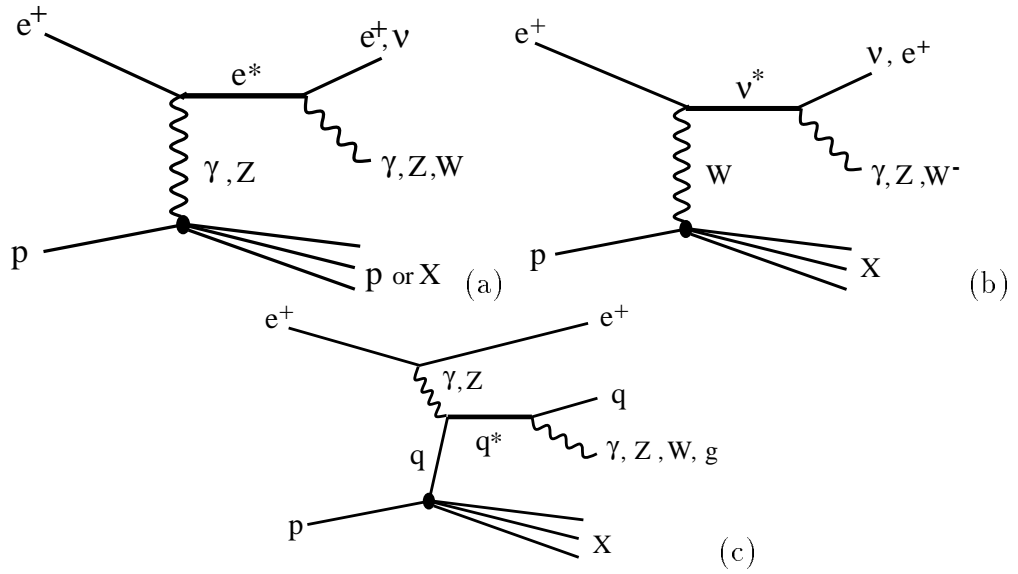


Figure 3.10: Excited fermion production. (a) positron, (b) neutrino and (c) quark.

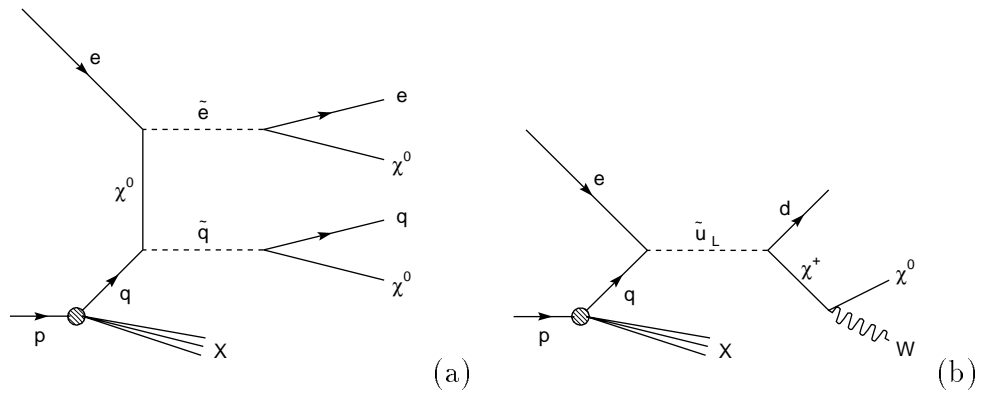


Figure 3.11: Two examples of the MSSM at HERA. (a)  $R_P$  conserving and (b)  $R_P$  violating.  $\tilde{e}$  is a selectron, the supersymmetric partner of the electron.  $\chi^0$  is a neutralino and  $\chi^+$  is a chargino.

# Chapter 4

## Monte Carlo Simulation

This chapter is concerned with the simulation of the processes that are expected to contribute to the sample selected by this analysis, both as signal and background. Firstly the principles and mechanics of Monte Carlos (MCs) are explained. Secondly the particular Monte Carlos employed by this analysis are presented and discussed.

The term “Monte Carlo” is most commonly used as a generic name to describe the prediction of a particular model, used either as a comparison with another model, or to experimental data. In the latter case, which is of most relevance here, this catch-all phrase is in fact describing a process with several stages. Firstly an event generator simulates the partons dealt with in Feynman diagrams. Secondly these partons are converted into observable particles. Finally these particles are put into a simulation of the detector, and the detector’s response to such input must be calculated. The next sections expand on these stages.

## 4.1 The Stages of Event Simulation

Monte Carlo techniques provide a method of modelling a system by assigning probabilities to all discrete possibilities, or fitting a function to continuous set of possibilities, and by repeated random number generation building up a distribution of final outcomes. An event generator calculates the amplitudes of all Feynman diagrams for a given process, using fixed order matrix elements. It implements the parton density functions (PDFs) for the proton and photon as necessary, and produces outgoing partons. More sophisticated programs also include parton showering, simulating higher order processes.

Due to colour confinement, the partons produced by the sub-process are not the final state particles observed in the detector. Leptons produced at the parton level may well be observed in the final state, but individual quarks and gluons shower and hadronise. This process can be modelled by programs such as JETSET [54]. JETSET uses the string fragmentation method, whereby all coloured partons are connected by a gluon “string”. As partons move apart, the increasing potential energy of the string creates a  $q\bar{q}$  pair and the string breaks. The same process is then iteratively applied to the daughter partons, until only lower energy, real hadrons result.

Once the final state particles have been produced, for a practical comparison with the data to be made they must be passed through a simulation of the detector. H1 uses the GEANT3 [55] software to model the detector. Monte Carlo generated events, once processed by this software, are then in a similar format to the real data. The output from each subdetector, whether real (data) or simulated (MC) is then reconstructed in an identical fashion as described in section 2.8. Not only does this allow a realistic comparison between the data and the theory to be made but also, by comparing Monte Carlo distributions before and after the detector simulation, detector effects such as resolution smearing and systematic offsets can be estimated.

## 4.2 EPVEC

### 4.2.1 Cross Section Calculation

The EPVEC event generator takes an electron and proton as the initial state particles, and produces vector bosons ( $EPVEC = ep \rightarrow VECtor$  boson). It is a set of FORTRAN routines which simulates the parton level processes illustrated in figure 4.1. The generator is based on [38]. Specifically, the generator used in this thesis is H1EPVEC [56], which implements EPVEC within the H1 computing environment using the PYTHIA [57] framework. The cross section is dominated by diagrams 4.1(a) and (b), where the  $W$  is radiated by the incoming and scattered quark. Diagrams (c) and (d) contain off-shell  $W$  propagators. Diagram (e) contains the  $WW\gamma$  vertex. Diagrams (f) and (g) are greatly suppressed due to the second heavy propagator.

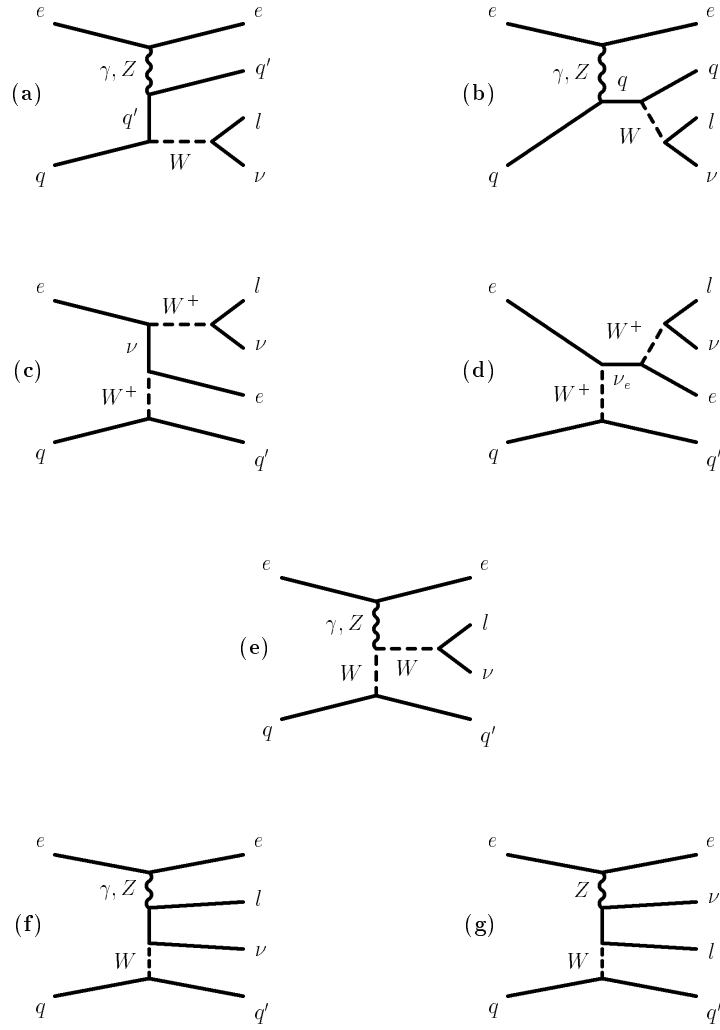


Figure 4.1: The leading order Feynman diagrams for the process  $ep \rightarrow eW^\pm X$  that are included in the event generator EPVEC.

Two particular factors are of notable interest in the calculation and implementation of these diagrams. Firstly, as stated, the process  $ep \rightarrow eWX$  is dominated by diagrams 4.1(a) and (b). In these diagrams an almost real photon and a massless quark are exchanged in a  $u$ -channel<sup>1</sup> configuration. Care must be taken in the calculation of this diagram because of the  $u$ -channel fermion pole. Close to this pole, QCD corrections become large, and the process may be considered as  $q\bar{q} \rightarrow W$  [38, 58]. Hence, the cross section is calculated as the sum of two parts, the photoproduction regime and the DIS regime, thus:

$$\sigma = \sigma(|u| > u_{cut}) + \int_{-u_{cut}}^{u_{cut}} d|u| \frac{d\sigma}{d|u|} \quad (4.1)$$

where,

$$u = (p_q - q_W)^2 \quad (4.2)$$

and  $p_q$  and  $q_W$  are the four momenta of the incoming quark and the final state  $W$  respectively. The cross section for values of  $|u|$  above  $u_{cut}$  (the DIS regime) is calculated as specified in [58], using helicity amplitudes. For  $|u|$  below  $u_{cut}$  a “resolved photon” approach is adopted, using the Weizsäcker-Williams [59, 60] approximation for the photon spectrum. The photon structure function used is the LAC [61] parameterisation taken from PDFLIB [62].

Previous work [63] has shown that the  $W$  production cross section has a small dependency on the choice of  $u_{cut}$  ( $\simeq 5\%$ ), a similar dependency on the choice of proton structure function ( $\simeq 5\%$ ), and a slightly larger dependency on the choice of photon structure function ( $\simeq 10\%$ ). The cross section is also sensitive to the choice of  $Q^2$  scale for the partons in both the photon and proton. The error originating from this choice is estimated [64] to be around 10%.

---

<sup>1</sup>As with all choices of Mandelstam variable configurations, the definition of this diagram as  $u$ -channel is arbitrary.



Final state parton showers are simulated using the PYTHIA framework [65]. An error of 30% is quoted for this cross section calculation. This is due mainly to uncertainties in the photon parton density functions and the scale at which the calculation is performed.

### 4.2.2 Event Characteristics

As outlined in section 3.6, real  $W$  production at HERA has a spectacular signature, characterised by an isolated high  $p_T$  lepton, a hadronic jet and missing transverse momentum. One of the most striking events of this kind, beautifully illustrating this topology, is shown in figure 4.2.

## 4.3 Background Processes

- Charged Current (CC) processes :  $ep \rightarrow \nu X$

A CC DIS event (see figure 3.1) can mimic the topology of leptonic  $W$  decay events if a particle in the hadronic final state is misinterpreted as a candidate lepton from  $W$  decay. The generator DJANGO [66] was used to calculate this contribution. Studies of CC events where a candidate electron, passing loose selection requirements, is found show that events of this kind are described by the expectation within a systematic error of 30% (see section 6.4).

- Neutral Current (NC) processes :  $ep \rightarrow eX$

The scattered electron in a NC DIS event (see figure 3.1) can be misinterpreted as the lepton from  $W$  decay, but the missing transverse momentum can only be produced by fluctuations in the shower or detector response to the final state particles, or by limited geometrical acceptance. The generator DJANGO [66] was used to calculate this contribution. The generator PYTHIA [57] was used

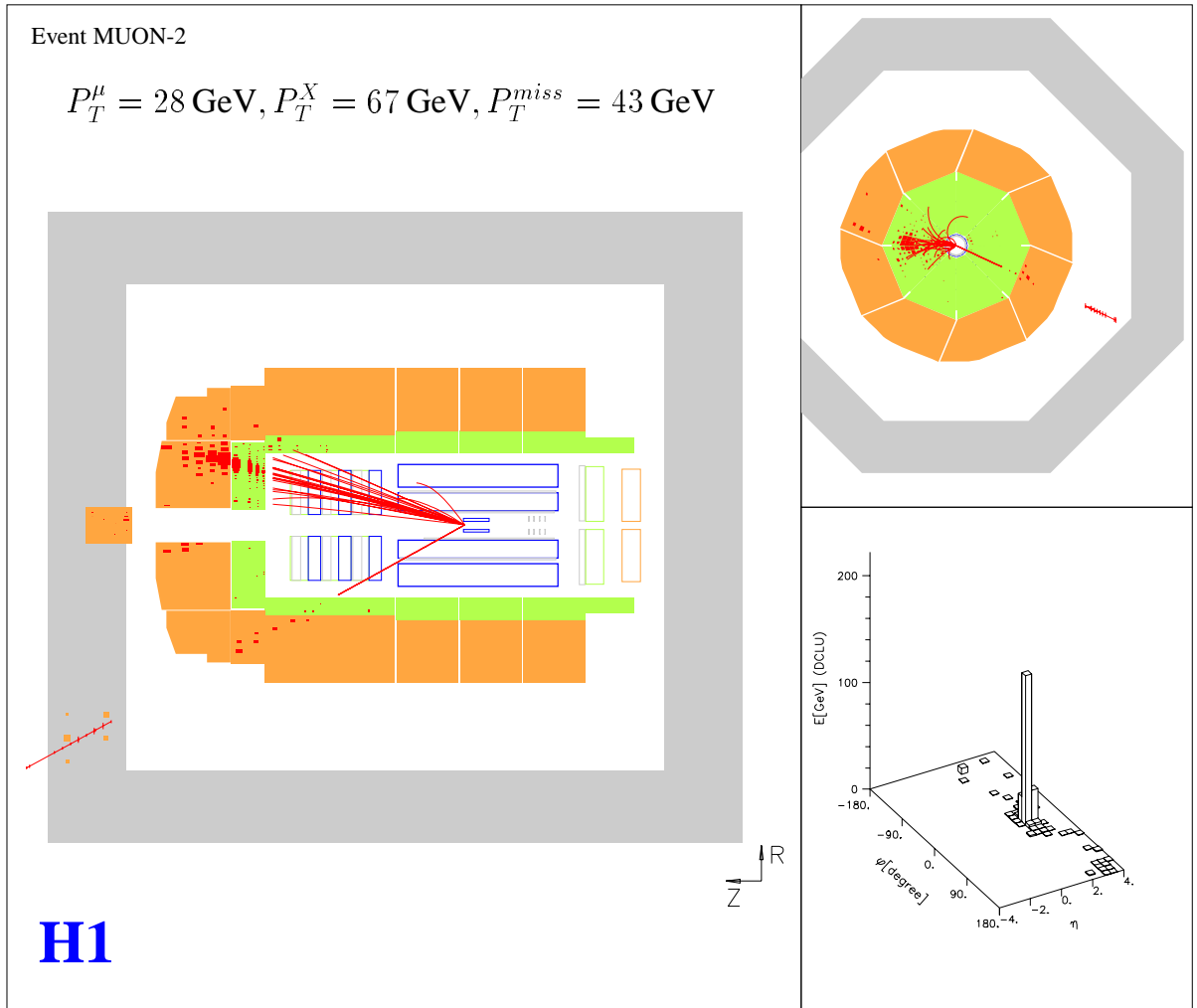


Figure 4.2: A spectacular candidate  $W$  event, with the  $W$  decaying leptonically via the muon channel, observed at H1 in 1997, beautifully illustrating the classic topology of this class of events.

to calculate the QCD photoproduction process  $\gamma p \rightarrow X$ . Production of heavy flavours is included in DJANGO and PYTHIA [67]. Studies of NC events with reconstructed missing transverse momentum show that events of this kind are described by the expectation within a systematic error of 30% (see section 6.3).

- Lepton pair production in two photon ( $\gamma\gamma$ ) interactions

Inelastic lepton pair production can mimic the topology of  $W$  events if one lepton escapes detection, and measurement error causes apparent missing momentum. The generator LPAIR [68] was used to calculate this contribution.

Studies of events with two identified leptons show that events of this kind are described by the expectation within a systematic error of 75% (see section 6.5).

# Chapter 5

## Event Selection : Part I

Due to the low cross section of real  $W$  production at HERA ( $\mathcal{O}(1 \text{ pb})$ ) the selection criteria for such events must be extremely carefully defined. It is desirable to reject as great a proportion of the background processes as possible, but in doing so it is also vital to maintain a high acceptance of the rare signal.

### 5.1 The “Isolated Lepton” Analysis

The selection criteria presented in this analysis, and in fact the entire analysis, are historically based on the published observation [37] of several events with a high transverse momentum ( $p_T$ ) lepton and overall missing transverse momentum at H1. These events were recorded by H1 in a data sample of  $36.5 \text{ pb}^{-1}$  of  $e^+p$  collision data accumulated between 1994 and 1997. The topology of the events presented was so striking that a data set of only six events warranted publication. Indeed, the first of the events to be observed by H1 was sufficiently notable to warrant its own publication [69], and to generate considerable theoretical interest [70]. Both of the H1 publications are firmly styled as an *observation*, and neither the selection criteria employed nor the conclusions drawn are motivated by a particular physics

process. Real  $W$  production is nevertheless highlighted as the dominant Standard Model source of events with this topology.

The six published events are selected by the following requirements:

- A calorimetric missing transverse momentum,  $P_T^{calo}$ , greater than 25 GeV.
- A well measured central track with a polar angle greater than  $10^\circ$  and a transverse momentum greater than 10 GeV (a *high*  $P_T$  track).

Further to these selection requirements some standard [71] cuts are made to reject non- $ep$  events due to cosmic muons, halo muons or beam-gas interactions. Further anti-NC cuts are made, rejecting events in which the scattered positron<sup>1</sup> is balanced in azimuth by the hadronic system within  $\Delta\phi = 5^\circ$ , and events where the longitudinal momentum balance results in  $\delta > 45$  GeV. Definitions and discussions of these quantities are presented in section 5.3.

These criteria select 124 events. The high- $P_T$  track is further required to be isolated from other activity in the detector. This isolation is quantified by:

- its distance  $D_{jet}$  to the nearest hadronic jet in the pseudorapidity<sup>2</sup>-azimuth plane  $\eta - \phi$ .
- its distance  $D_{track}$  to the nearest track in the pseudorapidity-azimuth plane  $\eta - \phi$ . (Definitions and discussions of these quantities are presented in section 5.3.)

This procedure selects the six events. One event contains an isolated electron, and the other five contain an isolated muon. The electron event and two of the muon events have kinematics compatible with Standard Model  $W$  production. However,

---

<sup>1</sup>The publication presents only  $e^+p$  collision data.

<sup>2</sup>Pseudorapidity,  $\eta = \ln[\tan(\frac{\theta}{2})]$

the three remaining muon events are atypical. This is best illustrated with reference to the quantities  $P_T^X$ , the transverse momentum of the hadronic system, and  $M_T^{l\nu}$ , the transverse mass of the lepton-neutrino system. The correlation between these quantities is plotted in figure 5.1. The Monte Carlo events plotted (points) have a luminosity 500 times greater than that of the data. The three events labelled  $\mu 1$ ,  $\mu 2$  and  $\mu 4$  can thus be seen to be remarkably unusual.

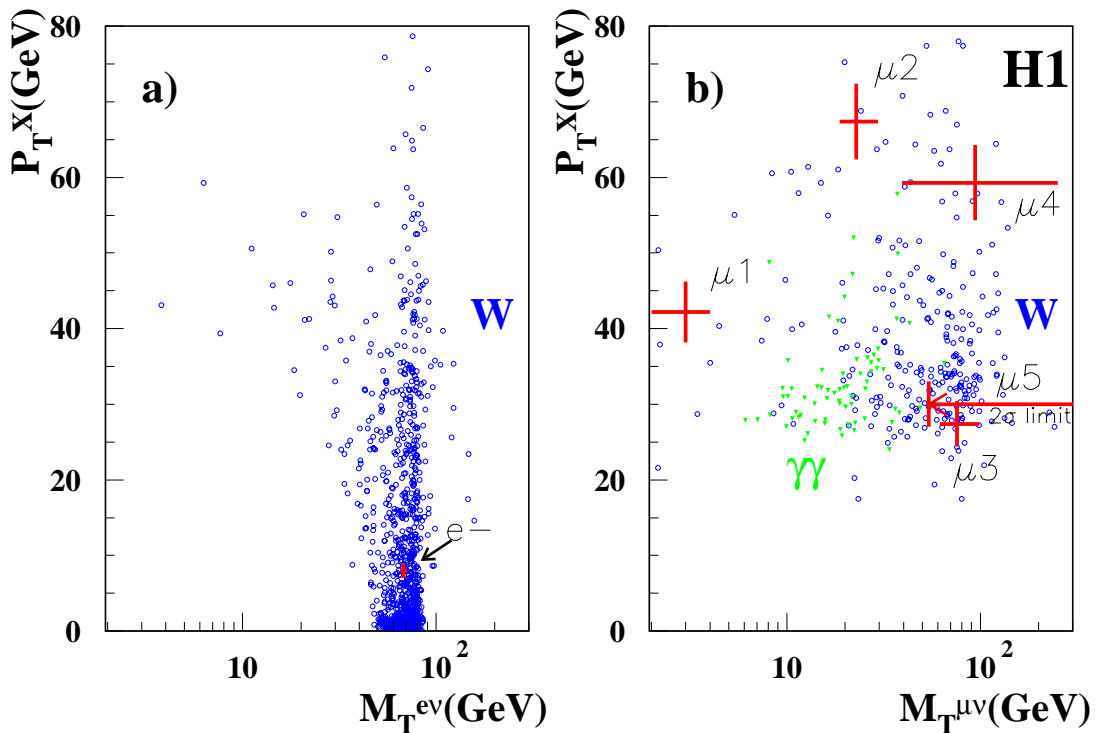


Figure 5.1: Scatter plots showing the correlation between  $P_T^X$  and  $M_T^{l\nu}$  (electron (left) and muon (right)). Blue dots are simulations of Standard Model  $W$  production generated by the EPVEC [56] program. Green dots are simulations of Standard Model lepton pair events (labelled  $\gamma\gamma$ ) generated by the LPAIR program [68]. All simulations have a luminosity 500 times that of the data (crosses) shown. Taken from from [37].

The final numbers of events compared with Standard Model processes are shown

in table 5.1.

	Electron Channel	Muon Channel
Data	0 $e^+$ , 1 $e^-$	5
$W$ production	$1.65 \pm 0.47$	$0.53 \pm 0.11$
CC - DIS	$0.02 \pm 0.01$	$0.01 \pm 0.01$
NC - DIS	$0.51 \pm 0.10 e^+$ , $0.02 \pm 0.01 e^-$	$0.09 \pm 0.06$
Photoproduction	$< 0.02$	$< 0.02$
Heavy Quarks	$< 0.04$	$< 0.04$
Photon-Photon	$0.09 \pm 0.03 e^+$ , $0.04 \pm 0.01 e^-$	$0.14^{+0.14}_{-0.07}$

Table 5.1: Observed and predicted event rates. The limits given correspond to 95% confidence level. Unless stated otherwise the quoted numbers refer to the summed production of both lepton charged states. Taken from [37].

## 5.2 The Presented Data

Since the publication of the “isolated lepton” paper [37], H1 has more than doubled the integrated luminosity of  $e^+p$  collision data, recording a further  $45.1 pb^{-1}$  of  $e^+p$  data in 1999 and 2000. A smaller sample ( $13.6 pb^{-1}$ ) of  $e^-p$  data was also recorded in 1998/9. The analysis presented in this thesis covers the full  $81.6 pb^{-1}$  of  $e^+p$  data, and the smaller  $e^-p$  sample.

## 5.3 The Selection Variables

The production of real  $W$  bosons has already been identified as the dominant Standard Model source of the events discussed in section 5.1. However the selection criteria of the discussed publication [37] were not explicitly developed to select this

process. In the development of this analysis to do just that, it has been necessary to move into a considerably more *multi-variate* framework, drawing on the discriminatory power of a range of variables. The variables employed are as follows:

- $P_T^{calo}$ , the missing transverse momentum measured in the calorimeters. This is the vector sum of all calorimeter deposits (electronic and hadronic).
- $P_T^{miss}$ , the total missing momentum, reconstructed from calorimeters and track detectors. This is the vector sum of all calorimeter deposits (electronic and hadronic) and of all instrumented iron hits.
- $P_T^l$ , the transverse momentum of the identified lepton (electron or muon).
- $P_T^X$ , the transverse momentum of the hadronic system, defined as all reconstructed particles apart from identified isolated leptons.
- $\theta_l$ , the polar angle of the muon or electron, where  $\theta_l = 0^\circ$  is defined as the direction of the incoming proton beam.
- $\delta_{miss} = 2E_e - \sum E_i(1 - \cos \theta_i)$ , where  $E_i$  and  $\theta_i$  denote the energy and polar angle of each detected particle in the event and  $E_e$  is the electron beam energy.  $\sum E_i(1 - \cos \theta_i)$  is sometimes written  $(E - p_z)$ . For an event where only longitudinal momentum in the proton direction is undetected  $\delta_{miss} = 0$ .
- $\Delta\phi_{l-X}$ , the acoplanarity, the difference in azimuthal angle between the lepton and the vector that balances the vector of the hadronic final state  $X$ . NC events typically have low values of  $\Delta\phi_{l-X}$  – the lepton and hadronic final state are “back-to-back”.
- $\frac{V_{ap}}{V_p}$ , a measure of the azimuthal balance of the event. It is defined as the ratio of the anti-parallel to parallel components of the measured calorimetric transverse momentum, with respect to the direction of  $P_T^X$  [19]. Hence,



$$V_p = \sum_i \frac{\vec{P}_T^X \cdot \vec{P}_{T,i}}{P_T^X} \quad \text{for} \quad \vec{P}_T^X \cdot \vec{P}_{T,i} > 0 \quad (5.1)$$

$$V_{ap} = - \sum_i \frac{\vec{P}_T^X \cdot \vec{P}_{T,i}}{P_T^X} \quad \text{for} \quad \vec{P}_T^X \cdot \vec{P}_{T,i} < 0 \quad (5.2)$$

- $\zeta_l^2 = 4E^l E_e \cos^2 \theta_l/2$ , where  $E^l$  is the energy of the final state lepton. For NC events, where the scattered electron is misinterpreted as a decay lepton from the  $W$ ,  $\zeta_l^2$  is equal to the four momentum transfer squared  $Q^2$ . Since the NC cross section falls steeply with  $Q^2$ , these events generally have small values of  $\zeta_l^2$ . Conversely, leptons from  $W$  decay generally have high values of  $\zeta_l^2$ .
- $E_{cone}$ , the energy contained within a cone of radius 1 in  $\eta$ - $\phi$  space around the electron, that is not associated to the electron. Defining an upper limit on the ratio of this value to the energy of the electron allows a measure of control on how “clean” an electron candidate is.
- $D_{jet}$ , the distance between the high  $P_T$  lepton and the closest hadronic jet in the pseudorapidity-azimuth plane ( $\eta - \phi$ ), defined by
$$D_{jet} = \sqrt{(\Delta\eta_{track-jet})^2 + (\Delta\phi_{track-jet})^2}$$
(for this purpose jets are reconstructed using an inclusive  $k_T$  algorithm [72,73] with  $R < 1$  and  $E_T^{min} = 5$  GeV). If there is no jet in the event,  $D_{jet}$  is defined with respect to the polar and azimuthal angle of the hadronic final state  $X$ .
- $D_{track}$ , the distance between the high  $P_T$  lepton and the closest track in  $\eta - \phi$ , defined in an analogous way to  $D_{jet}$ , where all tracks with a polar angle greater than  $5^\circ$  are considered.

## 5.4 Lepton Identification

### 5.4.1 Electron Candidates

An electron candidate is identified by the presence of a compact and isolated cluster of energy in the electromagnetic part of the LAr calorimeter. Furthermore, this cluster of energy must be associated with a track<sup>3</sup> having a distance of closest approach to the cluster of less than 12 cm. When the track produces hits in the 3 central chambers (CJC, CIZ and COZ – see sections 2.3.1 and 2.3.2) it determines the polar angle of the electron candidate. When the track is less well constrained, this angle is determined using the position of the electromagnetic energy cluster and the reconstructed vertex. The azimuthal angle is always determined from track information. The energy of the electron candidate is determined from the calorimeter cluster.

The calibration of the electron energy is performed as developed in [19]. Fiducial cuts exclude the candidate electron from regions of the detector known to contain significant amount of inactive material;  $\phi$ - and  $z$ -cracks between calorimeter modules. NC DIS events, kinematically reconstructed via two different methods (DA [76] and  $\omega$  [77]), are used to calibrate the electron energy scale. Elastic QED Compton and exclusive  $\gamma\gamma \rightarrow e^+e^-$  events are also used since NC DIS statistics are limited in the forward region [19]. The fractional energy shift for different calibration methods is shown in figure 5.2.

### 5.4.2 Muon Candidates

Due to the penetrative nature of muons, their presence in an event may be identified from several different regions of the detector. Indeed a single high energy muon in

---

<sup>3</sup>The track definition comes from the H1 software package H1PHAN [74], which handles tracks and clusters reconstructed by H1REC [75].

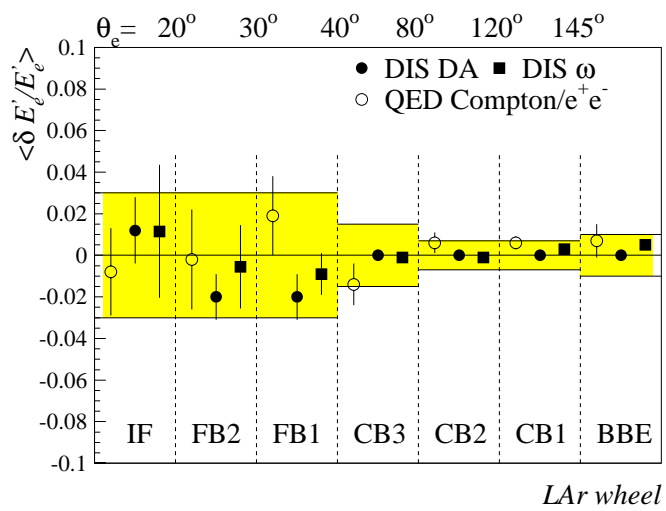


Figure 5.2: Comparison of the electromagnetic energy scale as determined by different calibration methods as a function of polar angle (and calorimeter module). The shaded error band shows the systematic uncertainty (0.7% to 3%) on the energy scale quoted in this thesis. Taken from [19].

the forward direction may be consecutively detected by the forward tracker, the LAr calorimeter, the instrumented iron and the forward muon system. Nevertheless the identification of muon candidates requires careful definition, due to the need for clean, well identified and well isolated muon candidates.

Muon candidates are identified by two sets of criteria. Less stringent requirements are imposed for muon candidates selected for the study sample (see section 5.7.2). A tighter definition is employed for those candidates contributing to the final event sample.

Candidates are required to have tracks in the instrumented iron, the forward muon system, the inner tracking system (forward or central) or any combination of these. Those candidates formed from inner tracks alone must be associated with an energy deposition typical of a minimum ionising particle in the LAr calorimeter. The energy of a muon candidate is measured from the curvature of the track in the inner tracking system.

Candidate muon tracks in the inner tracking system are required to have  $P_T > 1$  GeV. Setting this cut significantly lower than the final muon selection cut (10 GeV) allows second muons in  $\gamma\gamma \rightarrow \mu^+\mu^-$  events to be identified. Were the muon selection cut to be set at 10 GeV throughout, additional muons with lower energy would be missed, and  $\gamma\gamma \rightarrow \mu^+\mu^-$  events misidentified as  $W \rightarrow \mu\nu$  candidates.

Muon candidates formed solely from a track in the instrumented iron are rejected for  $\theta < 25^\circ$ , because of scattering in the beam pipe causing hits in this region of the instrumented iron. Good muon candidates in this region are identified by the forward muon system.

For events entering the final sample the candidate muon must satisfy stricter requirements. The muon in this sample may be identified by a forward muon track. Otherwise, the muon must have an inner track link and either a track segment or a characteristic energy deposit in the instrumented iron.

These criteria are summarised in table 5.2.

	Study Sample	Final Selection
Track definition	Forward Muon track or Iron track or Inner track or any combination	Forward Muon track or Inner track + Iron track or Inner track + Iron energy deposit
Transverse Momentum	5 GeV	10 GeV
	Second muons need only have 1 GeV	
Polar Angle	$25^\circ < \theta_\mu < 145^\circ$ or Forward Muon	

Table 5.2: A summary of muon candidate definitions.

## 5.5 Hadronic Reconstruction

The hadronic final state is predominantly measured by the LAr calorimeter, however information from the inner trackers is also used, since the momentum measurement of low momentum tracks is performed more accurately by the trackers. An algorithm (FSCOMB) assigns calorimeter energy in a cylinder of radius 25 (50) cm in the electromagnetic (hadronic) section of the calorimeter to a track leading to its centre. This procedure is described in more detail in [18] and [19].

The calibration of hadronic energy is made using a large NC event sample. This method is inherited directly from [19]. The intrinsic balance of a NC event means that the transverse momentum of the scattered electron should exactly balance the transverse momentum of the hadronic final state. The ratio of these two quantities for the large NC calibration sample is shown in figure 5.3. This ratio is used to correct the hadronic energy measurement as a function of the hadronic polar angle.

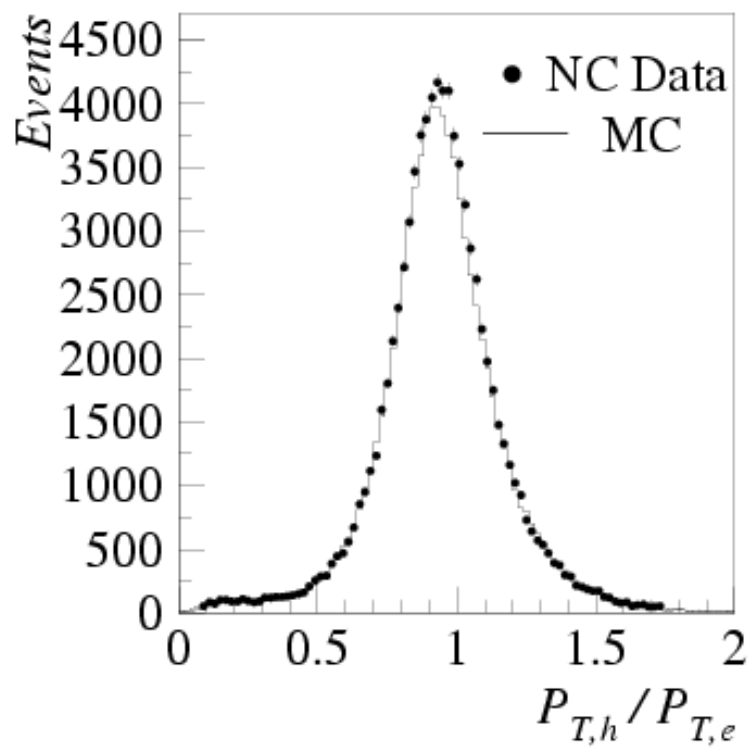


Figure 5.3: Hadronic calibration. The ratio of the transverse momentum of the hadronic final state to the transverse momentum of the scattered positron for a large sample of NC events. Taken from [19].

## 5.6 Rejection of non- $ep$ Processes

As previously stated, the rate of events originating from an  $ep$  interaction is considerably lower than the rate of events from non- $ep$  processes. The time-of-flight systems (see section 2.6) eliminate the vast majority ( $\approx 99\%$  [78]) of this background, but a small proportion is mistaken for desirable physics by the detector and recorded with the rest of the data. The three main types of non- $ep$  process recorded by H1 are cosmic muons (figure 5.4), beam halo muons (figure 5.5) and beam-gas events (figure 5.6). It is even possible for all three to occur at once (figure 5.7).

A set of background finders [79, 80] are used to identify these events, and reject them from the analysis. The background finders employ algorithms that identify characteristic patterns of energy deposition in the detector (commonly in the LAr calorimeter). For example, the algorithm HALAR ([80]) divides the LAr calorimeter into strips running parallel to the beam pipe, and identifies beam-halo muon events by their characteristic energy deposition along such a strip.

All events selected by the loose selection criteria are visually examined. A few events are rejected at this stage.

## 5.7 The Cuts

In both electron and muon channels a set of selection criteria (the “loose” cuts) are defined which select a small subset of the full data sample, the study sample. Defining these “loose” selections, which typically contain between 5 (muon) and 15 (electron) times the number of events as the final sample, allows studies to be made of the background processes that contribute to each channel, and to verify that the distributions of the data samples are well described in both shape and normalisation by the Monte Carlo simulation. A further set of cuts defines the final sample (the

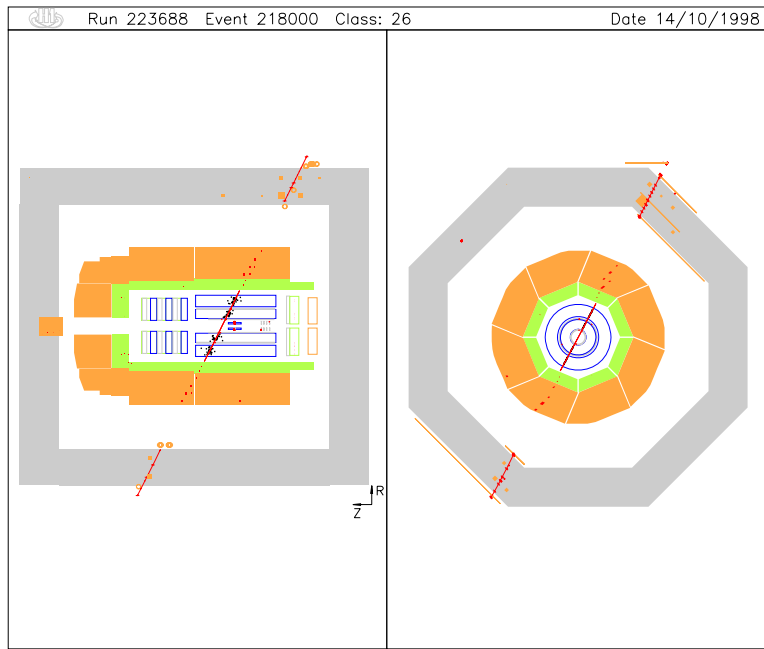


Figure 5.4: A cosmic muon event.

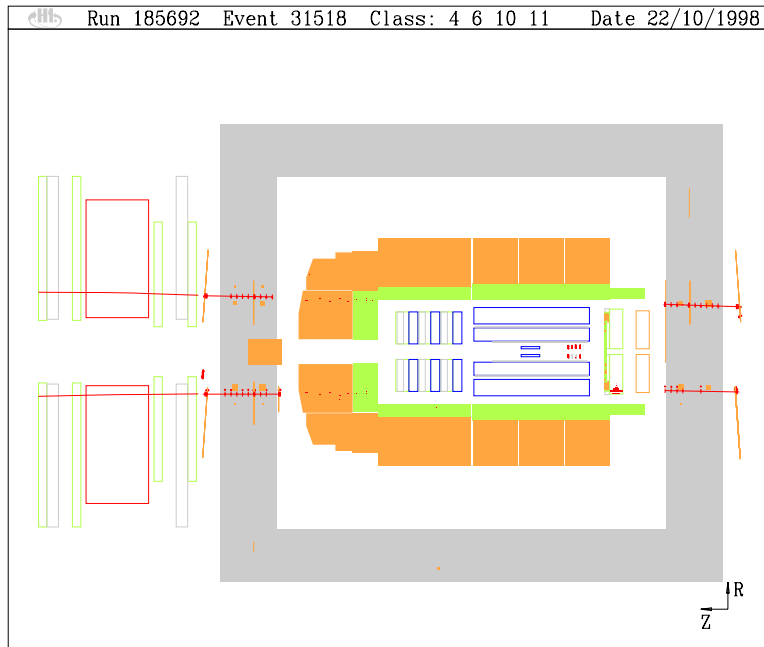


Figure 5.5: A beam halo muon event.



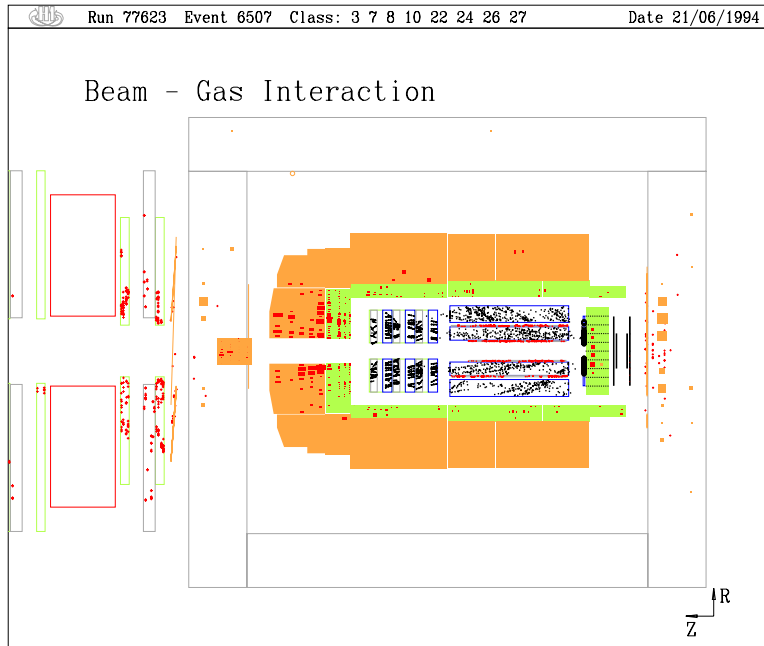


Figure 5.6: A beam-gas event.

Run 55920 Event 19103 Class: 8 9 13 Date 2/05/1994

Three events in one

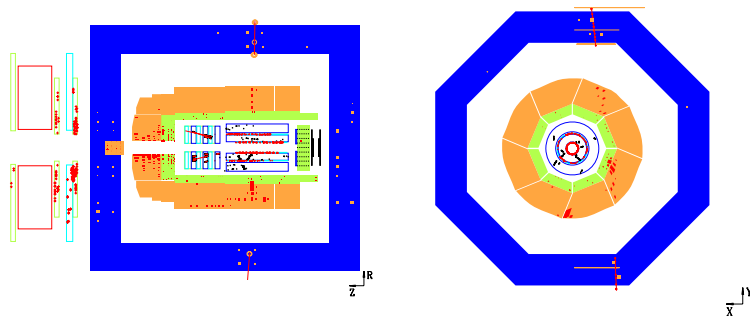


Figure 5.7: The coincidence of a cosmic muon, a beam halo muon and a beam-gas event.

“harsh” cuts). The loose cuts are defined and discussed in sections 5.7.1 and 5.7.2, and the harsh cuts are defined in sections 7.1.1 and 7.2.1. Discussion of the choice of final selection criteria takes place in sections 6.1 and 6.2.

### 5.7.1 Selecting the Electron Channel : $ep \rightarrow eWX \rightarrow ee\nu X$

The dominant background source in the electron decay channel are Neutral Current (NC) events which have significant  $P_T^{calo}$ . This imbalance of transverse momentum in the calorimeter is purely a feature of the measurement since NC events have no intrinsic momentum imbalance.

The distribution of NC events with respect to  $Q^2$  is one of the most powerful tools for tackling this background. Figure 5.8 shows the  $Q^2$  distribution of a large sample of NC events, with and without a  $P_T^{calo}$  requirement. Noting the logarithmic scale of the ordinate, the distributions of both samples are seen to fall extremely rapidly with increasing  $Q^2$ .

For this purpose  $Q^2$  is calculated using the *electron method*, where it is defined as  $Q^2 = 4E^l E_e \cos^2 \theta_l / 2$ , where  $E^l$  is the energy of the scattered electron,  $E_e$  is the energy of the beam electron and  $\theta_l$  is the polar angle of the scattered electron. However, if this method is applied to events involving the decay of a  $W$  boson which has decayed  $W \rightarrow e\nu$  then the electron candidate detected is more likely to be the decay electron from the  $W$  rather than the beam electron. Hence, the quantity  $\zeta^2$  is defined, exactly as for  $Q^2$ , but where it is understood that the quantity being kinematically reconstructed is  $Q^2$  for NC events, and is (most likely) a different quantity for  $W$  events. Nevertheless, this quantity is an useful discriminant for the rejection of NC events, since  $\zeta^2(Q^2)$  falls much more rapidly for NC events than for  $W$  events.

A second powerful discriminant in the rejection of the NC background is the *acoplanarity* of an event. This is defined as the azimuthal angle between the lepton

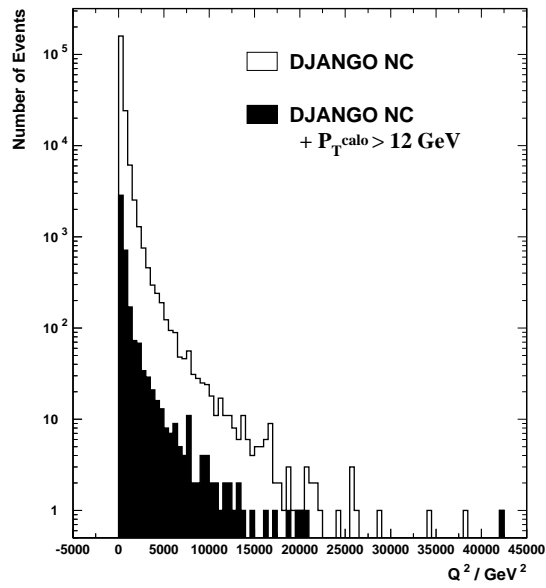


Figure 5.8: The  $Q^2$  distribution of a sample of  $\sim 200,000$  DJANGO neutral current events (open histogram), and of the same sample with the additional requirement that  $P_T^{calo} > 12$  GeV (shaded histogram). Noting the logarithmic scale, both distributions are seen to fall very rapidly with increasing  $Q^2$ .

and the direction that balances the hadronic final state. This is illustrated in figure 5.9. For a NC event there is no neutrino and hence  $\Delta\phi_{e-X} = 0^\circ$ . Deviations from this, as for  $P_T^{calo}$ , are a feature of the resolution of the detector and of fluctuations in the the measurement process. As can be seen in figure 5.10, the distribution of  $\Delta\phi_{e-X}$  is strongly peaked at  $0^\circ$  for NC events. (This NC sample has the same  $P_T^{calo}$  cut applied as in the shaded histogram of figure 5.8.)

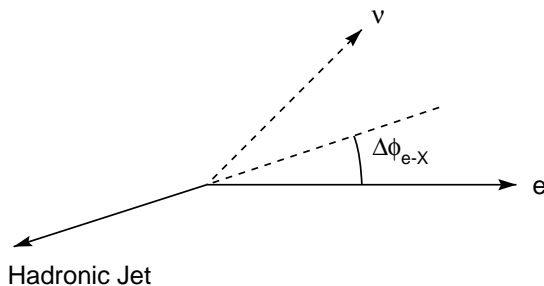


Figure 5.9: Diagram showing the definition of the acoplanarity. The vectors shown are in the azimuthal plane.

A third useful discriminant for separating NC and  $W$  events is the quantity  $\frac{V_{ap}}{V_p}$ . This was developed as part of the H1 NC/CC high  $Q^2$  analyses [19], and is a measure of the isotropic nature of the azimuthal projection of an event. It is defined as the ratio of the anti-parallel<sup>4</sup> to parallel components of the measured calorimetric transverse momentum, with respect to the direction of  $P_T^X$  [19]. Events with one or more particles, that do not deposit much energy in the calorimeter ( $\mu, \nu$ ), generally have low values of  $V_{ap}/V_p$ . Thus the distribution of  $\frac{V_{ap}}{V_p}$  for  $W$  events is strongly peaked at 0 – see figure 5.11.

The study sample for the electron decay channel is defined by the following selection requirements :

---

<sup>4</sup>It should be noted that careful distinction should be made between the terms *anti-parallel* and *perpendicular* to avoid considerable confusion [81].

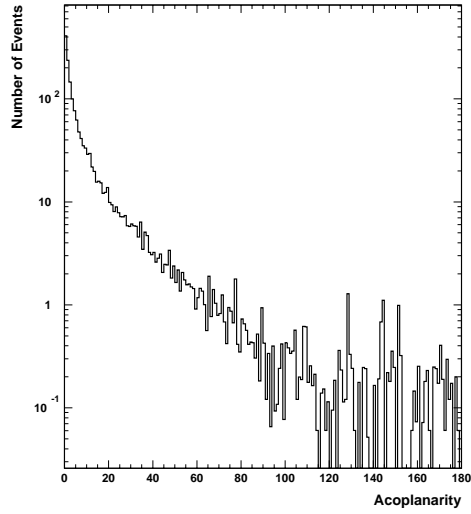


Figure 5.10: The acoplanarity,  $\Delta\phi_{e-X}$ , distribution of a sample of  $\sim 27,000$  DJANGO neutral current events, with  $P_T^{calo} > 12$  GeV. Noting the logarithmic scale, the distribution is very strongly peaked and falls very rapidly with increasing acoplanarity.

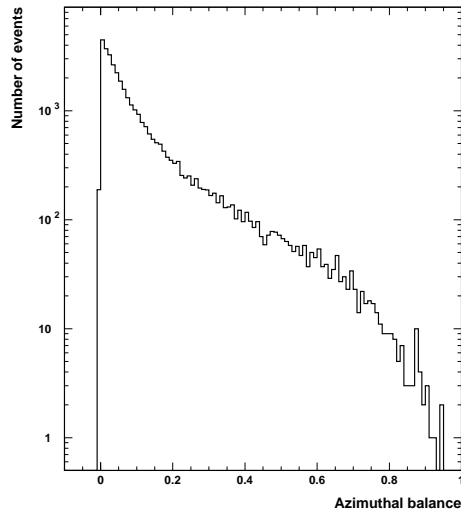


Figure 5.11: The azimuthal balance,  $\frac{V_{ap}}{V_p}$ , of a sample of  $\sim 35,000$  EPVEC  $W$  events. Noting the logarithmic scale, the distribution is very strongly peaked at a value of 0.

- $\zeta^2 > 500 \text{ GeV}^2$
- $\frac{V_{ap}}{V_p} < 0.5$  ( $< 0.15$  for  $P_T^e < 25 \text{ GeV}$ )
- $P_T^e > 10 \text{ GeV}$
- $5^\circ < \theta_e < 145^\circ$
- $D_{jet} > 1.0$
- $P_T^{calo} > 12 \text{ GeV}$
- $P_T^{miss} > 12 \text{ GeV}$

### The positron-proton data

This procedure selects 284 data events for the  $e^+p$  data taken in 1994-1997 and 1999-2000. This compares well to  $336 \pm 96$  Monte Carlo events selected by the same criteria. The distributions of these real and simulated events in the variables defining the final samples are shown in figures 5.12 to 5.15. In these and all following plots (unless otherwise stated), the data points are illustrated with Gaussian error bars. These are intended as a guide to the statistical precision of the data, not for quantitative analysis.

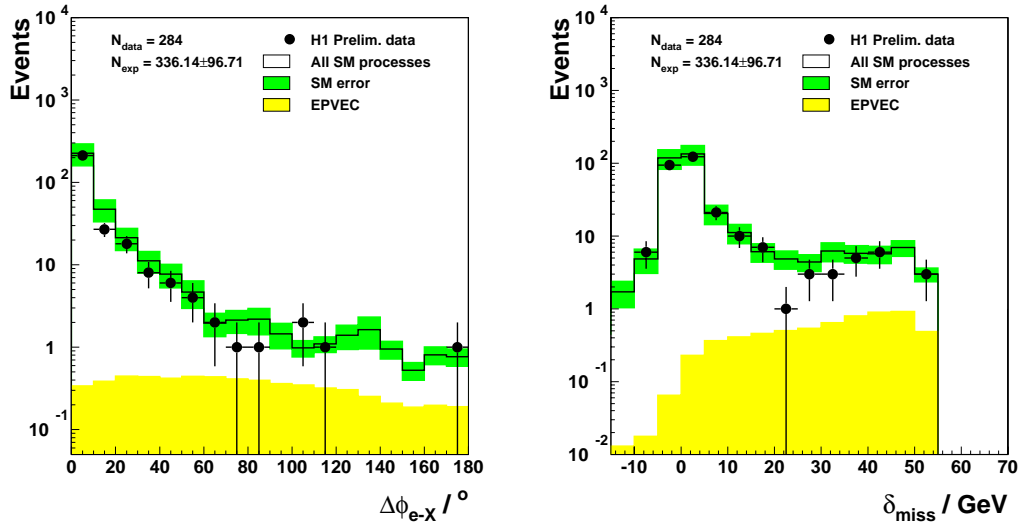


Figure 5.12: The acoplanarity (left) and the missing ( $E - p_z$ ) (right) of the electron study sample in the 94-00  $e^+p$  data.

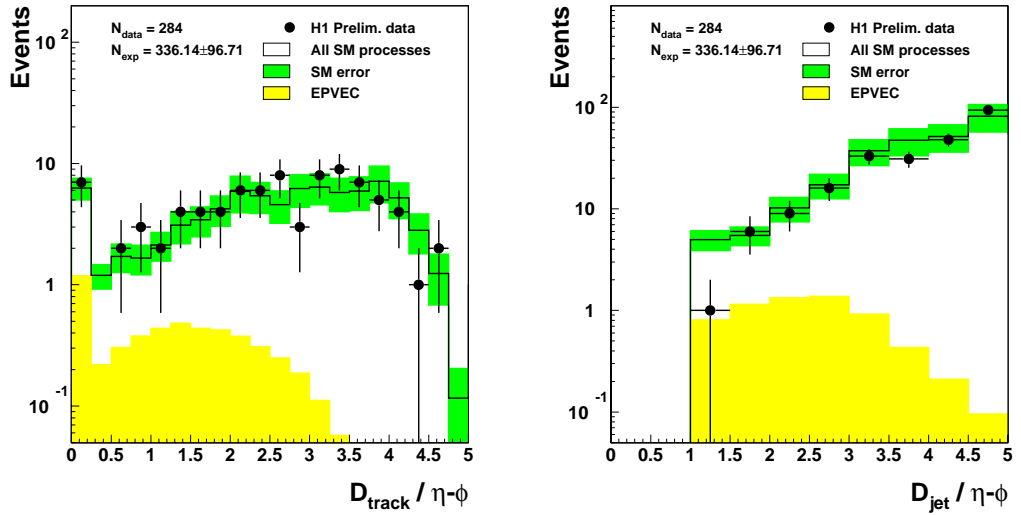


Figure 5.13: The distances  $D_{track}$  (left) and  $D_{jet}$  (right) of the electron study sample in the 94-00  $e^+p$  data.

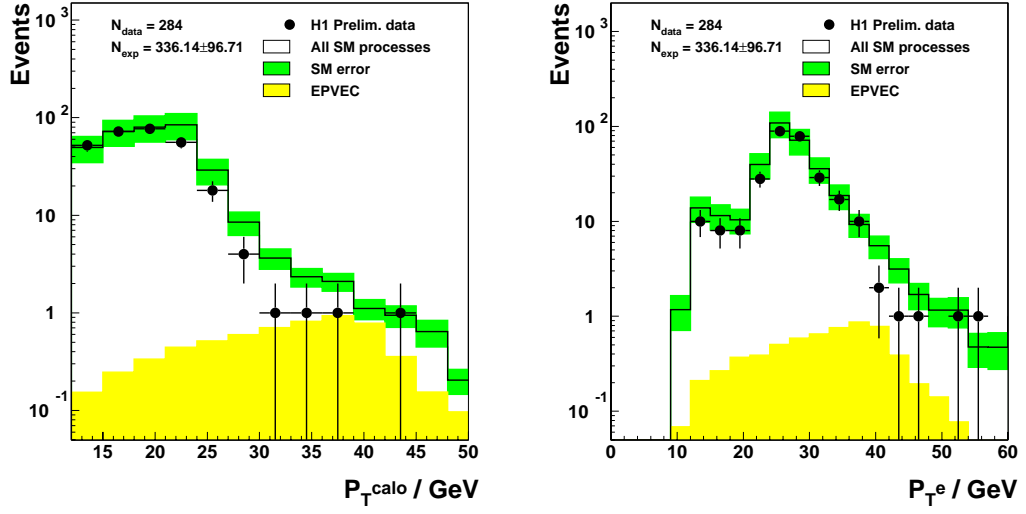


Figure 5.14: The calorimetric missing transverse momentum (left) and the transverse momentum of the electron (right) of the electron study sample in the 94-00  $e^+p$  data.

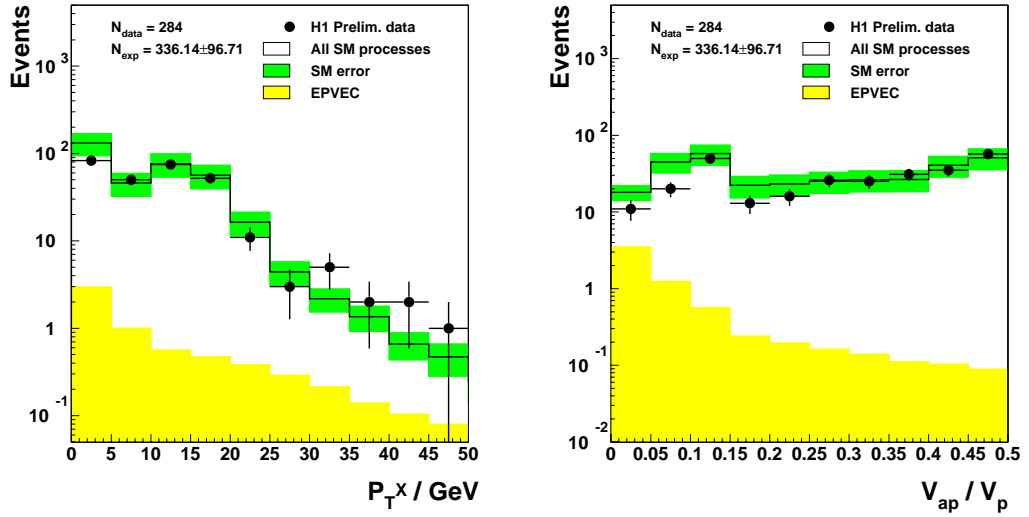


Figure 5.15: The transverse momentum of the hadronic final state,  $P_T^X$  (left), and the azimuthal balance (right) of the electron study sample in the 94-00  $e^+p$  data.



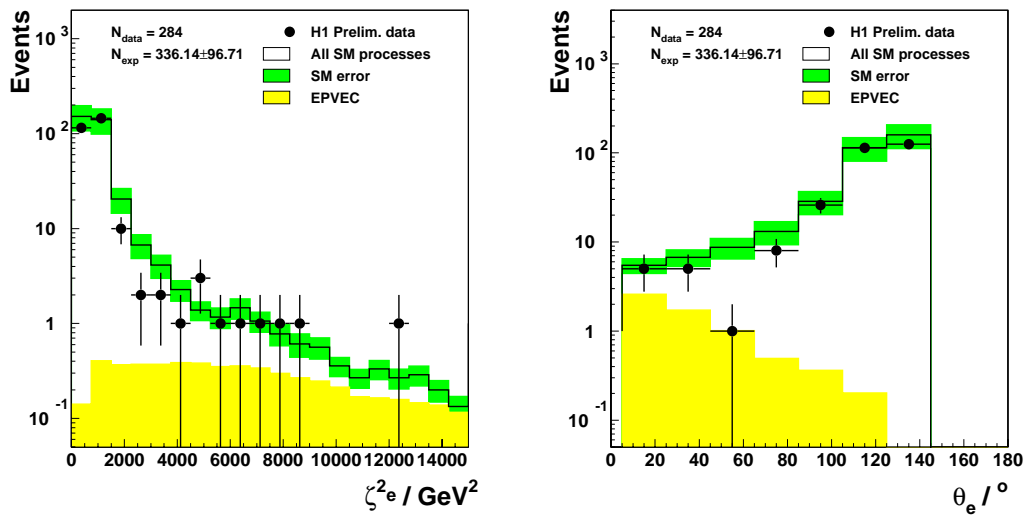


Figure 5.16: The  $\zeta^2(Q^2)$  (left) and  $\theta$  (right) distribution of the electron study sample in the 94-00  $e^+p$  data.

## The electron-proton data

This procedure selects 49 data events for the  $e^-p$  data taken in 1998-1999. This compares to  $78.5 \pm 22.5$  Monte Carlo events selected by the same criteria. The distributions of these real and simulated events in the variables defining the final samples are shown in figures 5.17 to 5.21.

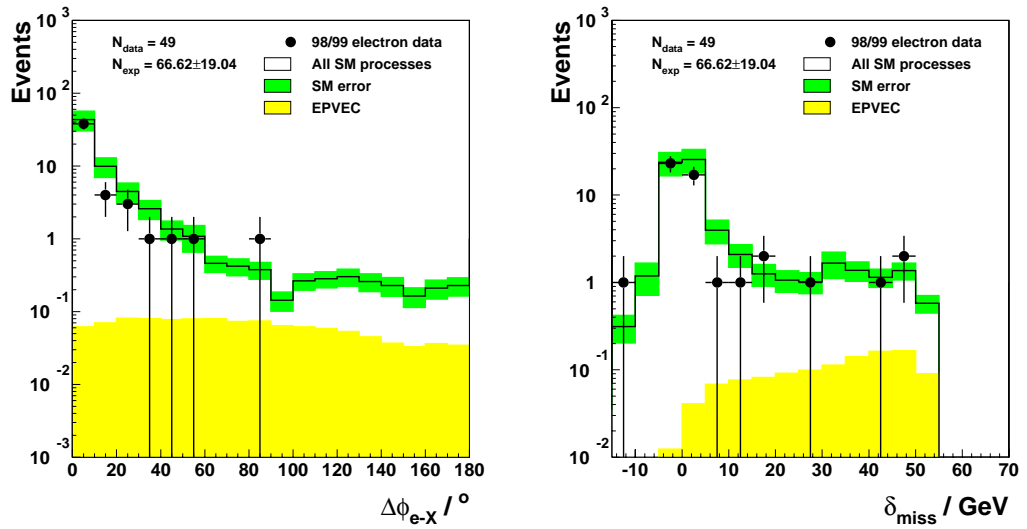


Figure 5.17: The acoplanarity (left) and the missing ( $E - p_z$ ) (right) of the electron study sample in the 98-99  $e^-p$  data.

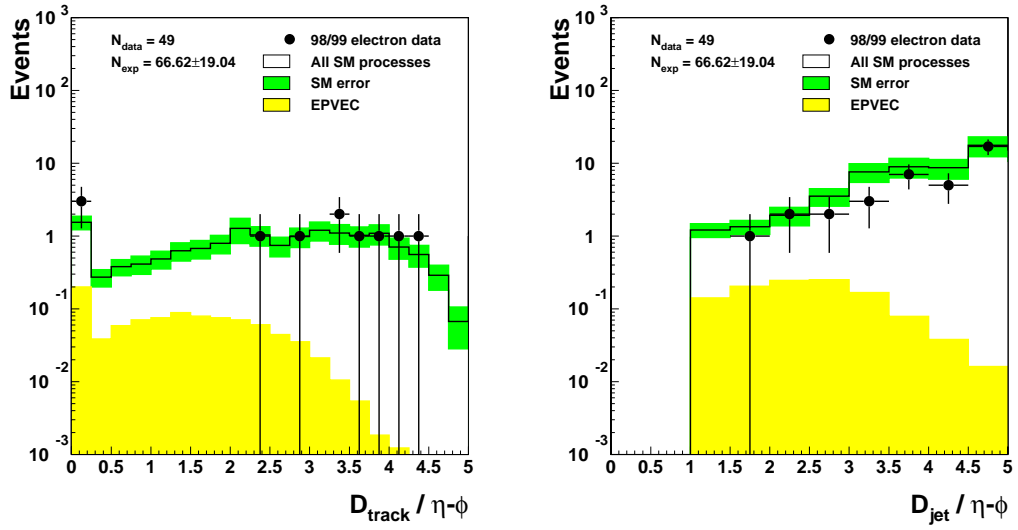


Figure 5.18: The distances  $D_{track}$  (left) and  $D_{jet}$  (right) of the electron study sample in the 98-99  $e^-p$  data.

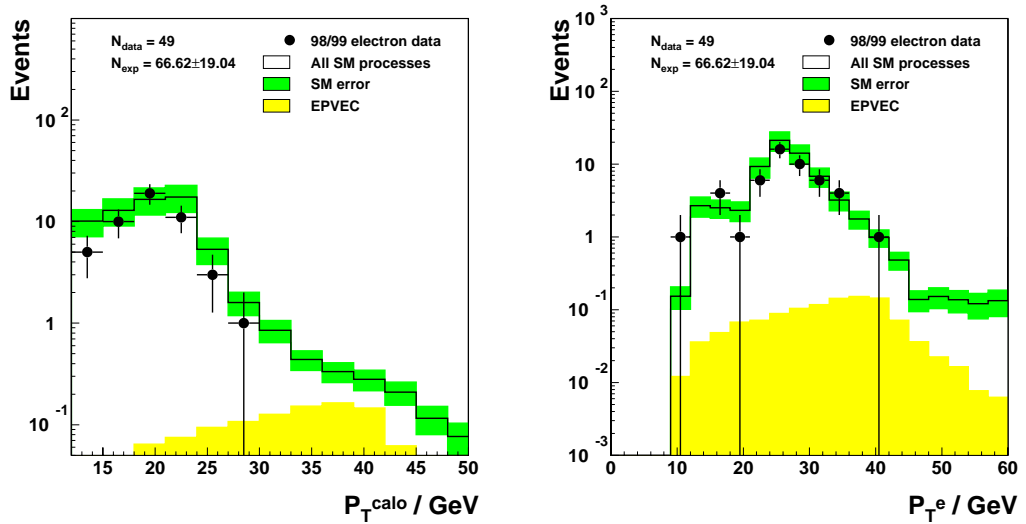


Figure 5.19: The calorimetric missing transverse momentum (left) and the transverse momentum of the electron (right) of the electron study sample in the 98-99  $e^-p$  data.

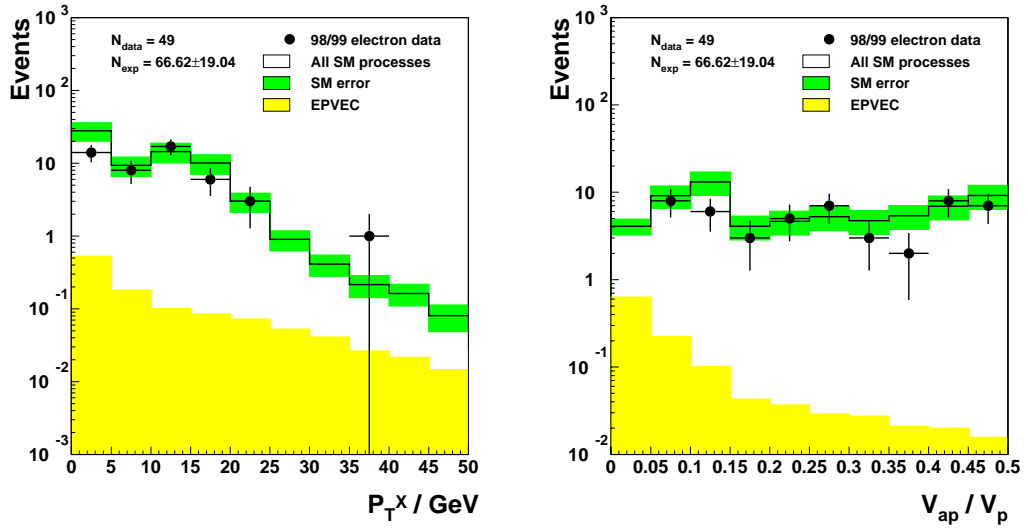


Figure 5.20: The transverse momentum of the hadronic final state,  $P_T^X$  (left), and the azimuthal balance (right) of the electron study sample in the 98-99  $e^-p$  data.

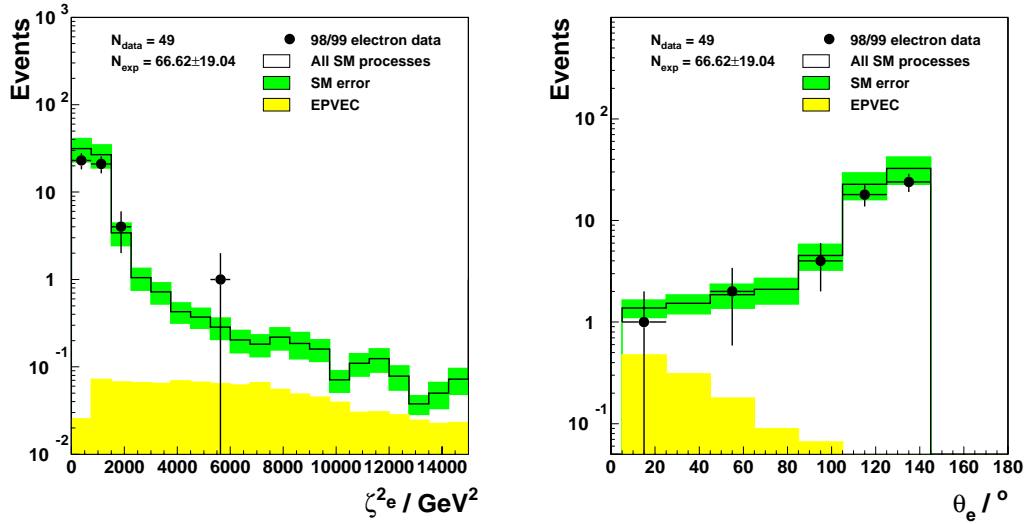


Figure 5.21: The  $\zeta^2(Q^2)$  (left) and  $\theta$  (right) distributions of the electron study sample in the 98-99  $e^-p$  data.

### 5.7.2 Selecting the Muon Channel : $ep \rightarrow eWX \rightarrow e\mu\nu X$

The study sample for the muon decay channel is defined using similar criteria to those outlined in section 5.7.1 for the electron decay channel. In this channel the dominant backgrounds are due to the inelastic di-photon process  $ep \rightarrow e\mu^+\mu^-X$  and photoproduction events containing a muon.

The differences in the selection criteria for the study sample reflect the fact that a muon will typically deposit little energy in the calorimeters of H1, and will be absorbed predominantly in the instrumented iron. The background processes in this channel are much closer in size to the signal. The correspondingly weaker need for background rejecting cuts allows a greater acceptance in the muon channel than in the electron channel (see section 7.3).

The study sample for the muon decay channel is defined by the following selection requirements :

- $\frac{V_{ap}}{V_p} < 0.4$  ( $< 0.15$  for  $P_T^{calo} < 25$  GeV)
- $P_T^\mu > 5$  GeV
- $5^\circ < \theta_\mu < 145^\circ$
- $D_{jet} > 1.0$
- $P_T^{calo} > 12$  GeV
- At least one isolated muon satisfying the muon identification criteria for the final sample. Further muons need only satisfy the less stringent identification criteria (see section 5.4.2).

## The positron-proton data

This procedure selects 28 data events for the  $e^+p$  data taken in 1994-1997 and 1999-2000. This compares well to  $28.1 \pm 15.5$  Monte Carlo events selected by the same criteria. The distributions of these real and simulated events in the variables defining the final samples are shown in figures 5.22 to 5.26.

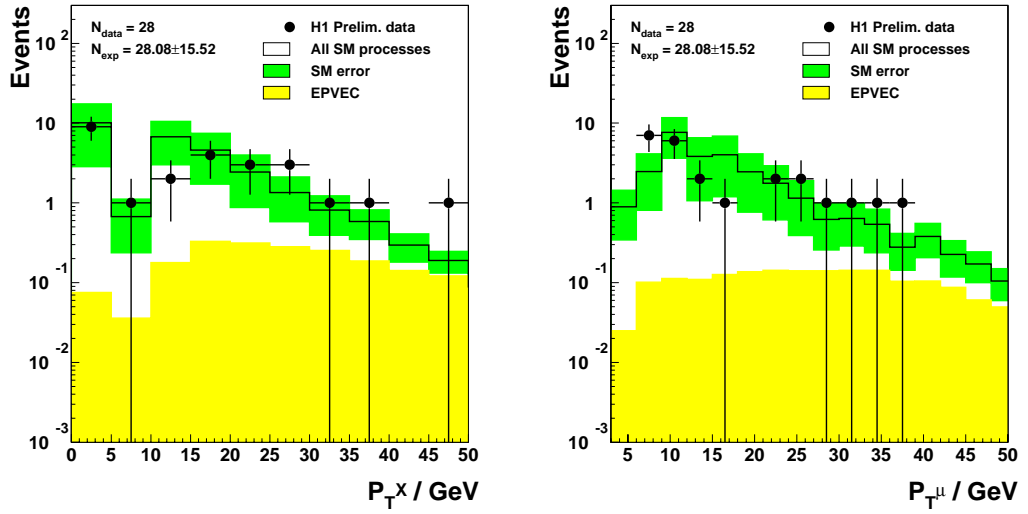


Figure 5.22: The transverse momentum of the hadronic final state,  $P_T^X$  (left), and the transverse momentum of the muon candidate (right) of the muon study sample in the 94-00  $e^+p$  data.

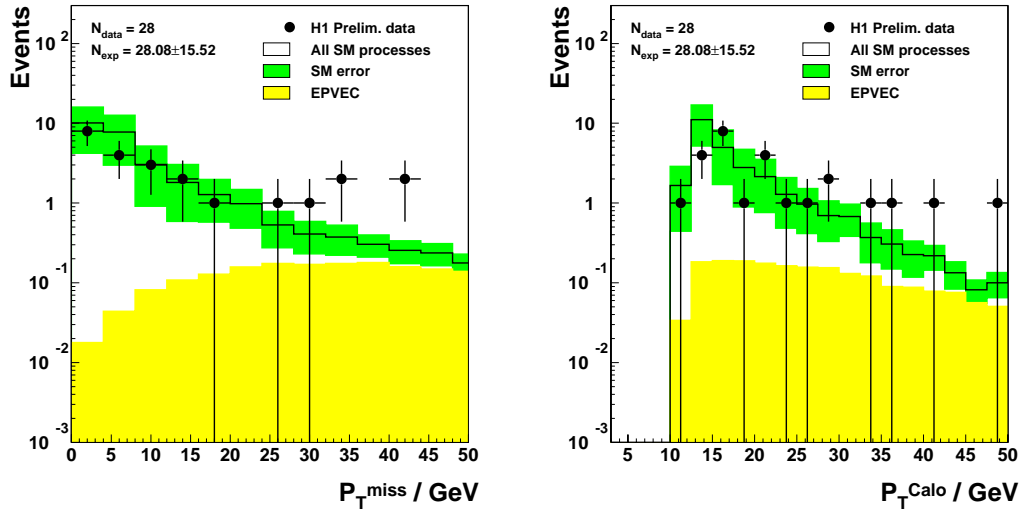


Figure 5.23: The missing transverse momentum,  $P_T^{miss}$  (left), and the missing calorimetric transverse momentum,  $P_T^{calo}$  (right) of the muon study sample in the 94-00  $e^+p$  data.

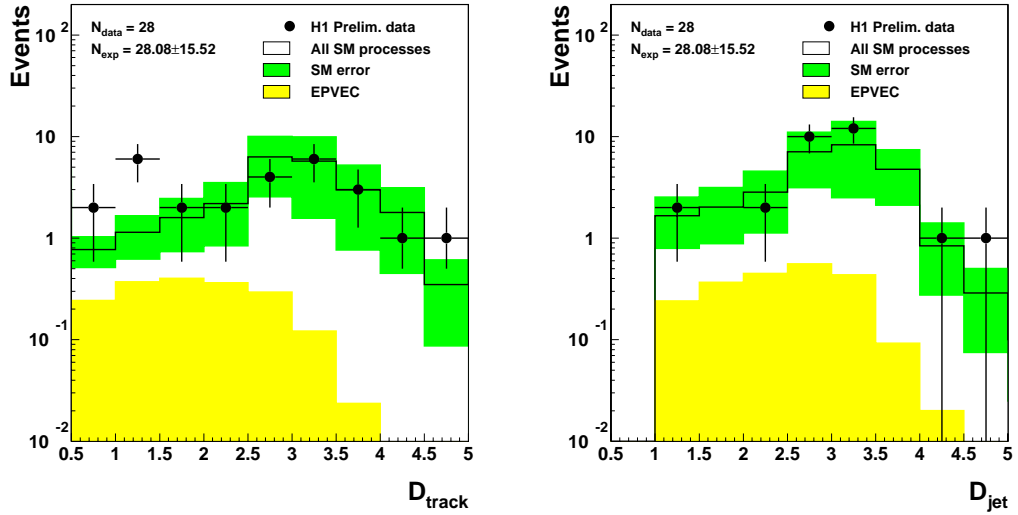


Figure 5.24: The distances  $D_{track}$  (left) and  $D_{jet}$  (right) of the muon study sample in the 94-00  $e^+p$  data.

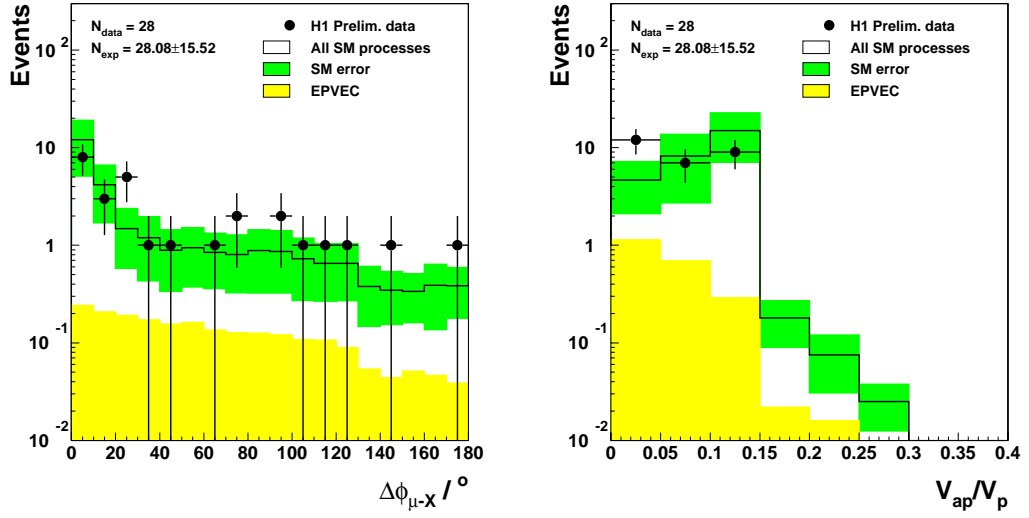


Figure 5.25: The acoplanarity (left), and azimuthal balance (right) of the muon study sample in the 94-00  $e^+p$  data.

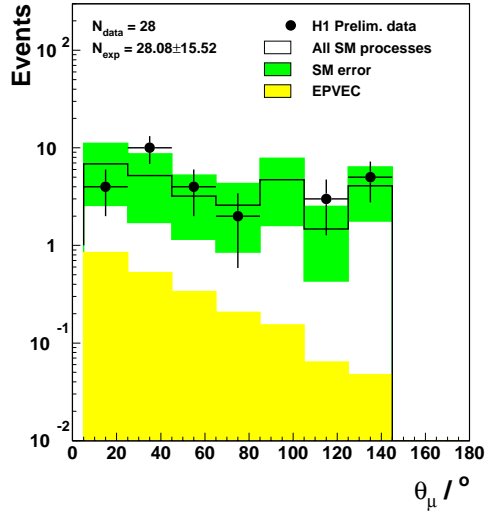


Figure 5.26: The polar angle of the muon candidate (right) of the muon study sample in the 94-00  $e^+p$  data.



## The electron-proton data

This procedure selects 4 data events for the  $e^-p$  data taken in 1998-1999. This compares to  $5.2 \pm 2.8$  Monte Carlo events selected by the same criteria. The distributions of these real and simulated events in the variables defining the final samples are shown in figures 5.27 to 5.31.

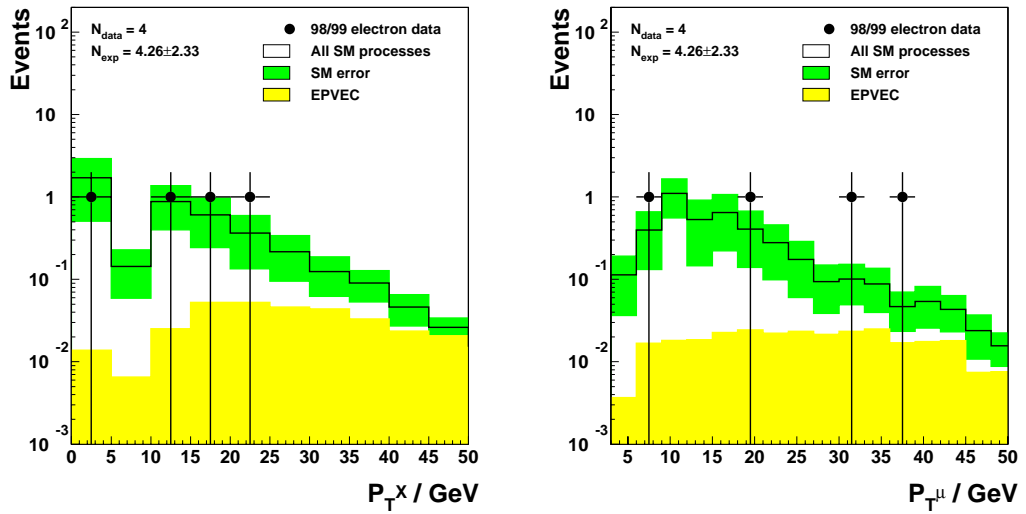


Figure 5.27: The transverse momentum of the hadronic final state,  $P_T^X$  (left), and the transverse momentum of the muon candidate (right) of the muon study sample in the 98-99  $e^-p$  data.

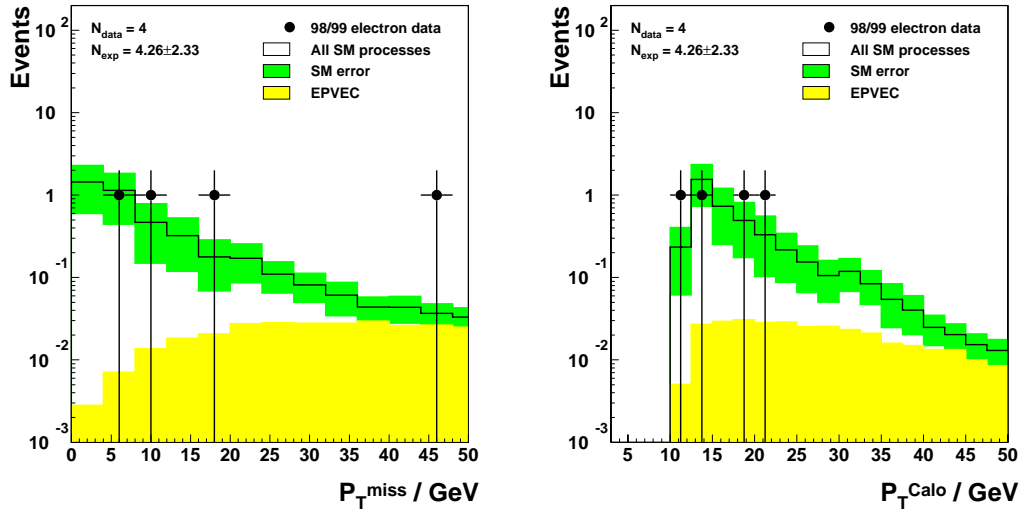


Figure 5.28: The missing transverse momentum,  $P_T^{miss}$  (left), and the missing calorimetric transverse momentum,  $P_T^{calo}$  (right) of the muon study sample in the 98-99  $e^-p$  data.

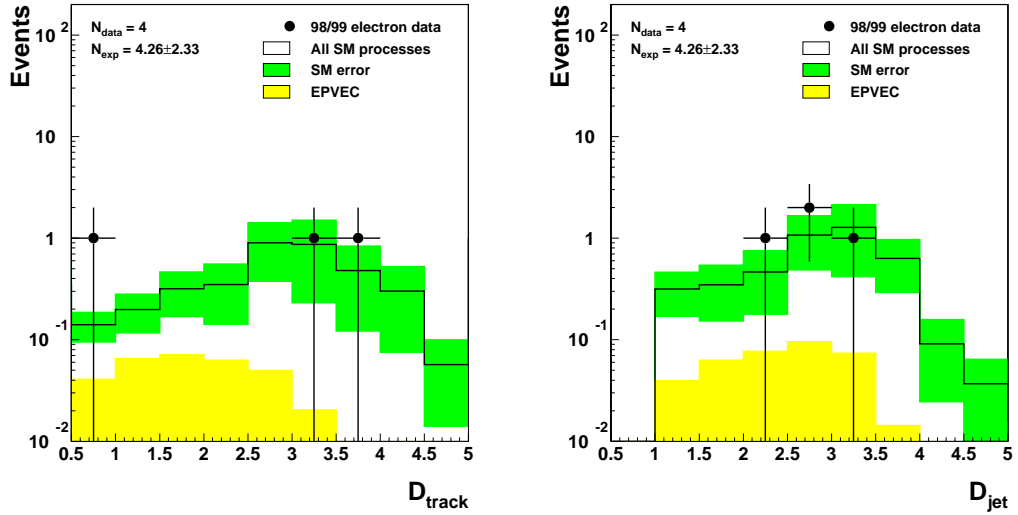


Figure 5.29: The distances  $D_{track}$  (left) and  $D_{jet}$  (right) of the muon study sample in the 98-99  $e^-p$  data.

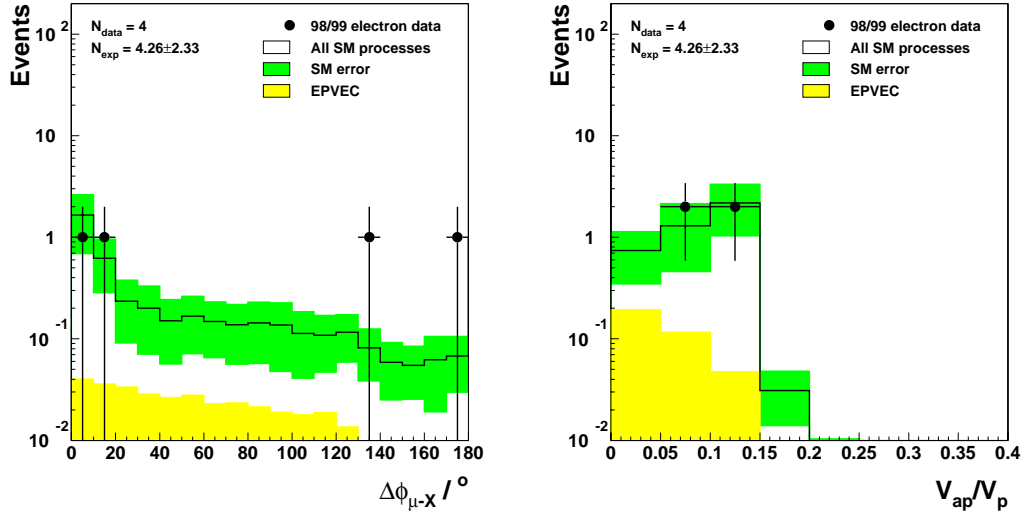


Figure 5.30: The acoplanarity (left), and azimuthal balance (right) of the muon study sample in the 98-99  $e^-p$  data.

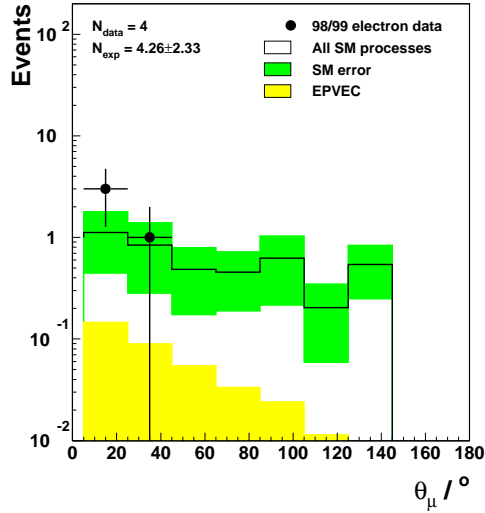


Figure 5.31: The polar angle of the muon candidate (right) of the muon study sample in the 98-99  $e^-p$  data.

# Chapter 6

## Background Studies

With the study samples defined for each decay channel, more detailed analysis of the Standard Model processes contributing to each is possible. Doing so means that the final selection criteria may be optimised for the resultant signal to background ratio. This chapter discusses first the electron channel, then the muon channel. There then follows a series of studies of samples defined to explicitly select NC, CC and muon pair ( $\mu^+\mu^-$ ) processes respectively. All studies have been carried out on the 94-00  $e^+p$  data sample.

### 6.1 Analysis of the Distributions in the Electron Channel

The study sample for the electron channel, as defined in section 5.7.1, consists predominantly of NC events. The contribution of NC processes to the Standard Model total can be seen in figures 6.1 to 6.8. The figures show the three largest components of the full Standard Model simulation. The second and third most prevalent processes are  $W$  boson production and inelastic  $\gamma\gamma \rightarrow \mu^+\mu^-$ . The latter

process contributes in the electron channel because the full process is  $ep \rightarrow e\mu^+\mu^-X$ , and hence the scattered beam electron may be misidentified as a  $W$  decay electron, and the muon lend the event significant  $P_T^{calo}$ .  $CC$  events are another significant background process and also difficult to reject because of the similarity of their topologies to  $W$  decay events. The quantity  $D_{track}$  is specifically employed to counter this background. This is expanded on in section 6.1.6.

### 6.1.1 $\zeta^2$

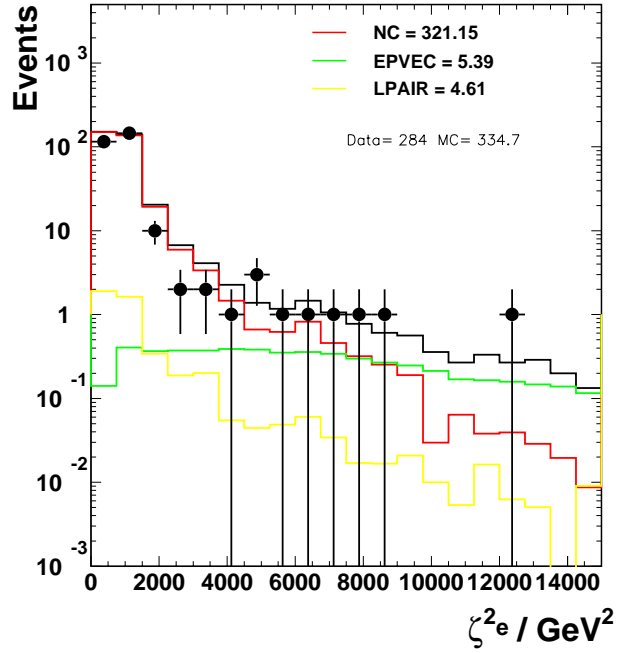


Figure 6.1: The  $\zeta^2$  distribution of the e channel study sample. Data are the points. The histograms are the full Standard Model simulation, and its NC, EPVEC and LPAIR components.

As in the original data set, before the study sample was defined, the distribution in  $\zeta^2$  of the NC component of the Standard Model simulation rises sharply at low values of  $\zeta^2$ . By contrast, the  $W$  production component (EPVEC) can be seen

to be distributed relatively evenly with  $\zeta^2$ , and in doing so becomes the dominant contribution for  $\zeta^2 > 8000 \text{ GeV}^2$ . The contribution from inelastic lepton pair events is everywhere smaller than that from  $W$  production, except at low values of  $\zeta^2$  ( $\zeta^2 < 1000 \text{ GeV}^2$ ).

$\zeta^2$  has discriminatory power for the final selection. The cut-off point is defined as  $5000 \text{ GeV}^2$ . Above this value events are accepted. In the region<sup>1</sup>  $500 < \zeta^2 < 5000 \text{ GeV}^2$  further requirements are imposed (see section 6.1.2).

### 6.1.2 $P_T^{calo}$

Like  $\zeta^2$ ,  $P_T^{calo}$  is dominated in its lower values by NC events, whereas at higher values the  $W$  decay events play an equally numerous role. The correlation between  $P_T^{calo}$  and  $\zeta^2$  for NC and for  $W$  events are shown in figure 6.3. The  $W$  events can be seen to be evenly spread across the entire kinematic plane presented. As expected from the 1-dimensional plots, NC events are densely clustered at low values of both variables, especially of  $\zeta^2$ . This correlation is utilised in the final selection, defining a cut-off at  $P_T^{calo} = 25 \text{ GeV}$ , below which the  $\zeta^2$  requirement is tightened to  $\zeta^2 > 5000 \text{ GeV}^2$ .

---

<sup>1</sup>The lower bound already defined in the study sample selection.

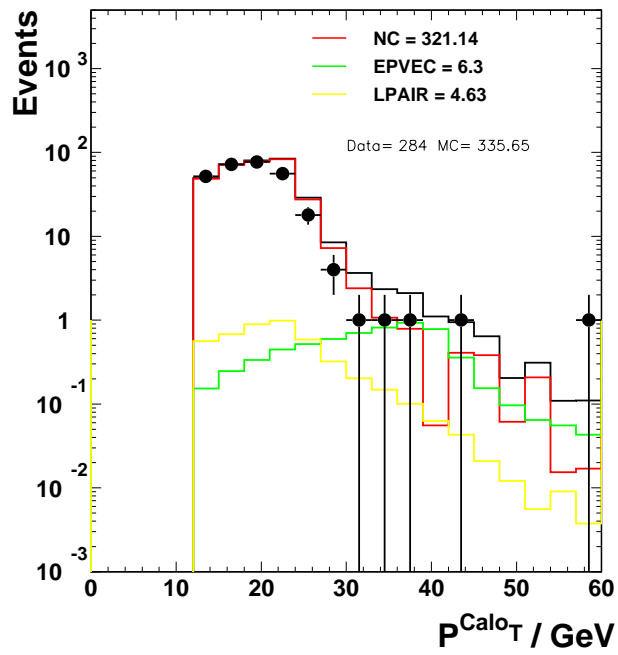


Figure 6.2: The  $P_T^{calo}$  distribution of the e channel study sample. Data are the points. The histograms are the full Standard Model simulation, and its NC, EPVEC and LPAIR components.

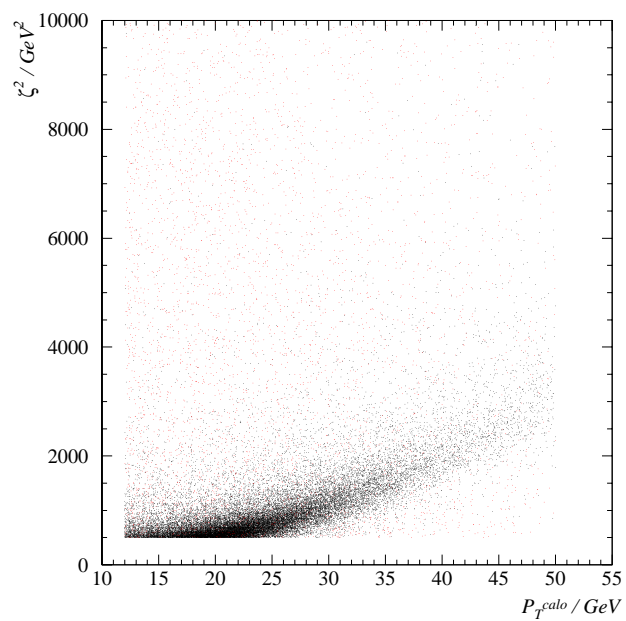


Figure 6.3: The correlation between  $P_T^{calo}$  and  $\chi^2$  of a NC simulation (black) and a  $W$  simulation (red). The  $W$  simulation is shown with a luminosity  $\approx 1000$  times that of the NC simulation for visual clarity.



### 6.1.3 $\frac{V_{ap}}{V_p}$

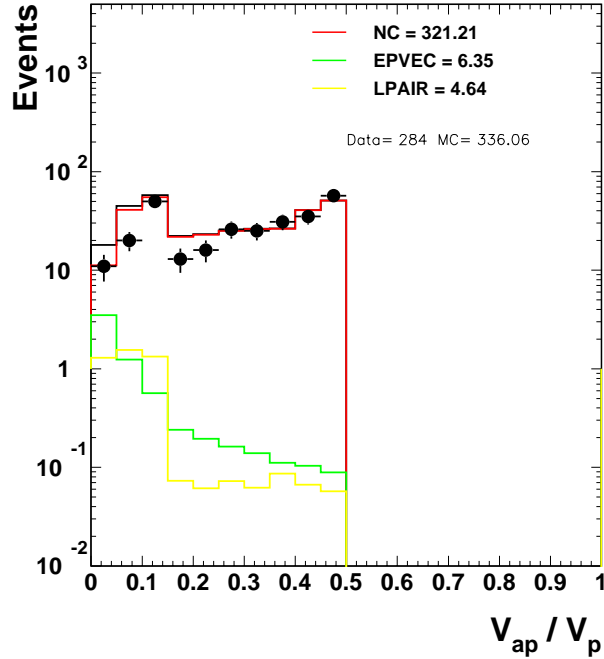


Figure 6.4: The  $\frac{V_{ap}}{V_p}$  distribution of the e channel study sample. Data are the points. The histograms are the full Standard Model simulation, and its NC, EPVEC and LPAIR components.

$\frac{V_{ap}}{V_p}$  is one of the variables forming part of the only 2-dimensional cut that selected the study sample, namely  $\frac{V_{ap}}{V_p} < 0.5$  ( $< 0.15$  for  $P_T^e < 25$  GeV). The effect of this 2-stage cut can be seen in figure 6.4, where the distributions are clearly discontinuous at  $\frac{V_{ap}}{V_p} = 0.15$ . The correlation between  $\frac{V_{ap}}{V_p}$  and  $P_T^e$  is shown in figure 6.5 for raw Monte Carlo samples (i.e. prior to the study sample selection cuts). The even spread of the NC sample across the range of  $\frac{V_{ap}}{V_p}$ , but predominantly at low  $P_T^e$ , is the motivation for the requirement that  $\frac{V_{ap}}{V_p} < 0.15$  for  $P_T^e < 25$  GeV. Greater acceptance of the  $W$  signal is achieved by allowing  $\frac{V_{ap}}{V_p}$  up to 0.5 for  $P_T^e > 25$  GeV.

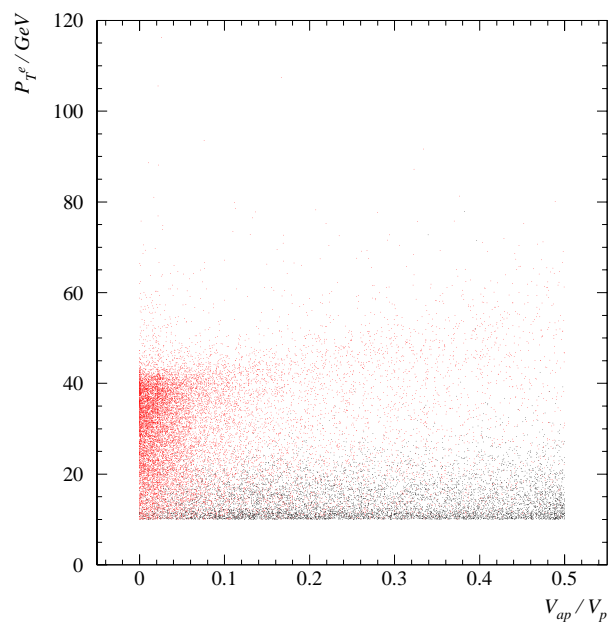


Figure 6.5: The correlation between  $\frac{V_{ap}}{V_p}$  and  $P_T^e$  of a NC simulation (black) and a  $W$  simulation (red). The  $W$  simulation is shown with a luminosity  $\approx 1000$  times that of the NC simulation for visual clarity.

### 6.1.4 $\delta_{miss}$

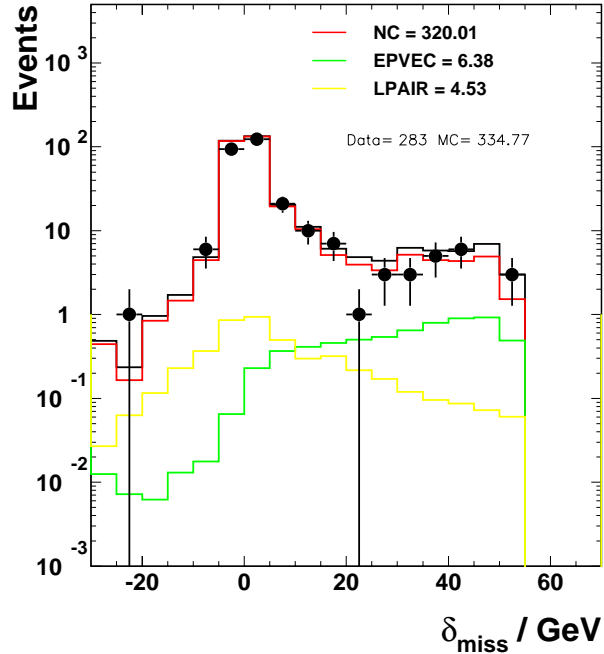


Figure 6.6: The  $\delta_{miss}$  distribution of the e channel study sample. Data are the points. The histograms are the full Standard Model simulation, and its NC, EPVEC and LPAIR components.

$\delta_{miss}$ , a constructed measure of the longitudinal momentum balance, is a useful discriminant. In figure 6.6, for both the NC and lepton pair components of the Standard Model simulation (both intrinsically balanced events),  $\delta_{miss}$  can be seen to peak at 0 GeV, whereas the distribution of  $\delta_{miss}$  for  $W \rightarrow l\nu$  events (imbalanced due to the neutrino) can be seen to rise towards positive values of  $\delta_{miss}$ .

By inspection (figure 6.6) there is a turning point at around 5 GeV. Not only do NC events peak strongly just below this, but it also represents the point above which  $W \rightarrow l\nu$  events begin to dominate over inelastic lepton pair events. This can be used as a discriminator for the final event selection. It is, however, only brought into play if only one electron candidate is detected, which has the same charge as

the beam lepton, since this is the signature of a NC event.

### 6.1.5 $\Delta\phi_{e-X}$

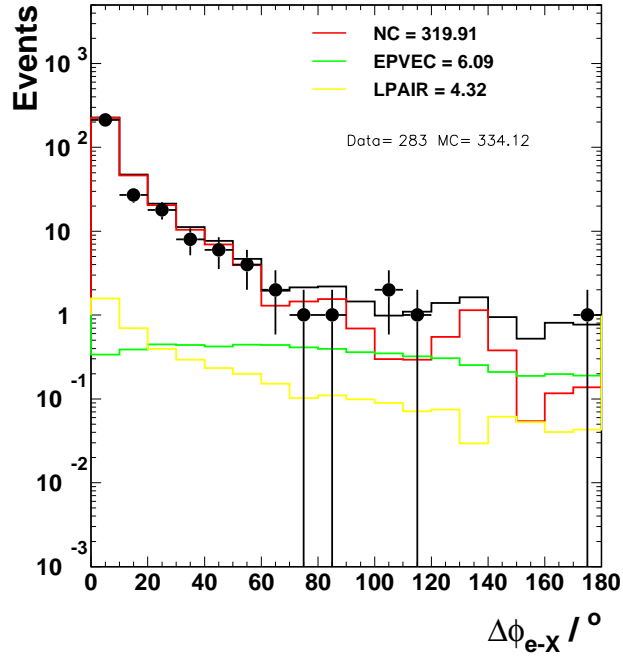


Figure 6.7: The  $\Delta\phi_{e-X}$  distribution of the e channel study sample. Data are the points. The histograms are the full Standard Model simulation, and its NC, EPVEC and LPAIR components.

As discussed in section 5.7.1, the acoplanarity of an event can be a powerful tool in the selection of  $W \rightarrow e\nu$  events and the rejection of NC events. Without detector effects such as smearing and cracks, a NC event should have no acoplanarity. This is clear from figure 6.7, with regard to the strong peak at  $0^\circ$  which can be seen to be almost entirely attributable to the NC component.  $W \rightarrow e\nu$  events are distributed rather evenly in acoplanarity, albeit with a weak peak between  $40^\circ$  and  $80^\circ$ .

In the final event sample events are only accepted which have an acoplanarity

greater than  $20^\circ$ . This is also the point where  $W \rightarrow l\nu$  events begin to dominate over inelastic lepton pair events.

### 6.1.6 $D_{track}$

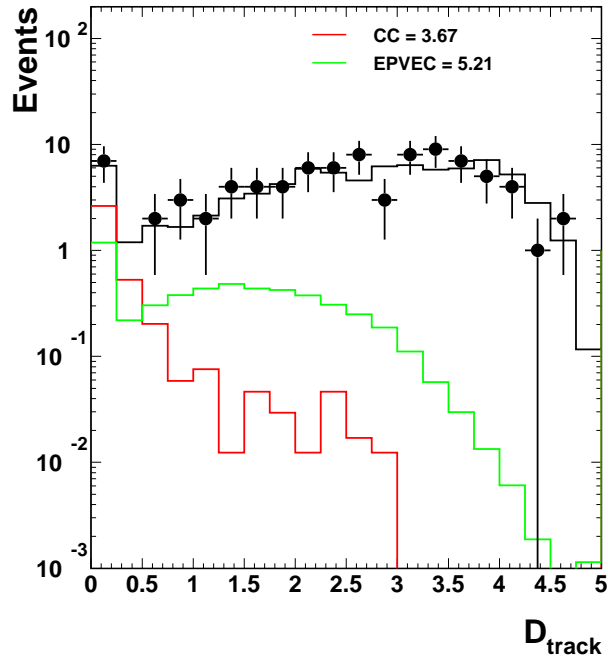


Figure 6.8: The  $D_{track}$  distribution of the e channel study sample. Data are the points. The histograms are the full Standard Model simulation, and its NC, EPVEC and LPAIR components.

$D_{track}$ , the distance in  $\eta - \phi$  space from the electron candidate to the nearest track, is employed to reject CC events. Figure 6.8 shows the full Standard Model simulation and its  $W \rightarrow e\nu$  (EPVEC) and CC (DJANGO) components. The sharp rise of the CC component at low values of  $D_{track}$  can be clearly seen. Substantial rejection of CC events from the final sample is achieved by only selecting events with  $D_{track} > 0.5$ .

This quantity loses discriminatory power in the forward region of the detector, where the particle flux is higher and where showering in the passive layers of the FTD spoils a track's isolation. For this reason the  $D_{track}$  cut is only made for  $\theta_e > 45^\circ$ . However, to preserve the quality of the electron candidates, the  $D_{track}$  cut is imposed when  $\frac{E_{cone}}{E^l} > 0.05$ , i.e. an electron candidate must either be well isolated or have particularly clean energy deposition in the calorimeter.

### 6.1.7 $P_T^X$

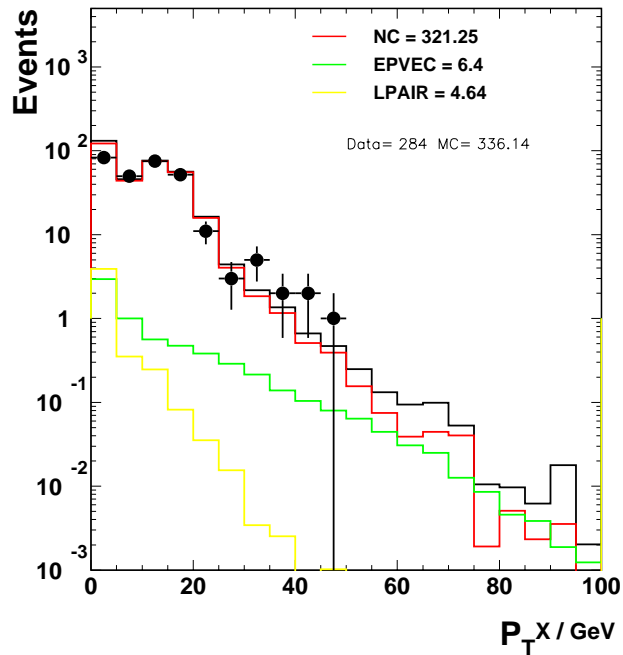


Figure 6.9: The  $P_T^X$  distribution of the e channel study sample. Data are the points. The histograms are the full Standard Model simulation, and its NC, EPVEC and LPAIR components.

$P_T^X$ , the transverse momentum the hadronic final state, is not cut on in selecting the final sample. However, this quantity is of particular interest in the analysis of the final event sample, and as such it worthwhile to note at this stage that the

distributions of the three main contributions to the Standard Model simulation all fall off exponentially with increasing  $P_T^X$ . Importantly, the  $W \rightarrow e\nu$  (EPVEC) distribution falls off least fast.

## 6.2 Analysis of the Distributions in the Muon Channel

The study sample for the muon channel, as defined in section 5.7.2, is considerably smaller than the electron channel study sample (284 data events). This is due to the absence in the muon channel of an equivalent to the NC process in the electron channel. In this channel the study sample consists of 28 data events. The Monte Carlo simulation predicts 28.1 events, 20.1 from lepton pair events ( $\gamma\gamma \rightarrow \mu^+\mu^-$ ), 5.0 from  $\gamma p$  events and 2.2 from  $W$  decay events. The distribution of the data and simulated events with respect to key quantities can be seen in figures 6.10 to 6.15. The figures show the three largest components of the full Standard Model simulation.



### 6.2.1 $P_T^\mu$

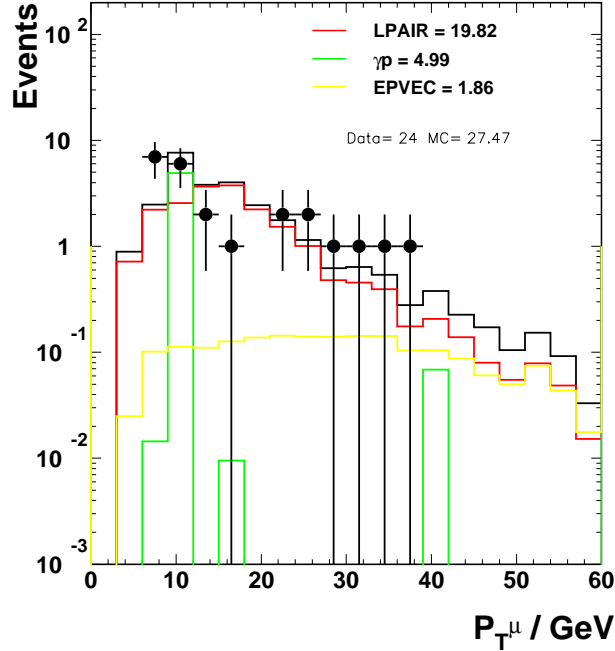


Figure 6.10: The  $P_T^\mu$  distribution of the  $\mu$  channel study sample. Data are the points. The histograms are the full Standard Model simulation, and its LPAIR,  $\gamma p$  and EPVEC components.

The simulated  $W \rightarrow \mu\nu$  events are distributed relatively evenly in  $P_T^\mu$ , albeit with a fall-off below 10 GeV. The inelastic muon pair contribution can be seen to fall steadily from 10 GeV. At around 45 GeV the  $W$  and muon pair contributions become comparable in size. The  $\gamma p$  (low  $Q^2$  NC) component has a rather discontinuous distribution in this sample. This is due to the huge cross section for this process, and hence despite the fact that enormous numbers of events have been generated and reconstructed for this simulation, the correspondingly small luminosity means that individual events have large weights, resulting in the “spiky” distributions.

## 6.2.2 $\frac{V_{ap}}{V_p}$

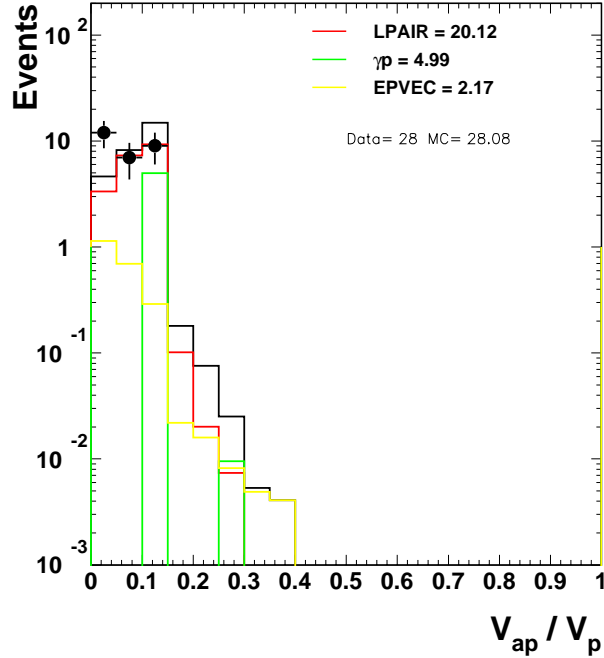


Figure 6.11: The  $\frac{V_{ap}}{V_p}$  distribution of the  $\mu$  channel study sample. Data are the points. The histograms are the full Standard Model simulation, and its LPAIR,  $\gamma p$  and EPVEC components.

As in the electron channel,  $\frac{V_{ap}}{V_p}$  is one of the variables forming part of the only 2-dimensional cut that selected the study sample, namely  $\frac{V_{ap}}{V_p} < 0.4$  ( $< 0.15$  for  $P_T^{calo} < 25$  GeV). The effect of this 2-stage cut can be seen in figure 6.4, where the distributions are clearly discontinuous at  $\frac{V_{ap}}{V_p} = 0.15$ . The correlation between  $\frac{V_{ap}}{V_p}$  and  $P_T^{calo}$  is shown in figure 6.12 for raw Monte Carlo samples (i.e. prior to the study sample selection cuts). The  $W$  signal becomes extremely weak above  $\frac{V_{ap}}{V_p} = 0.4$ , and no selection is made above this value. For  $\frac{V_{ap}}{V_p} < 0.4$ , background processes (particularly inelastic muon pair events) are rather densely distributed in the region  $P_T^{calo} < 25$  GeV until very low values of  $\frac{V_{ap}}{V_p}$ . For this reason the cut is made such that  $\frac{V_{ap}}{V_p} < 0.15$  for  $P_T^{calo} < 25$  GeV.

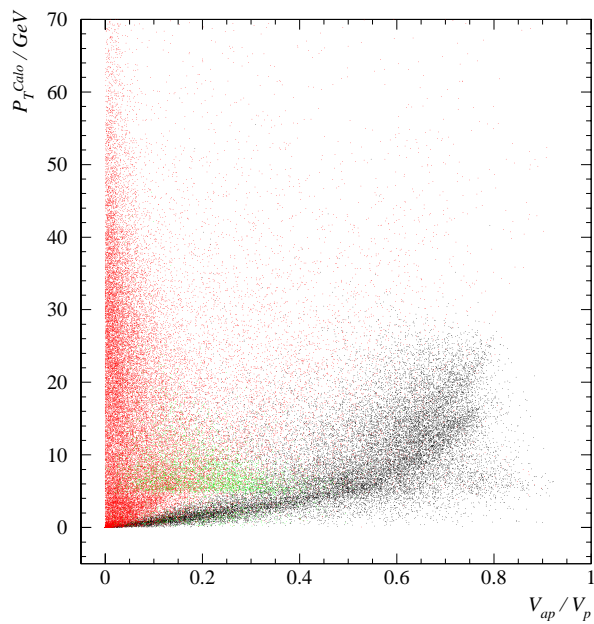


Figure 6.12: The correlation between  $\frac{V_{ap}}{V_p}$  and  $P_T^{calo}$  of a NC simulation (black), an inelastic  $\gamma\gamma \rightarrow \mu^+\mu^-$  simulation (green) and a  $W$  simulation (red). For visual clarity the  $W$  simulation is shown with a luminosity  $\approx 1000$  times that of the NC simulation, and the inelastic  $\gamma\gamma \rightarrow \mu^+\mu^-$  simulation is shown with a luminosity  $\approx 100$  times that of the NC simulation.

### 6.2.3 $\Delta\phi_{\mu-X}$

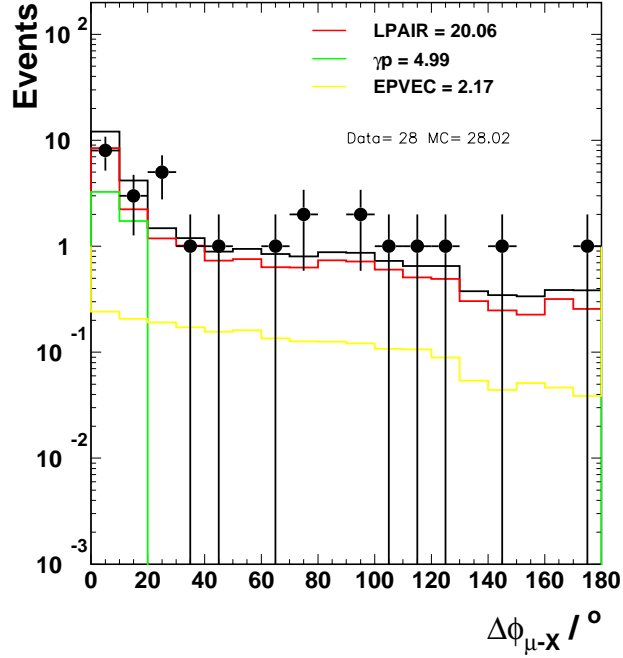


Figure 6.13: The  $\Delta\phi_{\mu-X}$  distribution of the  $\mu$  channel study sample. Data are the points. The histograms are the full Standard Model simulation, and its LPAIR,  $\gamma p$  and EPVEC components.

In the muon study sample the acoplanarity does not have the same discriminatory power as in the electron channel. However, like in the electron channel, the main background process (muon pair) is peaked at  $0^\circ$ . The rejection of these events can be optimised by rejecting low values of acoplanarity, for events with a low central track multiplicity. Muon pair events are characterised by 2 (or 1 if one is lost) central tracks.

### 6.2.4 $D_{track}$

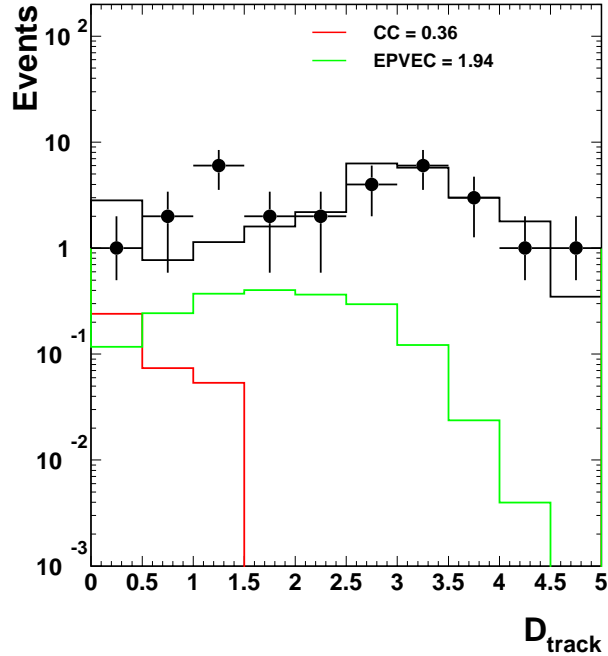


Figure 6.14: The  $D_{track}$  distribution of the  $\mu$  channel study sample. Data are the points. The histograms are the full Standard Model simulation, and its LPAIR,  $\gamma p$  and EPVEC components.

Like in the electron channel the quantity  $D_{track}$  is used for the rejection of CC events. Figure 6.14 shows the full Standard Model simulation and its  $W \rightarrow \mu\nu$  (EPVEC) and CC (DJANGO) components. The sharp rise of the CC component at low values of  $D_{track}$  can be clearly seen. Substantial rejection of CC events from the final sample is achieved by only selecting events with  $D_{track} > 0.5$ .

### 6.2.5 $P_T^X$

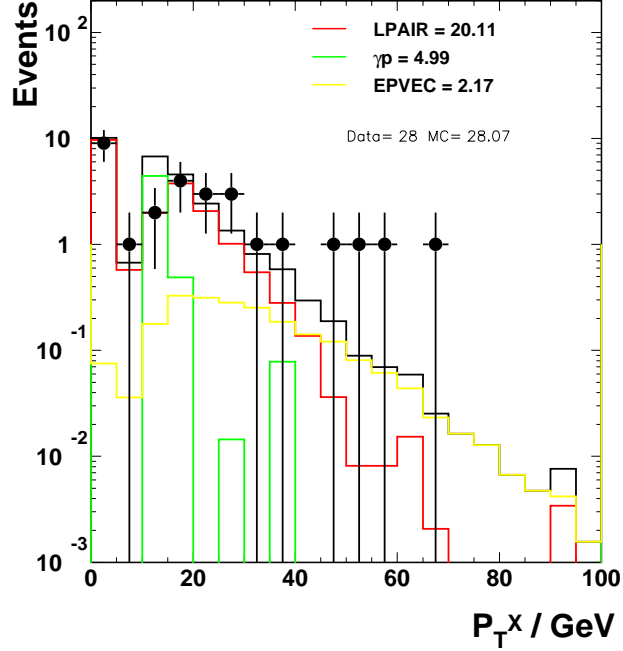


Figure 6.15: The  $P_T^X$  distribution of the  $\mu$  channel study sample. Data are the points. The histograms are the full Standard Model simulation, and its LPAIR,  $\gamma p$  and EPVEC components.

The  $P_T^X$  distributions of the electron and muon channels are similar towards higher values of  $P_T^X$ , but differ crucially at low  $P_T^X$ . It can be seen in figure 6.15 that like in the electron channel, the  $W$  component of the muon channel becomes more and more significant towards higher  $P_T^X$ . The clear difference in the muon channel comes where there is a noticeable drop in the  $P_T^X$  distribution below 12 GeV. This is due to the  $P_T^{calo} > 12$  GeV cut on the study sample. Muons deposit little energy in the calorimeters, and hence the  $P_T^{calo}$  cut is effectively a  $P_T^X$  cut. The spike at  $P_T^X = 0$  GeV is due to elastic muon pair processes, which have little or no hadronic final state, and it is the scattered electron that has provided the event's  $P_T^{calo}$ .

### 6.3 A NC Study Sample

The MC description of NC events has been checked. An event sample of NC data events and a sample of MC NC events containing high  $P_T$  tracks are compared in figures 6.16 and 6.17. Figure 6.16 shows the  $D_{track}$  and  $D_{jet}$  distributions of all tracks with transverse momentum greater than 1 GeV. Figure 6.17 shows the same distributions for all tracks with transverse momentum greater than 10 GeV.

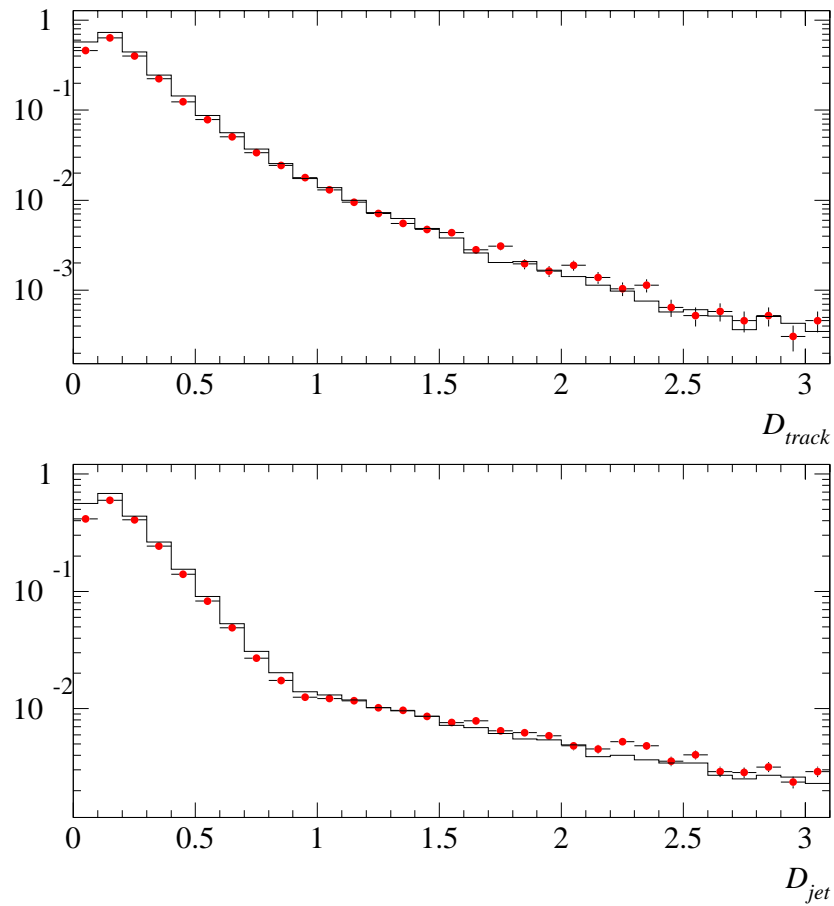


Figure 6.16: The  $D_{track}$  and  $D_{jet}$  distributions of all tracks with  $P_T > 1$  GeV in the NC study sample. The plots are shown divided by the total number of events, such that the area is the number of tracks per event. The data are the points. The histogram is the DJANGO simulation. From [82].

It can be seen from these figures that both  $D_{track}$  and  $D_{jet}$  distributions are well described in both shape and normalisation. This is true for both the  $P_T > 1$  GeV and the  $P_T > 10$  GeV sample. There is however some discrepancy between the data and the simulation at low values of  $D_{jet}$  and  $D_{track}$  in the  $P_T > 10$  GeV sample. The simulation overestimates the number of events with a high  $P_T$  track at the core of a jet.

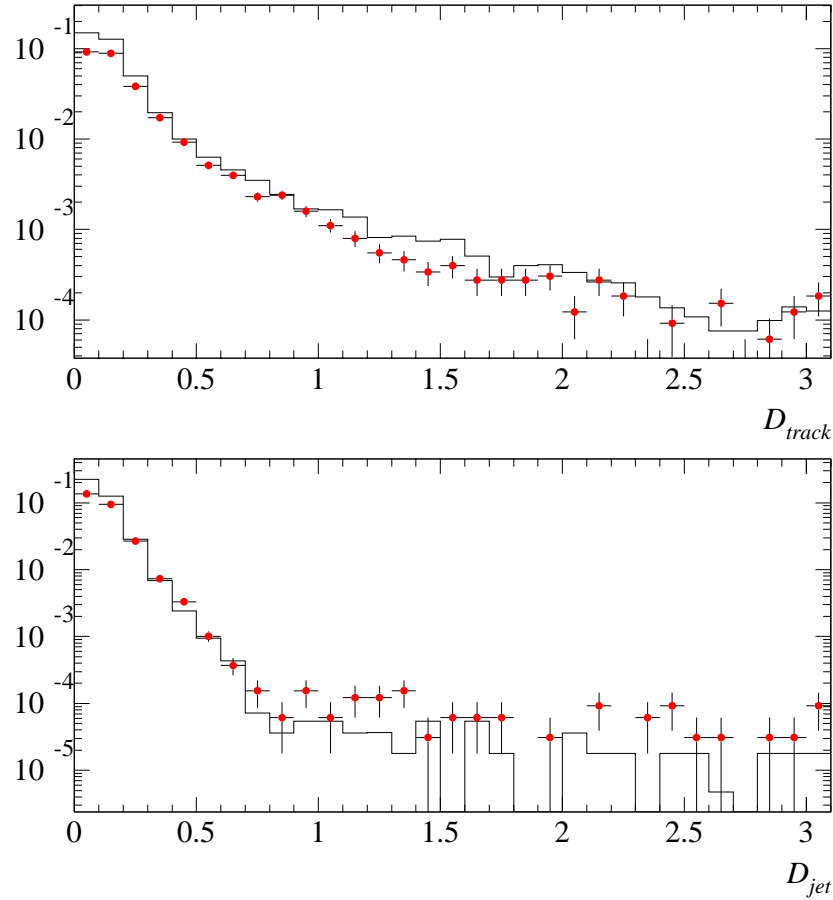


Figure 6.17: The  $D_{track}$  and  $D_{jet}$  distributions of all tracks with  $P_T > 10$  GeV in the NC study sample. The plots are shown divided by the total number of events, such that the area is the number of tracks per event. The data are the points. The histogram is the DJANGO simulation. From [82].



## 6.4 A CC Study Sample

The MC description of CC events with an identified electron has also been checked. An event sample of CC events (data and MC) is subjected to the electron finding algorithm described in section 5.4.1. The resulting samples are presented in figures 6.18 and 6.19.

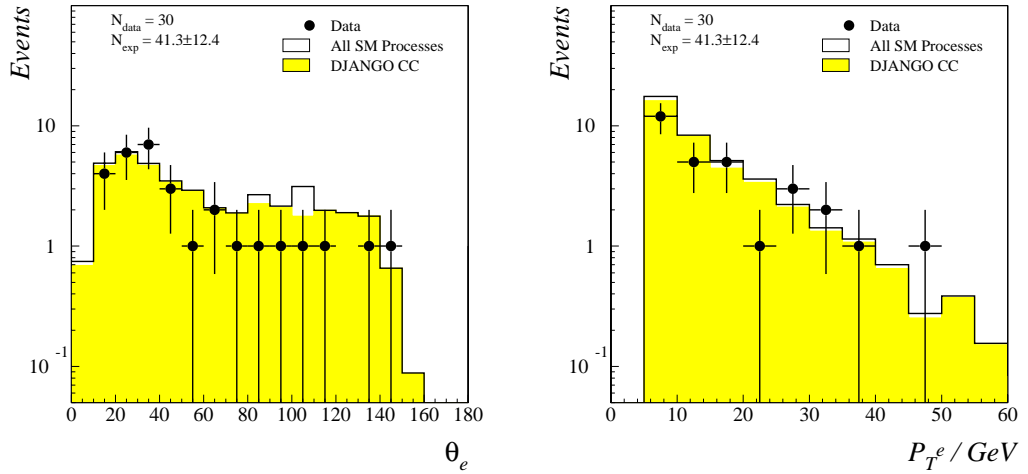


Figure 6.18: The  $\theta_e$  and  $P_T^e$  distributions of the CC+identified electron study sample. Data are the points. The empty histogram is the full Standard Model simulation and the yellow histogram is its DJANGO CC component. From [82].

It is these studies that lead to the quotation of a systematic error of 30% in section 4.3 on the contribution of CC processes. The shape is well described in all variables; only the normalisation carries the uncertainty.

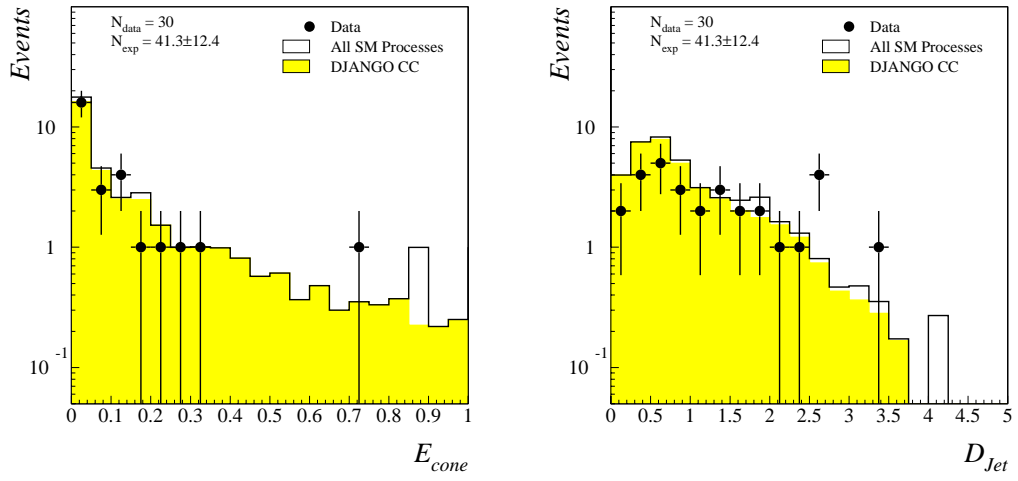


Figure 6.19: The  $E_{cone}$  and  $D_{jet}$  distributions of the CC+identified electron study sample. Data are the points. The empty histogram is the full Standard Model simulation and the yellow histogram is its DJANGO CC component. From [82].

## 6.5 A $\mu^+\mu^-$ Study Sample

As discussed in section 6.2 the main component of the muon study sample are muon pair events. An explicit study of this process is made by selecting a subset of the muon study sample with the requirement that there are at least two muons in the event. The distributions of the data and MC events selected in this manner are shown in figures 6.20 and 6.21.

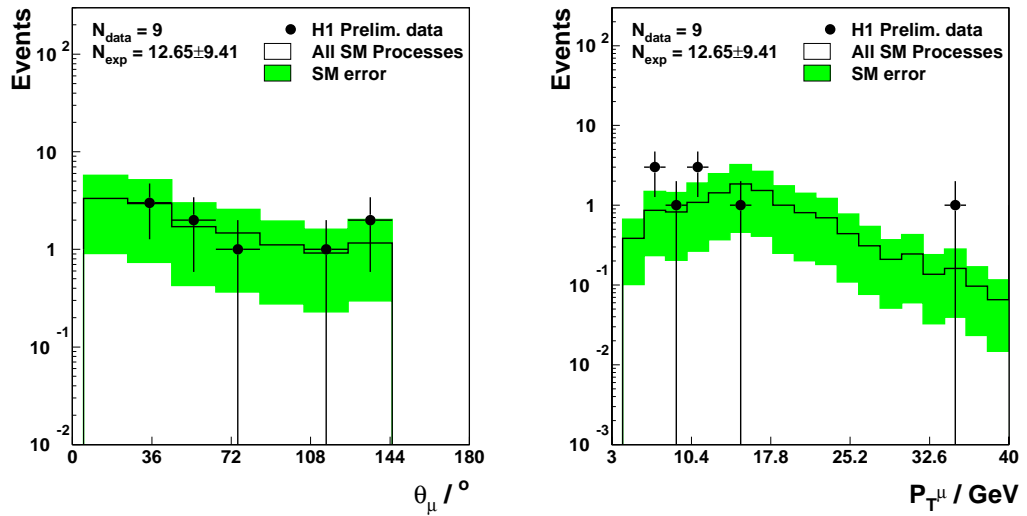


Figure 6.20: The  $\theta_\mu$  and  $P_T^\mu$  distributions of the events in the  $\mu^+\mu^-$  study sample. Data are the points. The histogram is the full Standard Model simulation, consisting almost exclusively of  $\mu^+\mu^-$  events. The green band illustrates the quoted 75% error on the  $\mu^+\mu^-$  simulation.

The systematic error of 75% quoted on the LPAIR contribution is illustrated in figures 6.20 and 6.21. This is a very conservative estimate, originating from uncertainties in the cross section calculation. This study shows this error to be ample to cover any discrepancy between MC and data.

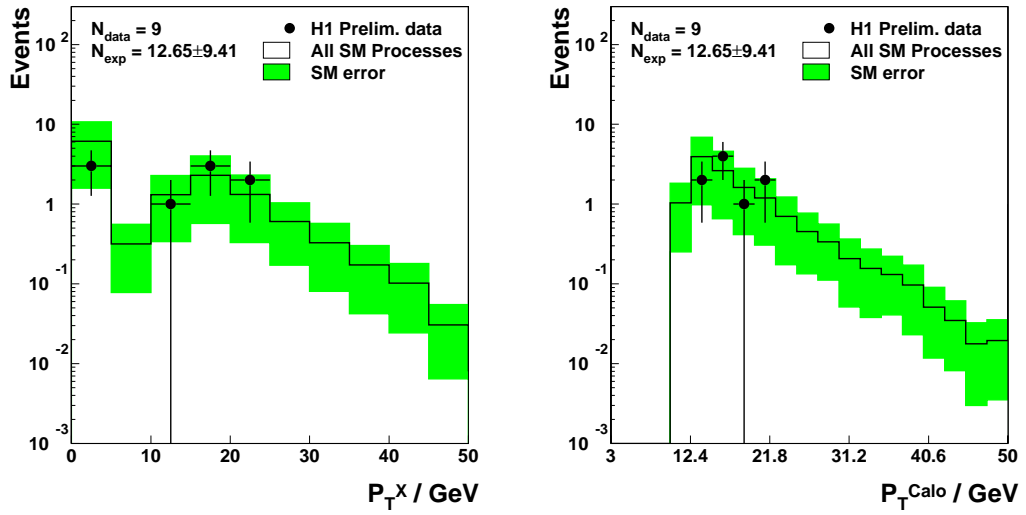


Figure 6.21: The  $P_T^X$  and  $P_T^{calo}$  distributions of the events in the  $\mu^+\mu^-$  study sample. Data are the points. The histogram is the full Standard Model simulation, consisting almost exclusively of  $\mu^+\mu^-$  events. The green band illustrates the quoted 75% error on the  $\mu^+\mu^-$  simulation.

# Chapter 7

## Event Selection : Part II

This chapter presents the selection criteria which identify the final event samples in both electron and muon decay channels. Detailed analysis of the distributions of several variables in each channel (sections 6.1 and 6.2) has paved the way for the optimised selection of  $W \rightarrow e\nu$  and  $W \rightarrow \mu\nu$  events.

### 7.1 The Final Selection of the Electron Channel

#### 7.1.1 The Cuts

The selection criteria for the electron channel study sample are defined in section 5.7.1. The final event sample is then selected as a subset of the study sample by the following criteria:

- $\zeta^2 > 5000 \text{ GeV}^2$  for  $P_T^{calo} < 25 \text{ GeV}$
- $\Delta\phi_{e-X} > 20^\circ$
- $\delta_{miss} > 5 \text{ GeV}$ <sup>1</sup>

---

<sup>1</sup>Applied if only one electron candidate is detected, which has the same charge as the beam

- $D_{track} > 0.5$  for
  - $\theta_e \geq 45^\circ$
  - $\frac{E_{cone}}{E^t} > 0.05$
- No isolated muons

The justification for these cuts has been discussed and presented in sections 6.1.1 to 6.1.7. The requirement of no isolated muons is imposed on the electron sample so that any given event may only be selected in one channel, not both.

## 7.1.2 Distributions of the Final Electron Selection

### The positron-proton data

The distributions of the data and simulation are shown in figures 7.1 to 7.5.

---

lepton.

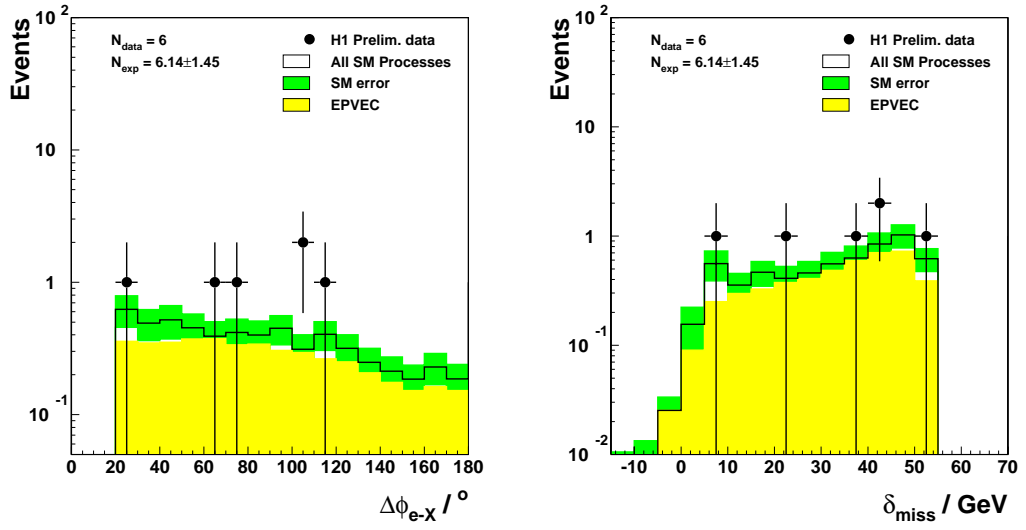


Figure 7.1: The acoplanarity (left) and the missing ( $E - p_z$ ) (right) of the final electron selection in the 94-00  $e^+p$  data.

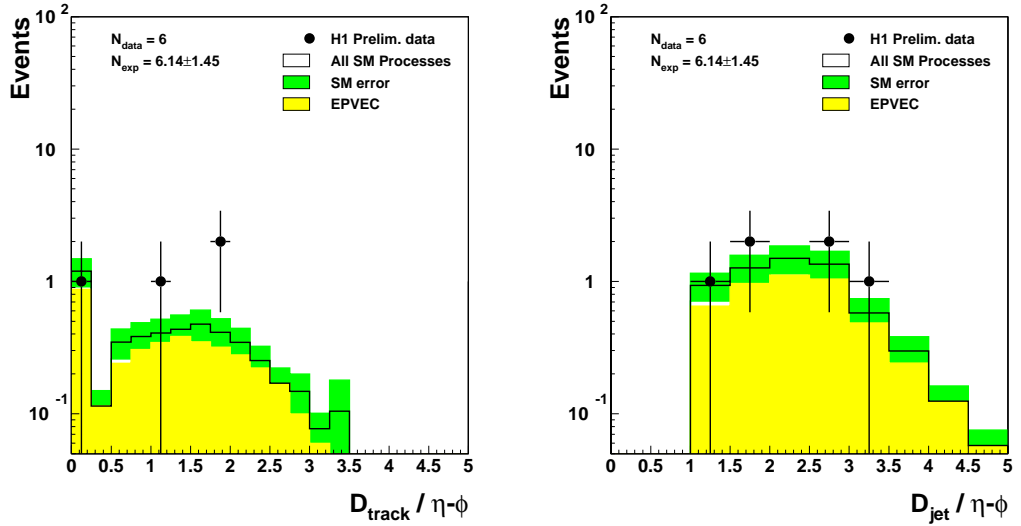


Figure 7.2: The distances  $D_{track}$  (left) and  $D_{jet}$  (right) of the final electron selection in the 94-00  $e^+p$  data.

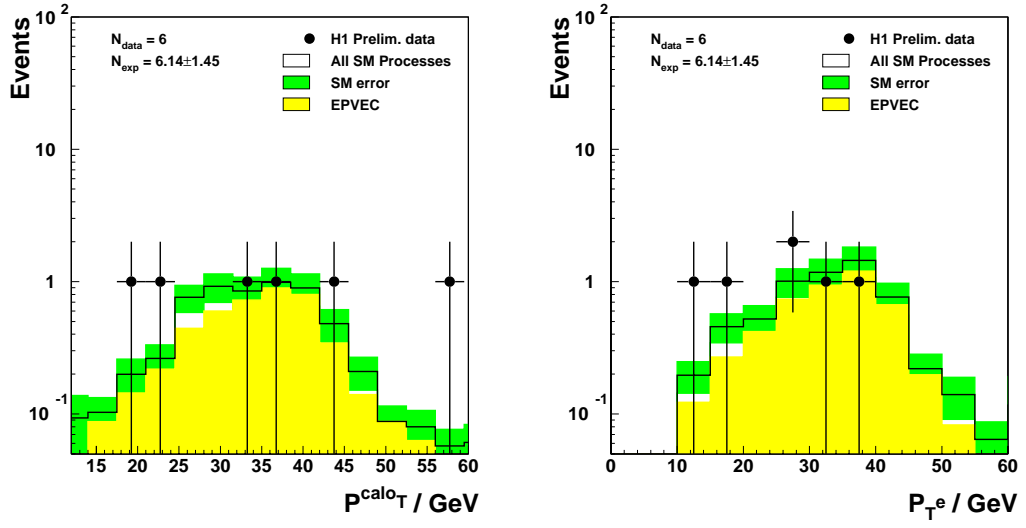


Figure 7.3: The calorimetric missing transverse momentum (left) and the transverse momentum of the electron (right) of the final electron selection in the 94-00  $e^+p$  data.

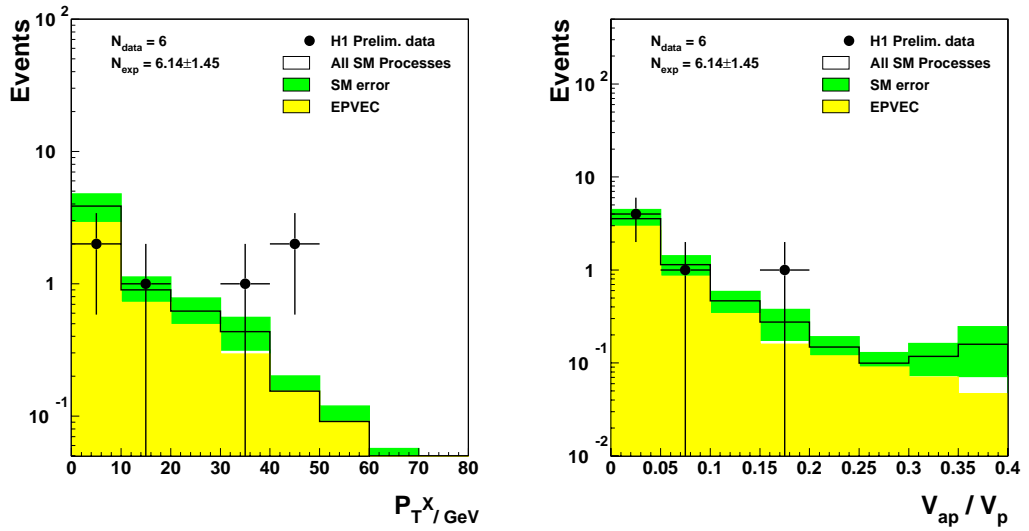


Figure 7.4: The transverse momentum of the hadronic final state,  $P_T^X$  (left), and the azimuthal balance (right) of the final electron selection in the 94-00  $e^+p$  data.



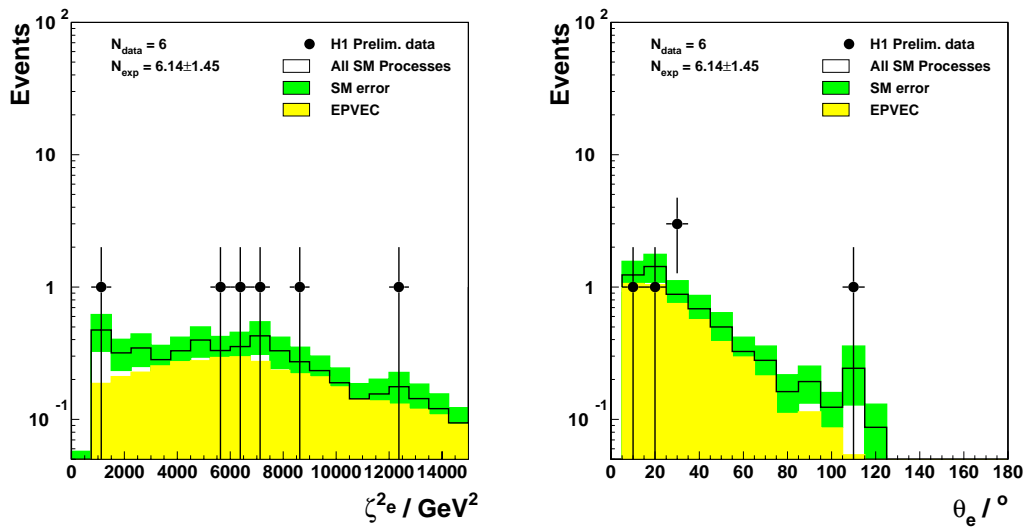


Figure 7.5: The  $\zeta^2(Q^2)$  distribution of the final electron selection in the 94-00  $e^+p$  data.

## The electron-proton data

No candidate  $W \rightarrow e\nu$  data events are observed in this data set, compared to  $1.46 \pm 0.30$  expected. The prediction of the Standard Model is presented in table 8.4.

## 7.2 The Final Selection of the Muon Channel

### 7.2.1 The Cuts

The selection criteria for the muon channel study sample are defined in section 5.7.2. The final event sample is then selected as a subset of the study sample by the following criteria:

- $P_T^\mu > 10$  GeV
- $P_T^{miss} > 12$  GeV
- $D_{track} > 0.5$
- $P_T^X > 12$  GeV
- $\Delta\phi_{\mu-X} > 10^\circ$  for  $\geq 2$  central tracks
- Only one isolated muon

The justification for these cuts has been discussed and presented in sections 6.2.1 to 6.2.5.

## 7.2.2 Distributions of the Final Muon Selection

### The positron-proton data

The distributions of the data and simulation are shown in figures 7.6 to 7.10.

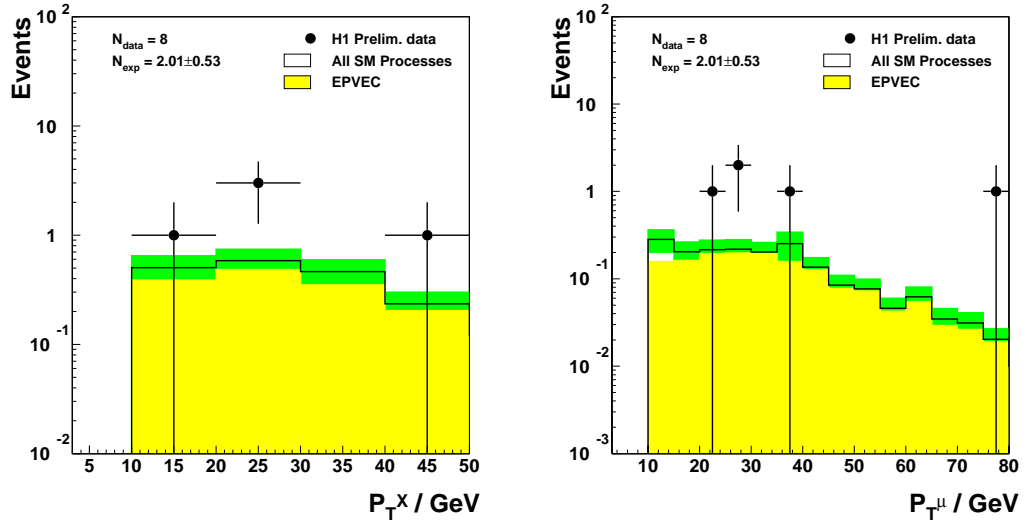


Figure 7.6: The transverse momentum of the hadronic final state,  $P_T^X$  (left), and the transverse momentum of the muon candidate (right) of the final muon selection in the 94-00  $e^+p$  data.

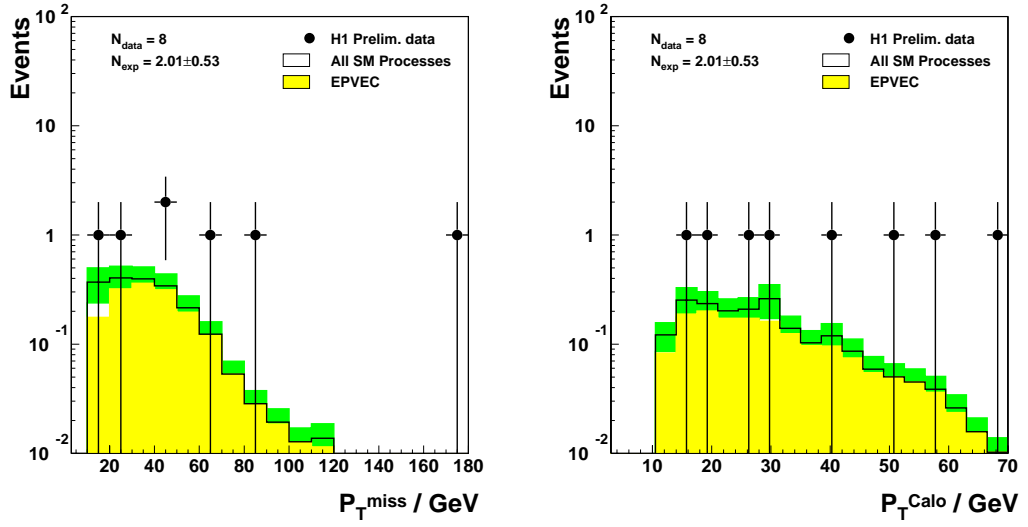


Figure 7.7: The missing transverse momentum,  $P_T^{miss}$  (left), and the missing calorimetric transverse momentum,  $P_T^{calo}$  (right) of the final muon selection in the 94-00  $e^+p$  data.

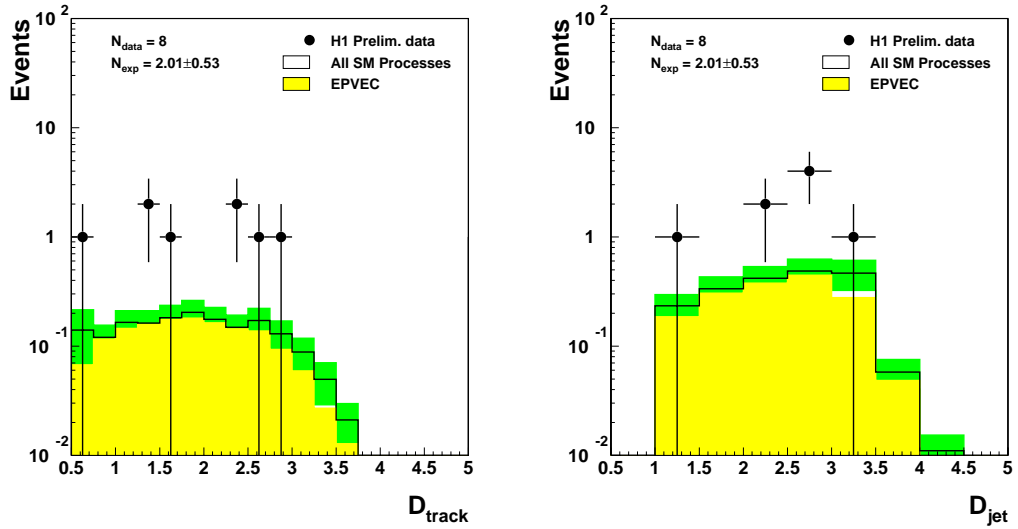


Figure 7.8: The distances  $D_{track}$  (left) and  $D_{jet}$  (right) of the final muon selection in the 94-00  $e^+p$  data.

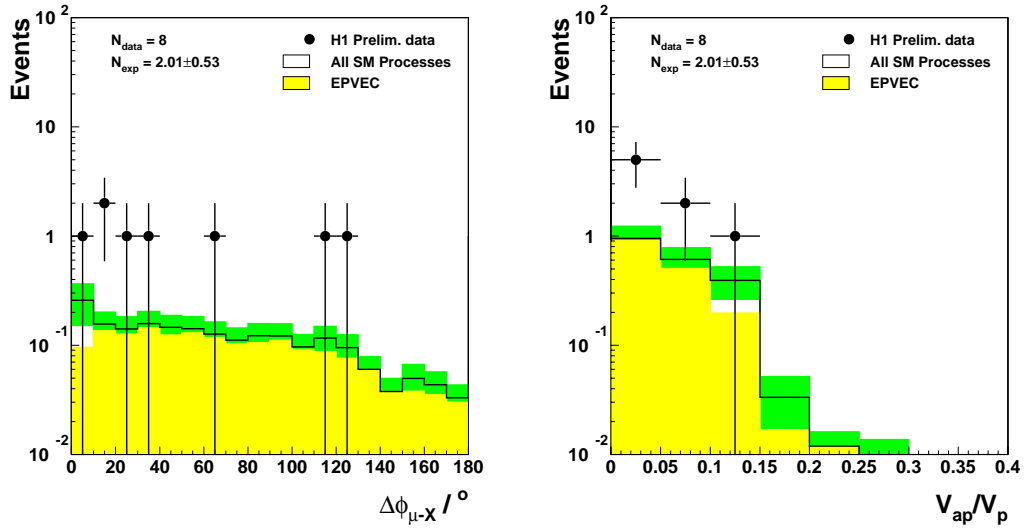


Figure 7.9: The acoplanarity (left), and azimuthal balance (right) of the final muon selection in the 94-00  $e^+p$  data.

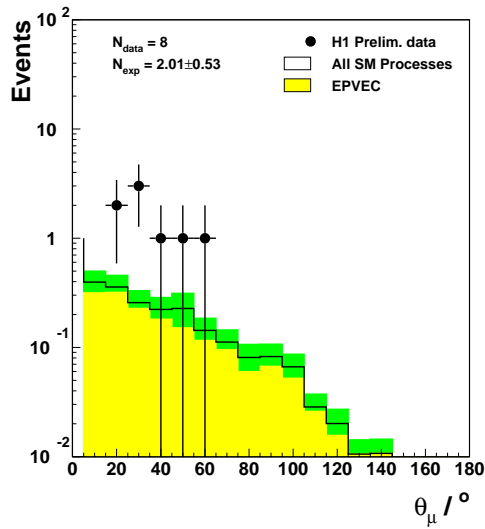


Figure 7.10: The polar angle of the muon candidate (right) of the final muon selection in the 94-00  $e^+p$  data.

## The electron-proton data

No candidate  $W \rightarrow \mu\nu$  data events are observed in this data set, compared to  $0.32 \pm 0.09$  expected. The prediction of the Standard Model is presented in table 8.5.

## 7.3 Selection Efficiencies

The selection efficiencies for the electron and muon channel are shown in figure 7.11 as a function of generated  $P_T^X$ . The electron channel selection efficiency is roughly constant at 40-50%. The muon channel selection efficiency reaches higher values ( $\sim 60\%$ ), but falls off at lower values of  $P_T^X$ . This is due to the  $P_T^{calo}$  cut forcing a cut on  $P_T^X$  as explained in section 6.2.5.

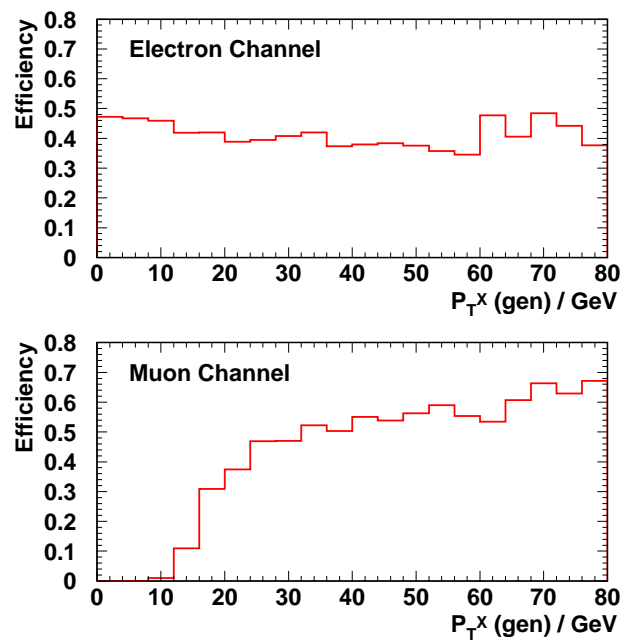


Figure 7.11: The selection efficiency as a function of generated  $P_T^X$  for the electron channel (upper plot) and the muon channel (lower plot) calculated from the EPVEC Monte Carlo.

# Chapter 8

## Final Results and Discussion

### 8.1 Results in the Positron-Proton Data

#### 8.1.1 Tables

Table 8.1 shows the final selection for the process  $W \rightarrow e\nu$ . The results are presented as a function of increasing  $P_T^X$  cut. The Standard Model prediction is given as a sum total, and broken down into its components. It can be seen that the  $W$  production component is the dominant component of the Standard Model prediction. This becomes more marked at higher  $P_T^X$ . Overall, the prediction of the Standard Model agrees well with the observed number of events ( $6.14 \pm 1.46$  *cf.* 6). However, a discrepancy between the two arises at higher  $P_T^X$ .

Of the six candidate events for the process  $W \rightarrow e\nu$ , one is observed to contain an  $e^-$ . Three of the other candidate events contain an  $e^+$ . The charges of the electrons in the remaining two events are unmeasured since the electrons are produced at low polar angles and shower in the passive layers of the FTD.

Table 8.2 shows the final selection for the process  $W \rightarrow \mu\nu$ . The results are



GeV	Data	St. Model	W	NC	CC	LPAIR
$P_T^X > 0$	6	$6.14 \pm 1.46$	$4.72 \pm 1.42$	$0.55 \pm 0.23$	$0.76 \pm 0.25$	$0.12 \pm 0.09$
$P_T^X > 12$	4	$2.06 \pm 0.51$	$1.65 \pm 0.50$	$0.15 \pm 0.10$	$0.23 \pm 0.09$	$0.03 \pm 0.02$
$P_T^X > 25$	3	$1.05 \pm 0.27$	$0.83 \pm 0.25$	$0.11 \pm 0.09$	$0.11 \pm 0.05$	$0.01 \pm 0.01$
$P_T^X > 40$	2	$0.33 \pm 0.10$	$0.31 \pm 0.09$	$0.00 \pm 0.00$	$0.01 \pm 0.01$	$0.00 \pm 0.00$

Table 8.1: Final results for the selection of the process  $W \rightarrow e\nu$ , shown with respect to increasing  $P_T^X$  cuts for the  $81.63 \text{ pb}^{-1}$  of  $e^+p$  data. Given are the total number of data events observed, the total predicted number from the Standard Model simulation, and the breakdown of the Standard Model into its  $W$  (EPVEC), NC (DJANGO+PYTHIA), CC (DJANGO) and  $\gamma\gamma \rightarrow e^+e^-$  (LPAIR) components. Errors given are systematic and statistical combined in quadrature.

presented as a function of increasing  $P_T^X$  cut. The Standard Model prediction is given as a sum total, and broken down into its components. As in the electron channel, it can be seen that the  $W$  production component is the dominant component of the Standard Model prediction, and again this becomes more marked at higher  $P_T^X$ . Across the full measured range of  $P_T^X$ , the number of data events observed exceeds the prediction of the Standard Model. Like in the electron channel, this effect becomes more pronounced at higher  $P_T^X$ .

Five of the candidate events for the process  $W \rightarrow \mu\nu$  contain a  $\mu^+$  and two contain a  $\mu^-$ . The muon in the remaining event has too high a momentum (too stiff a track) for its charge to be determined.

The two electron and muon channels may also be combined. This assumes lepton universality, namely that there is no *a priori* difference between the two decay channels, and that their branching ratios should be the same. This assumption itself is valid within the Standard Model, but it should be noted that the results presented here are not in agreement with the predictions of the Standard Model.

GeV	Data	St. Model	W	NC	CC	LPAIR
$P_T^X > 12$	8	$2.01 \pm 0.54$	$1.65 \pm 0.50$	$0.07 \pm 0.07$	$0.05 \pm 0.03$	$0.25 \pm 0.19$
$P_T^X > 25$	6	$1.21 \pm 0.32$	$1.01 \pm 0.30$	$0.07 \pm 0.07$	$0.04 \pm 0.03$	$0.09 \pm 0.07$
$P_T^X > 40$	4	$0.46 \pm 0.13$	$0.43 \pm 0.13$	$0.00 \pm 0.00$	$0.02 \pm 0.02$	$0.02 \pm 0.02$

Table 8.2: Final results for the selection of the process  $W \rightarrow \mu\nu$ , shown with respect to increasing  $P_T^X$  cuts for the  $81.63 \text{ pb}^{-1}$  of  $e^+p$  data. Given are the total number of data events observed, the total predicted number from the Standard Model simulation, and the breakdown of the Standard Model into its  $W$  (EPVEC), NC (DJANGO+PYTHIA), CC (DJANGO) and  $\gamma\gamma \rightarrow \mu^+\mu^-$  (LPAIR) components. Errors given are systematic and statistical combined in quadrature.

The combined results for the electron and muon decay channels are shown in table 8.3. The Standard Model prediction is shown as a sum total, and split into  $W$  production and other processes combined. It should be noted that only the electron channel contributes for  $P_T^X < 12 \text{ GeV}$  (see section 6.2.5). The number of candidate events observed exceeds the Standard Model prediction throughout. In particular, at  $P_T^X > 40 \text{ GeV}$ , 6 candidate events are observed in comparison to the Standard Model prediction of  $0.79 \pm 0.22$  (dominated by  $W$  production).

GeV	Data	St. Model	W	Other processes
$P_T^X > 0$	14	$8.16 \pm 1.97$	$6.36 \pm 1.91$	$1.80 \pm 0.46$
$P_T^X > 12$	12	$4.07 \pm 1.03$	$3.30 \pm 0.99$	$0.77 \pm 0.27$
$P_T^X > 25$	9	$2.26 \pm 0.57$	$1.83 \pm 0.55$	$0.43 \pm 0.15$
$P_T^X > 40$	6	$0.79 \pm 0.22$	$0.74 \pm 0.22$	$0.05 \pm 0.03$

Table 8.3: Final results for the electron and muon channels combined, shown with respect to increasing  $P_T^X$  cuts for the  $81.63 \text{ pb}^{-1}$  of  $e^+p$  data. Given are the total number of data events observed, the total predicted number from the Standard Model simulation, and the breakdown of the Standard Model into its  $W$  (EPVEC) component and other components combined. Errors given are systematic and statistical combined in quadrature.

## 8.1.2 Event Kinematics

Distributions of the selected events in lepton polar angle, acoplanarity, transverse mass and  $P_T^X$  are shown in figures 8.1 and 8.2. These figures show the combined results presented in table 8.3.

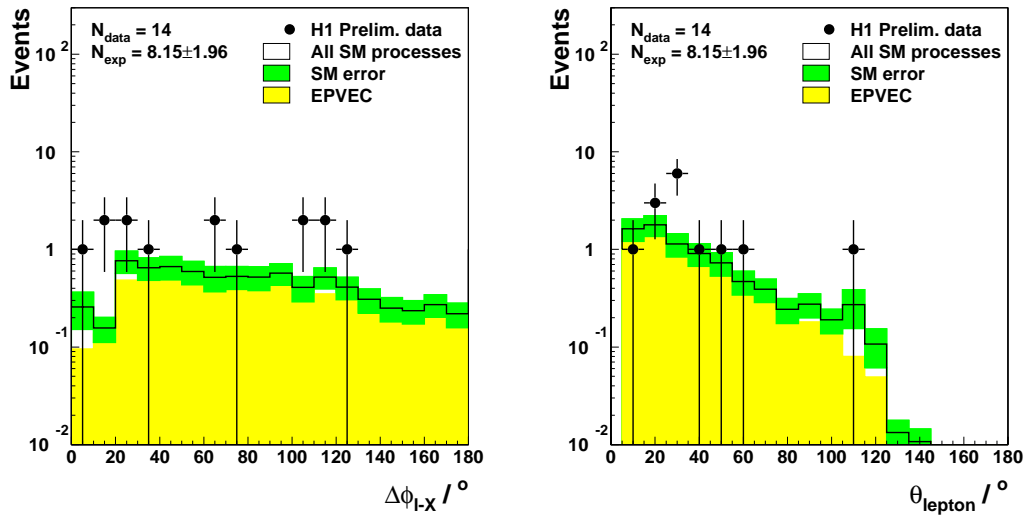


Figure 8.1: The acoplanarity (left) and the polar angle of the lepton (right) of the combined final electron and muon selection in the 94-00  $e^+p$  data.

The events are generally found at low values of lepton polar angle and are evenly distributed in acoplanarity in agreement with the expectation. The reduction in the expectation at low and high acoplanarity is due to the selection cuts.

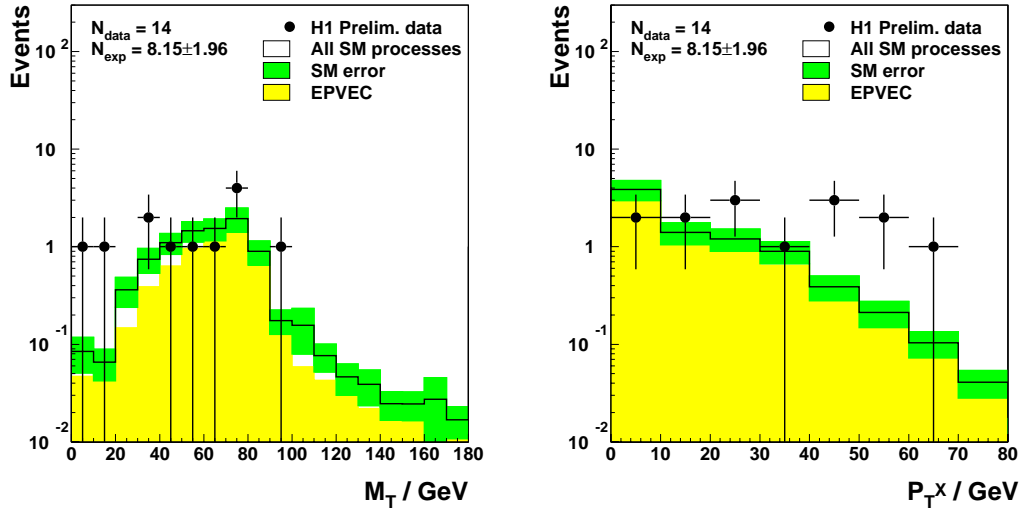


Figure 8.2: The transverse mass (left) and the transverse momentum of the hadronic final state (right) of the combined final electron and muon selection in the 94-00  $e^+p$  data.

The events are distributed in a Jacobian peak associated to the nominal  $W$  mass, as expected from  $W$  production. At  $P_T^X < 25$  GeV there is good agreement between the expectation and the observed events. At higher values of  $P_T^X$  the data lie above the expectation.

The scattered positron is tagged in three of the fourteen events, allowing the lepton-neutrino mass to be reconstructed, under the assumption that there is only one neutrino in the final state and there is no initial state QED radiation. All three events yield masses that are consistent with the  $W$  mass, having values of  $82_{-12}^{+19}$ ,  $71_{-11}^{+10}$  and  $77_{-15}^{+22}$  GeV. From Standard Model  $W$  production it is expected that approximately 25% of events have a scattered positron in the acceptance range of the detector.

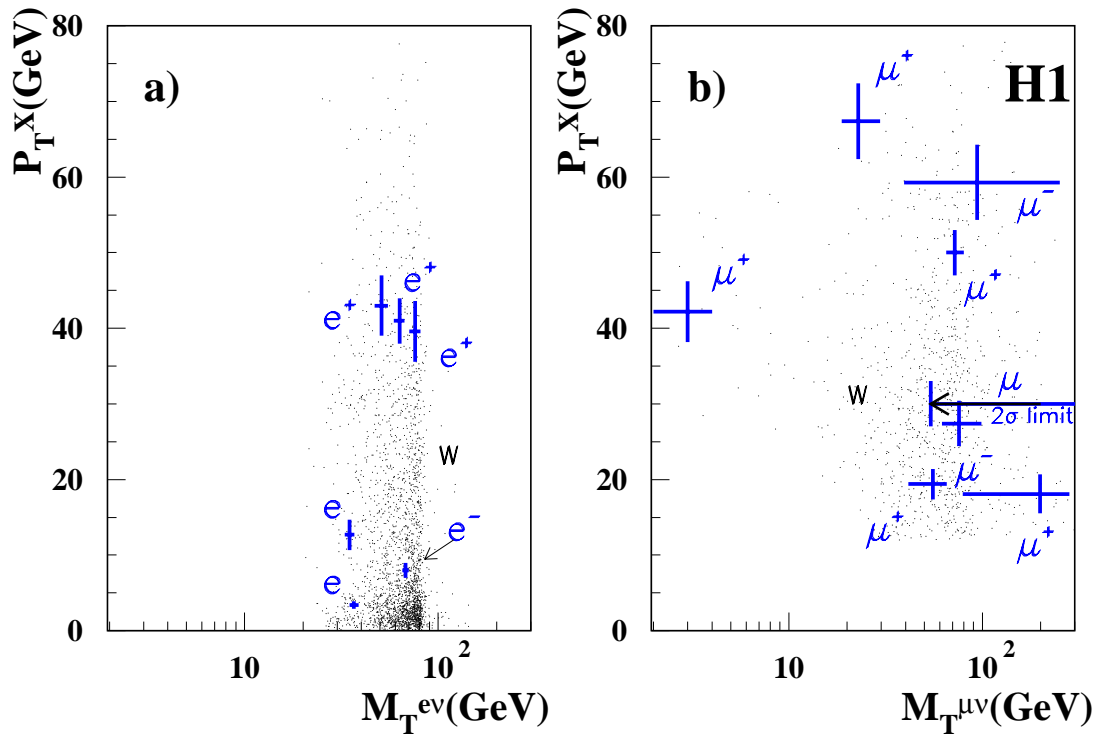


Figure 8.3: The correlation between the transverse momentum of the hadronic final state and the transverse mass of the lepton-neutrino system in the electron (left) and muon (right) decay channels in the 94-00  $e^+p$  data. The smaller dots represent the distribution of Standard Model  $W$  Monte Carlo events with a luminosity 500 times that of the data sample. Taken from [83].

The transverse mass and the transverse momentum of the hadronic system of the selected events are compared to  $W$  production in figure 8.3. It is the occurrence of events with high  $P_T^X$  which is atypical of Standard Model  $W$  production. Note in particular that more of these events have been observed, in both decay channels, since the previous publication (*cf.* figure 5.1).

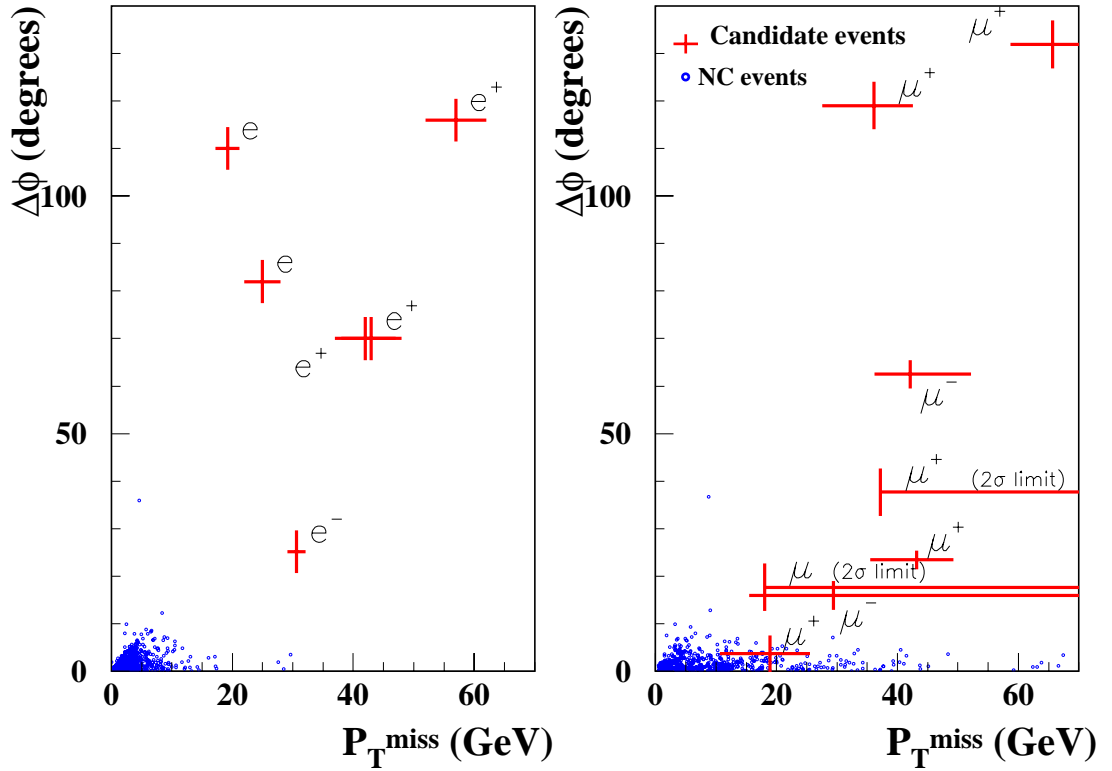


Figure 8.4: A comparison of the final data sample in each decay channel, showing the distribution in  $\Delta\phi_{l-X}$  and  $P_T^{miss}$ . The dots represent the distribution of NC data events. Taken from [83].

The significance of missing transverse momentum and acoplanarity has been studied with data using a sample of NC events having similar transverse momentum and lepton polar angle to the  $W$  candidates selected. The transverse momentum is reconstructed using the calorimetric deposit for comparison with the electron events and using the electron track momentum for comparison with the muon candidates. The deviations from zero in the  $P_T^{miss}$  and acoplanarity plane for NC events quantify the experimental smearing. The distribution of this sample is presented in figure 8.4. This study clearly shows that the observed acoplanarities and missing momenta in the  $W$  candidates are not explained by a measurement error and confirms the

existence of a non-detected particle in those events.

## 8.2 Results in the Electron-Proton Data

### 8.2.1 Tables

GeV	Data	St. Model	W	NC	CC	LPAIR
$P_T^X > 0$	0	$1.46 \pm 0.30$	$0.86 \pm 0.26$	$0.16 \pm 0.07$	$0.43 \pm 0.14$	$0.01 \pm 0.01$
$P_T^X > 12$	0	$0.50 \pm 0.11$	$0.31 \pm 0.09$	$0.06 \pm 0.04$	$0.12 \pm 0.05$	$0.00 \pm 0.00$
$P_T^X > 25$	0	$0.26 \pm 0.06$	$0.16 \pm 0.05$	$0.02 \pm 0.02$	$0.08 \pm 0.04$	$0.00 \pm 0.00$
$P_T^X > 40$	0	$0.12 \pm 0.03$	$0.06 \pm 0.02$	$0.00 \pm 0.00$	$0.06 \pm 0.03$	$0.00 \pm 0.00$

Table 8.4: Final results for the selection of the process  $W \rightarrow e\nu$ , shown with respect to increasing  $P_T^X$  cuts for the  $13.61 \text{ pb}^{-1}$  of  $e^-p$  data. Given are the total number of data events observed, the total predicted number from the Standard Model simulation, and the breakdown of the Standard Model into its  $W$  (EPVEC), NC (DJANGO+PYTHIA), CC (DJANGO) and  $\gamma\gamma \rightarrow e^+e^-$  (LPAIR) components. Errors given are systematic and statistical combined in quadrature.

The lack of observed candidate  $W \rightarrow e\nu$  events in this data set is in agreement with the prediction of the Standard Model. It is also in agreement with the observed number of events in the positron-proton data set, for the luminosity of the  $e^-p$  data is 6 times smaller than that of the  $e^+p$  data set.



GeV	Data	St. Model	W	NC	CC	LPAIR
$P_T^X > 12$	0	$0.32 \pm 0.09$	$0.28 \pm 0.08$	$0.00 \pm 0.00$	$0.00 \pm 0.00$	$0.04 \pm 0.03$
$P_T^X > 25$	0	$0.19 \pm 0.06$	$0.18 \pm 0.05$	$0.00 \pm 0.00$	$0.00 \pm 0.00$	$0.02 \pm 0.01$
$P_T^X > 40$	0	$0.08 \pm 0.02$	$0.08 \pm 0.02$	$0.00 \pm 0.00$	$0.00 \pm 0.00$	$0.00 \pm 0.00$

Table 8.5: Final results for the selection of the process  $W \rightarrow \mu\nu$ , shown with respect to increasing  $P_T^X$  cuts for the  $13.61 \text{ pb}^{-1}$  of  $e^-p$  data. Given are the total number of data events observed, the total predicted number from the Standard Model simulation, and the breakdown of the Standard Model into its  $W$  (EPVEC), NC (DJANGO+PYTHIA), CC (DJANGO) and  $\gamma\gamma \rightarrow e^+e^-$  (LPAIR) components. Errors given are systematic and statistical combined in quadrature.

Again, the lack of observed candidate  $W \rightarrow \mu\nu$  events in this data set is in agreement with the prediction of the Standard Model. Comparing to the observed number of events in the positron-proton data set, one might expect an event at low  $P_T^X$ , but one cannot draw significant conclusions from such small data sets.

## 8.3 Discussion

All the results presented in 8.1 and 8.2 have been approved [82] by the H1 collaboration as being *preliminary*, and have been presented outside the collaboration [83].

At high  $P_T^X$  the event rates in both electron and muon channels represent a significant deviation from the prediction of the Standard Model, albeit in event samples with limited statistics. Combined, the two channels exceed the Standard Model prediction over the full measured range of  $P_T^X$ . The analysis presented in this thesis has developed from the observation of events by H1 of events with topologies characteristic of real  $W$  decay, but with some unusual kinematic properties [37, 69]. Of particular interest is the fact that equally spectacular events have been observed in the data samples recorded since those publications. Moreover, in the original publications it was only the muon events that were considered to be of particular note (see figure 5.1), yet in the most recent  $e^+p$  data (1999-2000), events have been observed at high  $P_T^X$  in the electron channel as well as the muon channel (compare figure 5.1 to figure 8.3).

The events observed at high  $P_T^X$  (9 at  $P_T^X > 25$  GeV and 6 at  $P_T^X > 40$  GeV) are in a region of phase space very lightly populated by the Standard Model. Not only are  $W$  events predicted to be rare in this kinematic range, but other Standard Model processes are even rarer. For example, at  $P_T^X > 25$  GeV the Standard Model predicts  $1.83 \pm 0.55$   $W$  events and only  $0.43 \pm 0.15$  events from other processes. Careful studies have been made of the background processes, and their contributions are quoted with very conservative errors.

Muon pair events (LPAIR) are the main background in the muon channel (the channel showing the greatest deviation from the expectation). The contribution from this kind of event is studied in section 6.5, and is quoted with a systematic error of 75%. With reference to figures 6.20 and 6.21 this quoted error can be seen to be ample to describe the agreement between the data and the simulation,

yet this error is plainly insufficient to cover the discrepancy between that data and simulation at high  $P_T^X$  in the final muon channel sample.

Equivalently, CC events (DJANGO-CC) are the main background in the electron channel. A study of these kind of events has also been carried out and is presented in section 6.4. The contribution to the expectation from this Monte Carlo is quoted with a systematic error of 30%, which can be seen in figures 6.18 and 6.19 to be a reasonable estimate of the discrepancy between the data sample and the simulation. Nevertheless, once in the the region of  $P_T^X > 25$  GeV and beyond, the contribution to the final sample from CC events becomes such a small proportion of the total, that even wildly larger systematic errors would not be sufficient to explain the discrepancy between data and simulation.

Possible explanations for these results fall into four main categories: statistical, systematic, within the Standard Model and beyond the Standard Model.

A statistical fluctuation remains the “safe” interpretation of these events. When the events from the 1994-1997  $e^+p$  data set were first published, their discussion was based on this explanation, although it was stated that “the kinematic properties [of the events] disfavour an interpretation of these events within the Standard Model processes considered”. This explanation remains a possibility, but with the addition of subsequent “unusual” events in the more recent data it looks weaker than ever. Nevertheless it should also be noted that ZEUS have performed a search for events with missing transverse momentum and an isolated high  $P_T$  lepton, and observe no excess of events at high  $P_T^X$ . A more detailed comparison to ZEUS can be seen in appendix B.

Systematic uncertainties may be split into two parts; experimental and theoretical. The theoretical part is dealt with shortly. Experimental systematic errors are essentially measurement errors. It is possible for the final state particles of an event not originating from a  $W$  to be mis-identified as such in the detector. Investigation

of this source of error makes it an improbable explanation for the observed excess. For example, the very small likelihood of NC data events being misidentified as  $W$  can be appreciated from figure 8.4. Another possibility is the misidentification of an isolated charged hadron as a muon, if the former were to penetrate unusually far beyond the hadronic part of the calorimeters and into the instrumented iron. Previous studies [37] have estimated the probability of this (for a momentum range typical of the muon candidates) to be  $< 3 \cdot 10^{-3}$ .

Theoretical systematic uncertainties are dealt with as possibilities within the Standard Model. Each of the Monte Carlo simulations has a systematic uncertainty associated with it. The largest of these (the LPAIR systematic uncertainty in the muon channel (75%) and the DJANGO-CC uncertainty in the electron channel (30%)) have been presented earlier in this chapter. The theoretical errors on these calculations arise predominantly from PDF and scale uncertainties. As previously discussed however, these do not come close to explaining the discrepancy between data and simulation. A further source of theoretical error arises in the calculation of the  $W$  production cross section in the EPVEC Monte Carlo. At present, this calculation is only performed to leading order in QCD. The most reliable contemporary calculations [84] estimate that extending these calculations to next-to-leading order will increase the total  $W$  cross section by less than 10%. Nevertheless, this represents the largest potential error yet presented, and as such the most likely explanation so far.

Moving into theoretical regions on the edge of the Standard Model, work has been done [85] to assess the possibility that events like the ones presented in this thesis might arise from anomalous triple boson couplings (TBCs) (see section 3.6). As shown in figure 8.5 a significant distortion of the  $P_T^X$  spectrum is possible, by a suitable choice of  $\Delta\kappa_\gamma$  and  $\lambda_\gamma$ . However such extreme choices of these parameters are in great contradiction to the latest precision TBC measurements [86], which measure  $\kappa_\gamma = 0.97_{-0.16}^{+0.20}$  and  $\lambda_\gamma = -0.110_{-0.055}^{+0.058}$ , and hence this seems an unlikely

source of explanation.

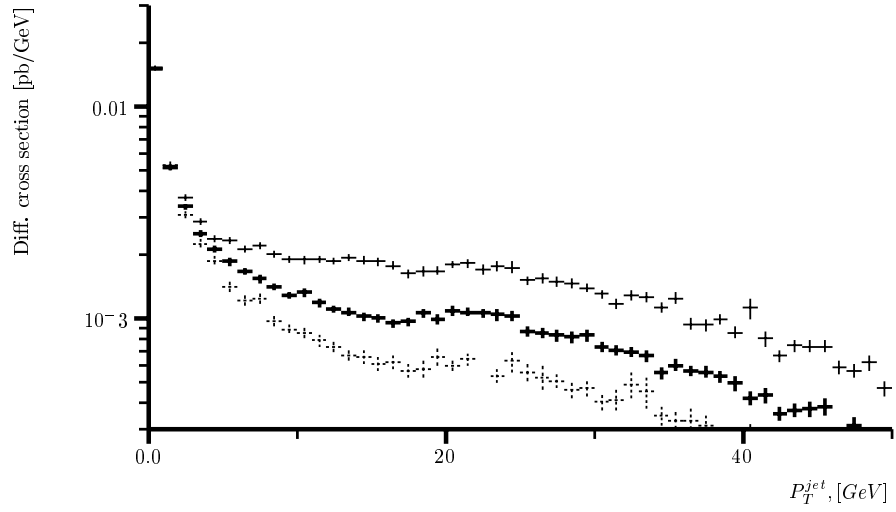


Figure 8.5: Calculation of the distribution of jet transverse momentum ( $P_T^{jet} = P_T^X$ ) in the reaction  $e^-p \rightarrow e^- \mu^+ \nu_\mu X$ . Bold crosses - standard case, dashed crosses -  $\lambda_\gamma = 0$ ,  $\kappa_\gamma = 0$ , thin crosses -  $\lambda_\gamma = 0$ ,  $\kappa_\gamma = 2$ . ( $E_\mu \geq 10$  GeV,  $P_T^{miss} \geq 20$  GeV). Taken from [85].

As discussed in section 3.7, the most stringent limits currently set on the FCNC vertex  $\kappa_\gamma^{FCNC}$  have been provided by the CDF collaboration [46] from their study of the process  $t \rightarrow u\gamma$ . The calculated [47] upper limit on  $\kappa_\gamma^{FCNC}$  of 0.28 is sufficient to allow a few single top events in the data sample presented here. Given that the most competitive modern results do not exclude this process, this must be seen as the most likely candidate explanation. Further discussion of this possibility can be found in [87].

There then remain intriguing possibilities beyond the Standard Model. Explanations such as excited fermion or leptoquark production are disfavoured by the observed acoplanarity of the events (see figure 8.1). The final state fermion and hadronic jet from these processes are expected to be produced in a back-to-back configuration ( $\Delta\phi_{l-X} = 0^\circ$ ). The distribution of the final event sample in  $\Delta\phi_{l-X}$  (figure 8.1) is not conducive to these interpretations.

There then remains the possibility of these events being the observation of the decay products of supersymmetric particles, although direct searches for such events by H1 [88] have excluded squark masses below 258 GeV<sup>1</sup> at the 95% confidence level independently of the values of the MSSM parameters. Thus, for the events presented in this thesis to fit into a scenario of this nature, a considerably different version of the MSSM would have to be proposed.

---

<sup>1</sup>For a Yukawa coupling of the electromagnetic strength.

# Chapter 9

## Summary

In  $81.63 \text{ pb}^{-1}$  of  $e^+p$  data, 14 candidate events are observed for the electronic or muonic decays of a  $W$  boson. The overall rate of events for the electron decay channel is in agreement with the prediction of the Standard Model (6 *cf.*  $6.14 \pm 1.46$ ). In the muon channel the rate of events exceeds the expectation across the full kinematic range (8 *cf.*  $2.01 \pm 0.54$ ). Combining the two decay channels 14 events are observed compared to an expectation of  $8.16 \pm 1.97$ . The discrepancy between the data and the simulation is seen to grow with increasing  $P_T^X$ . For  $P_T^X > 25 \text{ GeV}$ , 9 candidate events are observed, compared to an expectation of  $2.26 \pm 0.57$ .

In  $13.61 \text{ pb}^{-1}$  of  $e^-p$  data, no candidate events are observed, consistent with the expectation for this small data set.

The origin of these events, in particular those at high  $P_T^X$ , remains unclear. Whilst the events themselves have topologies broadly consistent with the electronic or muonic decay of a Standard Model  $W$  boson, their distribution in  $P_T^X$ , the transverse momentum of the hadronic final state, and their overall rate, do not favour an interpretation within the framework of the Standard Model.

Interpreted as evidence for contemporary models of physics beyond the Standard

Model, the production of single top quarks via the FCNC  $t\bar{u}\gamma$  vertex is the most compatible explanation, given contemporary limits on this vertex.

At present both HERA and H1 are undergoing an upgrade programme, scheduled to come online again at the end of Summer 2001. ZEUS is also upgrading. The higher luminosities expected after the upgrade will provide the larger data sets needed to establish whether the results presented in this thesis are a rather large statistical fluctuation, or the first evidence of new physics at HERA.



# Bibliography

- [1] H1 Collaboration; I. Abt et al., *The H1 Detector at HERA*, NIM. **A386** (1997) 310-396.
- [2] H1 Calorimeter Group; B. Andrieu et al., *The H1 Liquid Argon Calorimeter System*, NIM. **A336** (1993) 460.
- [3] H. Wellisch, J. Kubenka, H. Oberlack and P. Schacht, *Hadronic Calibration of the H1 LAr Calorimeter using Software weighting Techniques*, H1 Internal Note, **94-346**.
- [4] H1 SPACAL Group; R.D. Appuhn et al., *The H1 Lead/Scintillating Fiber Calorimeter*, NIM. **A386** (1997) 397-408.
- [5] H1 Collaboration, *Performance of an electromagnetic Lead/Scintillating Fiber Calorimeter for the H1 Detector*, NIM. **A374** (1996) 149-156.
- [6] H1 SPACAL Group, *Hadronic response and  $e/\pi$ -Separation with the H1 lead/fiber Calorimeter*, DESY **95-250**.
- [7] Tim Nicholls, *A Measurement of the Diffractive Proton Structure Function at HERA*, Ph.D. thesis, University of Birmingham, April 1997.
- [8] J. Ebert, *The H1-Tail Catcher Hardware and Software Performance*, H1 Internal Note **95-448**.

- [9] W. Hildesheim et al., *The Plug Calorimeter Users Guide*, H1 Internal Note **94-372**.
- [10] J. Tutas, *A Level 1 Trigger from the Limited Streamer Tube system*, H1 Internal Note **91-185**;  
H. Itterbeck et al., *Improvement of the Trigger Timing of the H1 Digital Muon System*, H1 Internal Note **95-427**.
- [11] H1 Collaboration, *The H1 Forward Muon Spectrometer*, NIM. **A340** (1994) 304-308.
- [12] J. Heatherington et al., *Studies on TOF FTDC data*, H1 Internal Note **93-307**;  
J. Heatherington et al., *Analysis of TOF FTDC data*, H1 Internal Note **94-362**.
- [13] H. Bethe, W. Heitler, *On the stopping of fast particles and on the creation of positive electrons*, Proc. Roy. Soc. Lond. **A146**.
- [14] H1 Collaboration, *Luminosity Measurement in the H1 Experiment at HERA*, contributed paper pa17-026 to ICHEP 1996, Warsaw.
- [15] E. Elsen, *The H1 Trigger and Data Acquisition*, Proc. of the “International Symposium on Electronic Instrumentation in Physics”, Dubna, May 1991, H1 Internal Note **93-262**;  
F. Sefkow et al., *Experience with the First Level trigger of H1*, Proc. of the 1994 IEEE Nuclear Science Symposium, Norfolk, Virginia. H1 Internal Note **94-407**.
- [16] J.C. Bizot et al., *Status of Simulation for a Topological Level 2 Trigger*, H1 Internal Note **92-212**;  
J.C. Bizot et al., *Strategy Studies for the H1 Topological L2-Trigger (L2TT)*, H1 Internal Note **97-508**.

- [17] J.H. Köhne et al., *Realization of a Second Level Neural Network Trigger for the H1 experiment at HERA*, H1 Internal Note **97-509**.
- [18] B. Heinemann, Dissertation - *Measurement of Charged Current and Neutral Current Cross Sections in Positron-Proton Collisions at  $\sqrt{s} \simeq 300\text{GeV}$*  - Fachbereich Physik der Universität Hamburg.
- [19] H1 Collaboration; C. Adloff et al., *Measurement of Neutral and Charged Current cross-sections in positron proton collisions at large momentum transfer*, Eur. Phys. J. **C13** (2000) 609-639. **hep-ex/9908059**.
- [20] A. Schöning, *Untersuchung von Prozessen mit virtuellen und reellen  $W^\pm$ -Bosonen am H1-Detektor bei HERA*, Ph.D. Thesis, II. Inst. Exp. Phys., Univ. Hamburg, 1996.
- [21] F. Keil, Ph.D. Thesis, Kirchhoff-Institut für Physik, Univ. Heidelberg, *in preparation*.
- [22] F. James, *MINUIT - Function minimization and Error analysis - reference manual*, Version 94.1, CERN D506, CERN, August 1998.
- [23] R. Feynman, *Very high-energy collisions of hadrons*, Phys. Rev. Lett. **23** (1969) 1415-1417;  
J. Bjorken, E. Paschos, *Inelastic electron proton and gamma proton scattering, and the structure of the nucleon*, Phys. Rev. **185** (1969) 1975-1982.
- [24] C. Callan, D. Gross, Phys. Rev. Lett. **21** (1968) 311.
- [25] C. Callan, D. Gross, *High-Energy electroproduction and the constitution of the electric current*, Phys. Rev. Lett. **22** (1969) 156-159.
- [26] M. Klein, *Structure Functions in Deep Inelastic Lepton-Nucleon Scattering*, Proc. of the Lepton-Photon Symposium, Stanford, August 1999. **hep-ex/0001059**.

- [27] E.D. Bloom et al., *Observed Behavior of highly inelastic electron - proton scattering*, Phys. Rev. Lett. **23** (1969) 935-939.
- [28] NMC Collaboration, *Proton and Deuteron  $F_2$  structure functions in deep inelastic muon scattering*, Phys. Lett. **B295** (1992) 159-168;  
NMC Collaboration; M. Arneodo et al., Phys. Lett. **B364** (1995) 107.
- [29] BCDMS Collaboration, *Test of QCD and a measurement of  $\lambda$  from scaling violations in the proton structure function  $F_2(x, Q^2)$  at high  $Q^2$* , Phys. Lett. **B223** (1989) 485.
- [30] J. Bjorken, *Inequality for backward electron-nucleon and muon-nucleon scattering at high momentum transfer*, Phys. Rev. **163** (1967) 1767-1769.
- [31] H1 Collaboration; C. Adloff et al., *Multi-Jet Event Rates in Deep-Inelastic Scattering and Determination of the Strong Coupling Constant*, Eur. Phys. J. **C6** (1999) 575-585.
- [32] F. Wilczek, *QCD Made Simple*, Physics Today, August 2000, pp 22-28.
- [33] T. Morris, *An Introduction to QED and QCD*, Proc. of the School for Young High Energy Physicists, RAL Technical Report (1999) 024.
- [34] F. Mandl and G. Shaw, *Quantum Field Theory*, McGraw-Hill 1964;  
M. E. Peskin and D. V. Schroeder, *An Introduction to Quantum Field Theory*, Addison Wesley 1995;  
L. H. Ryder, *Quantum Field Theory*, Cambridge University Press 1985.
- [35] M.H. Seymour, *Jets in QCD*. **hep-ph/9506421** and references therein.
- [36] H1 Collaboration; C. Adloff et al., *Measurement of Di-jet Cross-Sections in Photoproduction and Photon Structure*, Phys. Lett. **B483** (2000) 36-48.

- [37] H1 Collaboration; C. Adloff et al., *Observation of Events with an Isolated High Energy Lepton and Missing Transverse Momentum at HERA*, Eur. Phys. J. **C5** (1998) 575-584.
- [38] U. Baur, J. A. M. Vermaseren and D. Zeppenfeld, *Electroweak Vector Boson Production in High Energy ep Collisions*, Nucl. Phys. **B375** (1992) 3-44.
- [39] H1 Collaboration, *W production in  $e^\pm p$  collisions at HERA*, prepared for the XIX International Symposium on Lepton and Photon Interactions at High Energies, Stanford University, August 9-14, 1999.
- [40] H. Aihara et al., *Anomalous Gauge Boson Interactions*, Summary of the DPF Working Subgroup on Anomalous Gauge Boson Interactions of the DPF Long Range Planning Study. **hep-ph/9503425**.
- [41] K. Hagiwara, K. Hikasa, R.D. Peccei and D. Zeppenfeld, *Probing the Weak Boson Sector in  $e^+e^- \rightarrow W^+W^-$* , Nucl. Phys. **B282** (1987) 253;  
K. Gaemers and G. Gounaris, *Polarization Amplitudes for  $e^+e^- \rightarrow W^+W^-$  and  $e^+e^- \rightarrow ZZ$* , Z. Phys. **C1** (1979) 259.
- [42] D. Atwood, L. Reina and A. Soni, *Probing Flavor Changing Top - Charm - Scalar Interactions in  $e^+e^-$  collisions*, Phys. Rev. **D53** (1996) 1199-1201. **hep-ph/9506243**.
- [43] G.M. de Divitiis, R. Petronzio and L. Silvestrini, *Flavor Changing Top Decays in Supersymmetric extensions of the Standard Model*, Nucl. Phys. **B504** (1997) 45-60. **hep-ph/9704244**.
- [44] R.D. Peccei and X. Zhang, *Dynamical Symmetry Breaking and Universality Breakdown*, Nucl.Phys. **B337** (1990) 269-283.
- [45] H. Fritzsch and D. Holtmannspötter, *The Production of Single t quarks at LEP and HERA*, Phys.Lett. **B457** (1999) 186-192. **hep-ph/9901411**.

- [46] CDF Collaboration; F. Abe et al., *Search for Flavor Changing Neutral Current Decays of the Top Quark in  $p\bar{p}$  Collisions at  $\sqrt{s} = 1.8$  TeV*, Phys.Rev.Lett. **80** (1998) 2525-2530.
- [47] T. Han and J.L. Hewett, *Top Charm associated production in high energy  $e^+e^-$  collisions*, Phys.Rev. **D60** (1999) 074015. [hep-ph/9811237](#).
- [48] H1 Collaboration; C. Adloff et al., *Search for compositeness, leptoquarks and large extra dimensions in eq contact interactions at HERA*, Phys. Lett. **B479** (2000) 358-370;  
H1 Collaboration; C. Adloff et al., *A search for leptoquark bosons and lepton flavor violation in  $e^+p$  collisions at HERA*, Eur. Phys. J. **C11** (1999) 447-471.
- [49] ZEUS Collaboration; J. Breitweg et al., *Search for resonances decaying to  $e^+$ -jet in  $e^+p$  interactions at HERA*, Eur. Phys. J. **C16** (2000) 2, 253-267;  
ZEUS Collaboration; M.Derrick et al., *Search for leptoquarks with the ZEUS detector*, Phys. Lett. **B306** (1993) 173-186.
- [50] D.E. Acosta and S.K. Blessing, *Leptoquark searches at HERA and the Tevatron*, Ann. Rev. Nucl. Part. Sci. **49** (1999) 389-434;  
Z. Kunszt and W.J. Stirling, *QCD Corrections and the Leptoquark interpretation of the HERA high  $Q^2$  events*, Z. Phys. **C75** (1997) 453-463. [hep-ph/9703427](#);  
J. Kalinowski, R. Ruckl, H. Spiesberger and P.M. Zerwas, *Leptoquark / Squark Interpretation of HERA events : Virtual effects in  $e^+e^-$  annihilation to hadrons*, Z. Phys. **C74** (1997) 595-603. [hep-ph/9703288](#).
- [51] R. Kerger, *Lepton Flavor Violation at HERA*, Contributed to the 8th International Workshop on Deep Inelastic Scattering and QCD (DIS 2000), Liverpool, England, 25-30 Apr 2000. [hep-ex/0006023](#).
- [52] H1 Collaboration; C. Adloff et al., *A Search for Excited Fermions at HERA*. DESY-00-102, Jul 2000. Accepted by Eur. Phys. J. **C**. [hep-ex/0007035](#);

- ZEUS Collaboration; J. Breitweg et al., *A Search for Excited Fermions in  $e^+p$  collisions at HERA*, Z. Phys. **C76** (1997) 631-646. [hep-ex/9708007](#).
- [53] K. Hagiwara, D. Zeppenfeld and S. Komamiya, *Excited Lepton Production at LEP and HERA*, Z. Phys. **C29** (1985) 115.
- [54] T. Sjöstrand, M. Bengtsson, *The Lund Monte Carlo for Jet Fragmentation and  $e^+e^-$  physics: JETSET 6.2*, Comp. Phys. Comm. **39** (1985) 347-407;  
T. Sjöstrand, M. Bengtsson, *The Lund Monte Carlo for Jet Fragmentation and  $e^+e^-$  physics: JETSET 6.3 : An Update*, Comp. Phys. Comm. **43** (1987) 367.
- [55] R. Brun et al., *GEANT3 User's Guide*, CERN-DD/EE-84-1 (1987).
- [56] C. Diaconu et al., *H1EPVEC -  $W^\pm$  and Z production Monte Carlo generator based on EPVEC*, 09/1999, CPPM, Marseille, France.
- [57] T. Sjöstrand, *High Energy Event Generation with PYTHIA 5.7 and JETSET 7.4*, Comput. Phys. Commun. **82** (1994) 74-90.
- [58] U. Baur and D. Zeppenfeld, *Measuring the  $WW\gamma$  vertex in single W production at ep colliders*, Nucl. Phys. **B325** (1989) 253.
- [59] C.F. von Weizsäcker, *Radiation emitted in collisions of very fast electrons*, Z. Phys. **88** (1934) 612-625.
- [60] E.J. Williams, *Nature of the high-energy particles of penetrating radiation and status of ionization and radiation formulae*, Phys. Rev. **45** (1934) 729-730.
- [61] H. Abramowicz, K. Charchula and A. Levy, *Parameterization of parton distributions in the photon*, Phys. Lett. **B269** (1991) 458-464.
- [62] H. Plothow-Besch, *PDFLIB: A library of all available parton density functions of the nucleon, the pion and the photon and the corresponding  $\alpha_s$  calculations*, Comput. Phys. Commun. **75** (1993) 396-416.

- [63] D. Waters, *A First Estimate of  $\sigma(e^+p \rightarrow e^+W^\pm X)$  and Studies of High  $p_T$  Leptons with the ZEUS Detector at HERA*, Ph.D. Thesis, Wolfson College, University of Oxford, Hilary Term 1998.
- [64] C. Diaconu, CPPM Marseille, France. *Private communication*.
- [65] C. Diaconu, *Monte Carlo Generators for HERA Physics*, Proc. of the workshop 1998/1999, DESY-PROC-1999-02, p.631.
- [66] G.A. Schuler and H. Spiesberger, *DJANGO: The Interface for the Event Generators HERACLES and LEPTO*, Proc. of the Workshop *Physics at HERA*, vol. 3\* 1419-1432, DESY, Hamburg, 1991.
- [67] G. Ingelman, J. Rathsman and G.A. Schuler, *AROMA 2.2: A Monte Carlo Generator for Heavy Flavor Events in ep collisions*, Comput. Phys. Commun. **101** (1997) 135-142. [hep-ph/9605285](#).
- [68] S. Baranov et al., *LPAIR: A Generator for Lepton Pair Production*, Proc. of the Workshop *Physics at HERA*, vol. 3\* 1478-1482, W. Buchmüller and G. Ingelman (Editors), October 1991, DESY, Hamburg;  
J.A.M. Vermaseren, *Two Photon Processes at very High Energies*, NIKHEF-H/82-15, Jul 1982, Nucl. Phys. **B229** (1983) 347.
- [69] H1 Collaboration; T. Ahmed et al., *Observation of an  $e^+p \rightarrow \mu^+ X$  Event with High Transverse Momenta at HERA*, pre-print DESY-94-248, 1994.
- [70] T. Kon, T. Kobayashi and S. Kitamura, *Is a high  $P_T$  muon of the  $e^+p \rightarrow \mu^+ X$  event observed at HERA a signature of the stop?*, Phys. Lett. **B376** (1996) 227-231. [hep-ph/9601338](#).
- [71] H1 Collaboration; S. Aid et al., *Measurement of the  $Q^2$  dependence of the charged and neutral current cross-sections in  $e^\pm p$  scattering at HERA*, Phys. Lett. **B379** (196) 319-329. [hep-ex/9603009](#);



- H1 Collaboration; S. Aid et al., *Measurement of the  $e^+$  and  $e^-$  induced charged current cross sections at HERA*, Z. Phys. **C67** (1995) 565. [hep-ex/9506002](#).
- [72] S.D. Ellis and D.E. Soper, *Successive combination jet algorithm for hadron collisions*, Phys. Rev. **D48** (1993) 3160-3166. [hep-ph/9305266](#).
- [73] S. Catani et al., *Longitudinally invariant  $k(T)$  clustering algorithms for hadron-hadron collisions*, Nucl. Phys. **B406** (1993) 187-224.
- [74] H1PHAN manual, version 2.03/11, 1997.
- [75] H1REC manual, version 9.02/00, 1999.
- [76] S. Bentvelsen et al., Proc. of the Workshop “Physics at HERA”, vol. 1, eds. W.Buchmüller, G. Ingelman, DESY (1992) 23.
- [77] U. Bassler and G. Bernardi, *Some properties of the very high  $Q^2$  events of HERA*, Z. Phys. **C76** (1997) 223-230. [hep-ex/9707024](#).
- [78] A. Mehta, *Measurement of the Diffractive Proton structure function and calibration of the forward muon detector at H1*, Ph. D. Thesis, University of Manchester, December 1994.
- [79] I. Negri et al., *A Minimal Comprehensive Set of Muon Background Topological Finders for High  $P_T$  Physics Analysis*, H1 Internal Note : H1-IN-498(10/1996).
- [80] E. Chabert et al., *QBGFMAR: An Updated Phan Package for Cosmic and Halo Muon Topological Rejection in High  $P_T$  Physics Analysis*, H1 Internal Note : H1-IN-556(11/1998).
- [81] D. Dau, *Private Communication*, July 2000.
- [82] N. Malden, A. Mehta, C. Diaconu, *W analysis presentation*, H1 Plenary Meeting, July 2000.

- [83] H1 Collaboration, *W production in ep collisions at HERA*, submitted to the XXXth International Conference on High-Energy Physics, Osaka, Japan, July 2000, Abstract 974.
- [84] M. Spira, *W Boson Production at NLO*, contributed to the Workshop “Monte Carlo Generators for HERA Physics”, DESY, 1998/1999. **hep-ph/9905469**.
- [85] M.N. Dubinin and H.S. Song, *Anomalous W boson production at HERA*, Phys. Rev. **D57** (1998) 2927-2939. **hep-ph/9708259**.
- [86] OPAL Collaboration, *Measurement of triple gauge boson couplings from WW production at LEP energies up to 189 GeV*, submitted to Eur. Phys. J. C, CERN-EP-2000-114. **hep-ex/0009022**.
- [87] H1 Collaboration, *Search for Single top Production in  $e^\pm p$  collisions at HERA*, submitted to the XXXth International Conference on High-Energy Physics, Osaka, Japan, July 2000, Abstract 961.
- [88] H1 Collaboration, *A Search for Squarks of R-Parity Violating SUSY at HERA*, Conf. Paper 580, 29th International Conference on High-Energy Physics, Vancouver, Canada (1998), July 1998.  
L. Stanco, *A Search for Squarks of R-Parity Violating SUSY at HERA*, talk presented at ICHEP 2000, July 2000.
- [89] ZEUS Collaboration; J. Breitweg et al., *W Production and the Search for Events with an Isolated High-Energy Lepton and Missing Transverse Momentum at HERA*, Phys. Lett. **B471** (2000) 411-428. **hep-ex/9907023**.
- [90] ZEUS Collaboration; J. Breitweg et al., *Search for events with isolated high-energy leptons and missing transverse momentum at HERA*, submitted to the XXXth International Conference on High-Energy Physics, Osaka, Japan, July 2000, Abstract 1041.

# Appendix A

## Event Displays

The 14 events presented in this thesis are illustrated here chronologically.

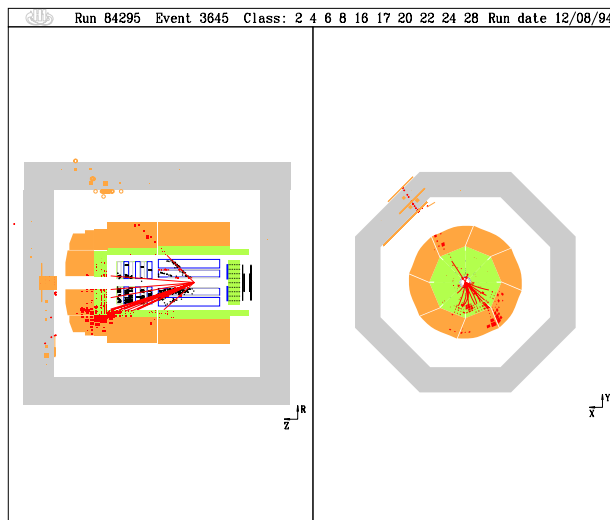


Figure A.1: Run 84295 Event 3645. A  $W \rightarrow \mu\nu$  candidate. (12.08.94  $\sim$ 1000)

Run 90264 Event 313 Class: 2 8 9 12 14 17 20 22 Run date 29/10/94

$e^+ p \rightarrow e^- X$

$E - P_z = 10 \text{ GeV}$   $P_{Tmiss} = 30 \text{ GeV}$

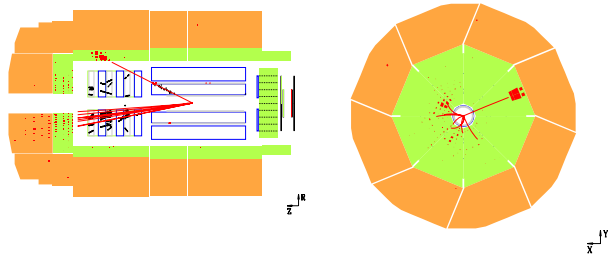


Figure A.2: Run 90264 Event 313. A  $W \rightarrow e\nu$  candidate. (29.10.94 ~0630)

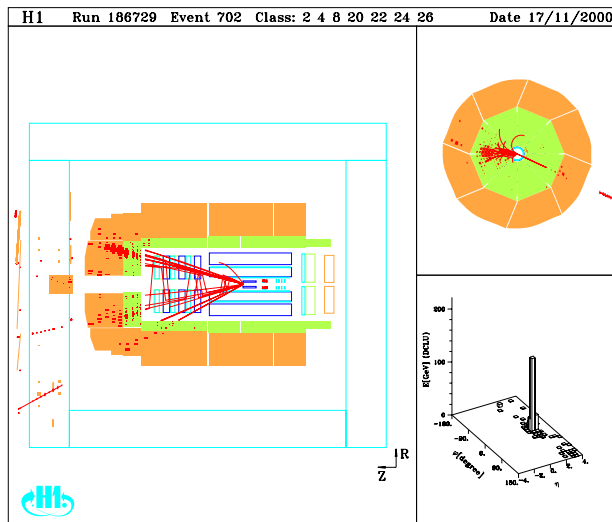


Figure A.3: Run 186729 Event 702. A  $W \rightarrow \mu\nu$  candidate. (04.05.97 ~0330)

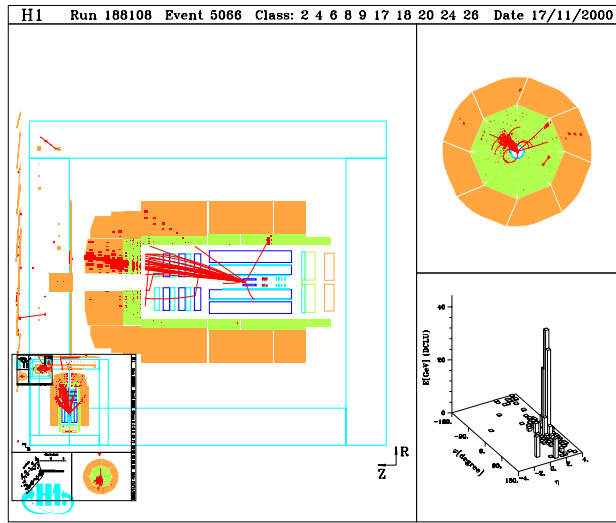


Figure A.4: Run 188108 Event 5066. A  $W \rightarrow \mu\nu$  candidate. (15.05.97 ~2030)

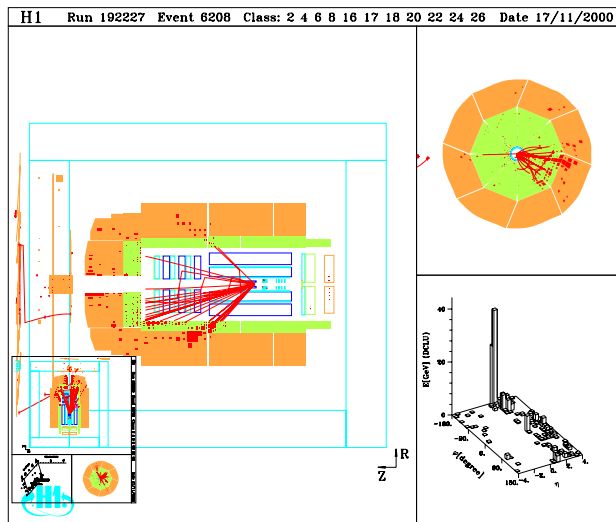


Figure A.5: Run 192227 Event 6208. A  $W \rightarrow \mu\nu$  candidate. (17.06.97 ~0345)

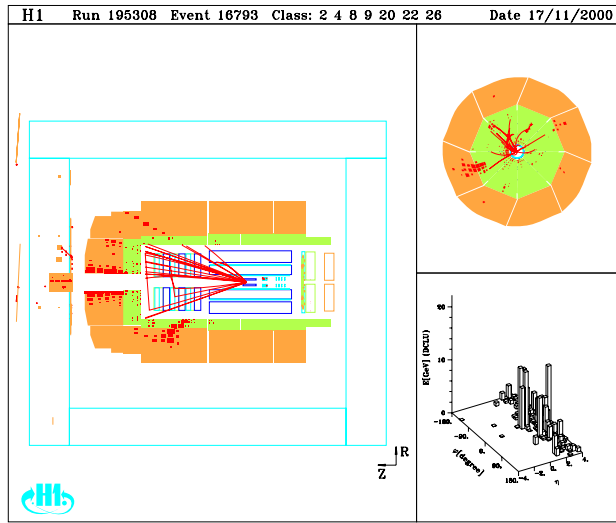


Figure A.6: Run 195308 Event 16793. A  $W \rightarrow \mu\nu$  candidate. (18.07.97 ~1100)

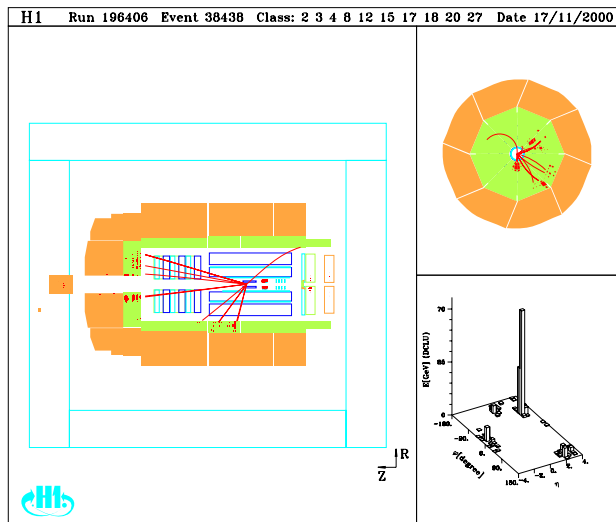


Figure A.7: Run 196406 Event 38438. A  $W \rightarrow \mu\nu$  candidate. (02.08.97 ~1530)

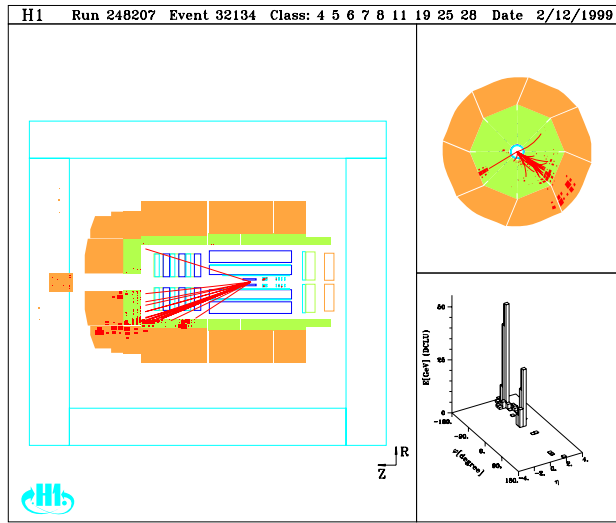


Figure A.8: Run 248207 Event 32134. A  $W \rightarrow e\nu$  candidate. (27.07.99 ~0630)

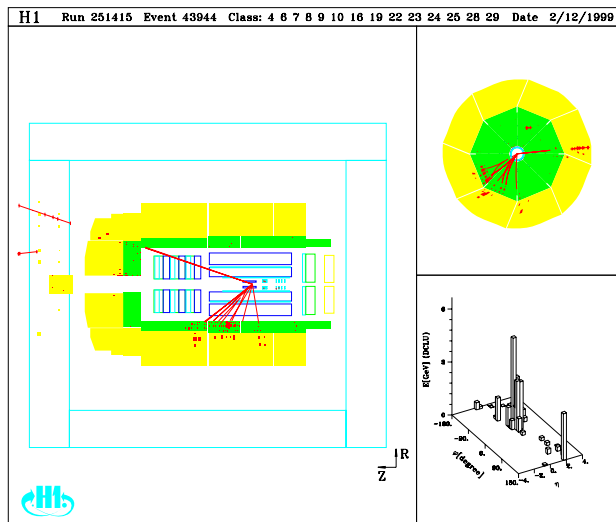


Figure A.9: Run 251415 Event 43944. A  $W \rightarrow \mu\nu$  candidate. (22.08.99 ~1600)

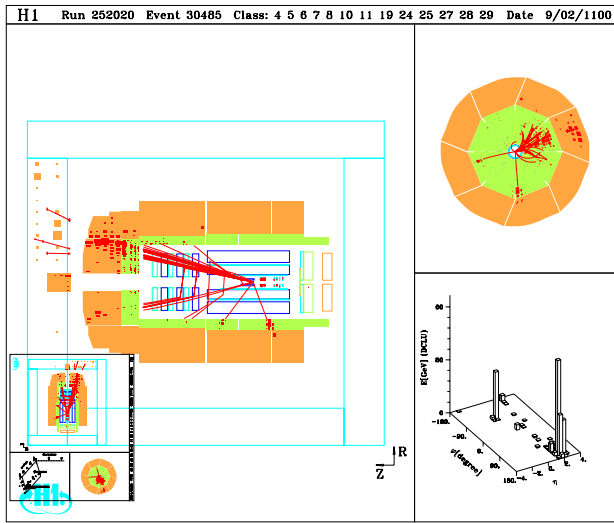


Figure A.10: Run 252020 Event 30485. A  $W \rightarrow e\nu$  candidate. (27.08.99  $\sim$ 0700)

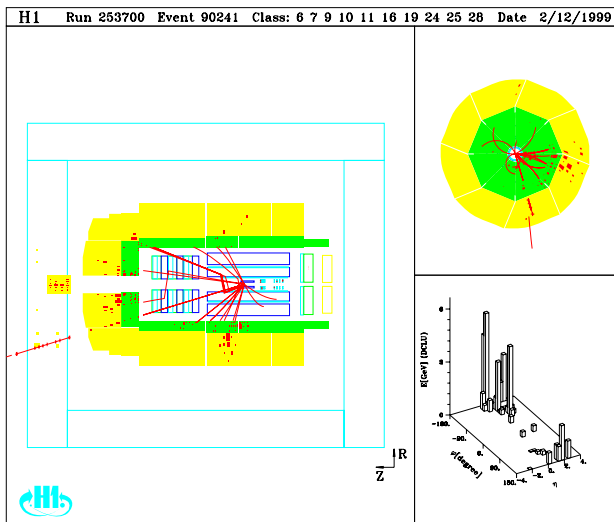


Figure A.11: Run 253700 Event 90241. A  $W \rightarrow \mu\nu$  candidate. (15.09.99  $\sim$ 0400)



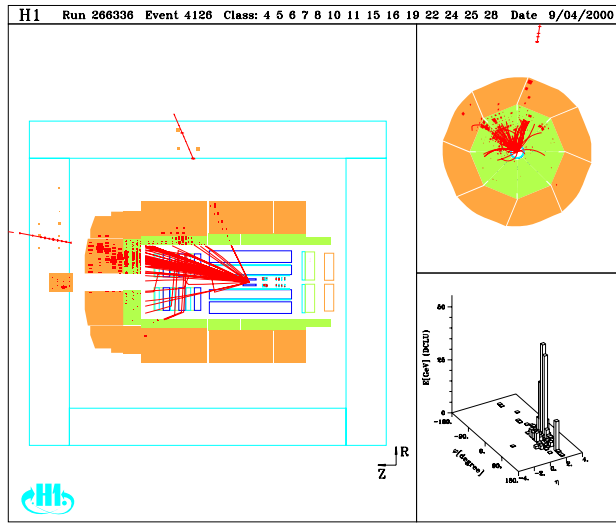


Figure A.12: Run 266336 Event 4126. A  $W \rightarrow \mu\nu$  candidate. (04.03.00 ~1500)

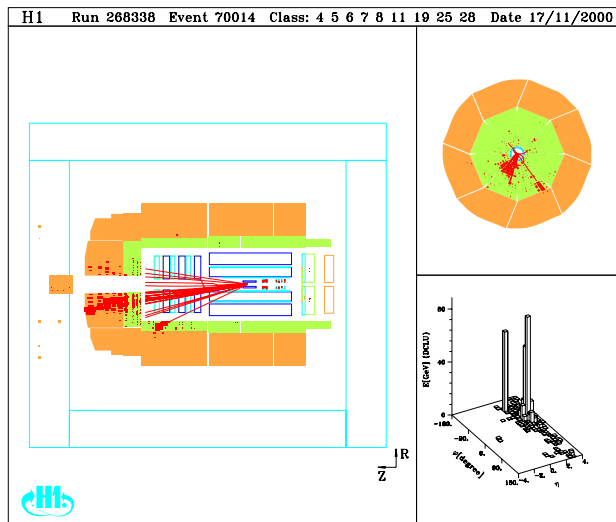


Figure A.13: Run 268338 Event 70014. A  $W \rightarrow e\nu$  candidate. (01.04.00 ~1000)

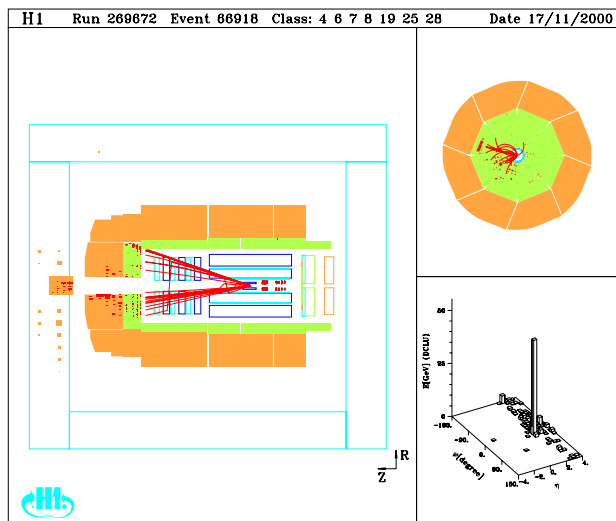


Figure A.14: Run 269672 Event 66918. A  $W \rightarrow e\nu$  candidate. (12.04.00 ~2230)

# Appendix B

## Comparison with ZEUS

ZEUS have also performed a search for events with missing transverse momentum and an isolated high  $P_T$  lepton [89]. No excess of events above the Standard Model expectation at high  $P_T^X$  was observed. Recently ZEUS have performed a search for  $P_T^X > 25$  GeV with additional cuts to enhance the  $W$  component of the selected events [90]. The ZEUS selection is very similar to that of H1 apart from the angular range, which is smaller in the ZEUS analysis. To facilitate comparison between the two experiments, H1 have repeated their analysis [83], with the additional requirement that  $0.3 < \theta_{lepton} < 2.0$  radians, which is approximately the ZEUS angular range. The results are shown in table B.1. All events for  $P_T^X > 25$  GeV that are found with the analysis presented in this thesis are also found with the restricted angular range. The Standard Model expectation is reduced by 20-25%.

Electron	H1 Data	SM expectation	$W$	Other SM processes
$P_T^X > 25$ GeV	3	$0.84 \pm 0.22$	$0.67 \pm 0.20$	$0.16 \pm 0.09$
$P_T^X > 40$ GeV	2	$0.27 \pm 0.08$	$0.26 \pm 0.08$	$0.01 \pm 0.01$
Muon	H1 Data	SM expectation	$W$	Other SM processes
$P_T^X > 25$ GeV	6	$0.94 \pm 0.26$	$0.78 \pm 0.23$	$0.16 \pm 0.10$
$P_T^X > 40$ GeV	4	$0.35 \pm 0.10$	$0.33 \pm 0.10$	$0.02 \pm 0.01$

Table B.1: Observed and predicted event rates in the electron and muon decay channel for all  $e^+p$  data, with the angular range restricted to  $0.3 < \theta_{lepton} < 2.0$  radians. Taken from [83]

# Appendix C

## A Note about Collaboration

High energy particle physics is a highly collaborative science. The author has been a member of the H1 collaboration since July 1998. The analysis presented in this thesis is his own work, although that work has been carried out as a member of the H1 High  $P_T/Q^2$  working group, and the DESY based H1-UK group. Like all contemporary data analyses, this thesis has relied greatly on the support of working group colleagues and the general H1 infrastructure. The author was the principal author of the publication of this analysis in [39] and [83].

# Acknowledgements

Three years, tens of thousands of miles and 167 pages later and my doctoral odyssey draws to a close. High energy physics, perhaps more than any other hard science, involves a great deal of personal interaction. It has been my great pleasure and good fortune to work, study and play with some fantastic people during the course of my Ph.D. studentship.

Chronologically... Through their own enormous enthusiasm and intellect Fred Loebinger and Robin Marshall inspired me to start, and stick with, a particle physics Ph.D.

Very little of what is presented here would have been possible without the guidance, insight and friendship of Andrew Mehta, whether hammering out conference results in adjoining offices at 2am, arguing pedantic nonsense in St. Pauli bars at 4am or soaking up the French Riviera sunshine (around tea-time).

Beate Heinemann, John Kennedy, Eram Rizvi, Dave South, Paul Thompson and Ben Waugh deserve thanks for also bridging work and friendship so well. Joachim Meyer gets special mention for being everything a grey-haired, fluent English speaking, German professor should be. John Dainton, Eckhard Elsen, Joerg Gayler and Peter Schleper have been wonderfully informal and friendly, despite their seniority.

Bleicherstraße was a great place to live, enhanced by the friendship of Paul Bate, Anna Burrage, Julian Phillips and Angela Wyatt. Hamburg wouldn't have been the same without Asia or William Thompson.

Throughout, people back home have been fantastically supportive, particularly during the difficult times. Award winners in this category are Cat and Chris, Nick, Rowan and Dickon. Special mention also to Mr and Mrs Matthew, and the other Dinosaurs. In a category all of her own is Ms Lawrie, because what wasn't hell was heaven.

Bill, Caroline, Charlie and Mark have made the process of writing up so much more bearable, through their good humour, cooking, and inexhaustible alcohol reserves.

Finally, thankyou to my parents for their love, support and patience.

